JSCSEN 90(3) 271-392(2025)

ISSN 1820-7421(Online)

Journal of the Serbian Chemical Society

Electronic version

VOLUME 90

No 3

BELGRADE 2025

Available on line at

www.shd.org.rs/JSCS/

The full search of JSCS is available through

DOAJ DIRECTORY OF OPEN ACCESS JOURNALS

www.doaj.org

The **Journal of the Serbian Chemical Society** (formerly Glasnik Hemijskog društva Beograd), one volume (12 issues) per year, publishes articles from the fields of chemistry. The **Journal** is financially supported by the **Ministry of Education, Science and Technological Development of the Republic of Serbia.**
Articles published in the **Journal** are indexed in **Clarivate Analytics products: Science Citation Index-Expanded™** – accessed *via* **Web of Science®** and **Journal Citation Reports®**.
Impact Factor announced on 28 June, 2023: **1.000; 5-year Impact Factor**: **1.100**.
Articles appearing in the **Journal** are also abstracted by: **Scopus, Chemical Abstracts Plus (CAplus℠), Directory of Open Access Journals, Referativnii Zhurnal (VINITI), RSC Analytical Abstracts, EuroPub, Pro Quest** and **Asian Digital Library.**

Publisher:	**Serbian Chemical Society**, Karnegijeva 4/III, P. O. Box 36, 1120 Belgrade 35, Serbia tel./fax: +381–11–3370–467, E-mails: **Society** – shd@shd.org.rs; **Journal** – jscs@shd.org.rs Home Pages: **Society** – http://www.shd.org.rs/, **Journal** – http://www.shd.org.rs/JSCS/
Internet Service:	Contents, Abstracts and full papers (from Vol 64, No. 1, 1999) are available in the electronic form at the Web Site of the **Journal** (http://www.shd.org.rs/JSCS/).
Former Editors:	**Nikola A. Pušin** (1930–1947), **Aleksandar M. Leko** (1948–1954), **Panta S. Tutundžić** (1955**–**1961), **Miloš K. Mladenović** (1962–1964), **Đorđe M. Dimitrijević** (1965–1969), **Aleksandar R. Despić** (1969–1975), **Slobodan V. Ribnikar** (1975–1985), **Dragutin M. Dražić** (1986–2006).
Editor-in-Chief:	BRANISLAV Ž. **NIKOLIĆ**, Serbian Chemical Society (E-mail: jscs-ed@shd.org.rs)
Deputy Editor:	DUŠAN **SLADIĆ**, Faculty of Chemistry, University of Belgrade
Sub editors:	
Organic Chemistry	DEJAN **OPSENICA**, Institute of Chemistry, Technology and Metallurgy, University of Belgrade JÁNOS **CSANÁDI**, Faculty of Science, University of Novi Sad
Biochemistry and Biotechnology	OLGICA **NEDIĆ**, INEP – Institute for the Application of Nuclear Energy, University of Belgrade
Inorganic Chemistry	BILJANA **GLIŠIĆ**, Faculty of Science, University of Kragujevac
Theoretical Chemistry	MATIJA **ZLATAR**, Institute of Chemistry, Technology and Metallurgy, University of Belgrade MILOŠ **MILIČIĆ**, Faculty of Chemistry, University of Belgrade
Physical Chemistry	LJILJANA **DAMJANOVIĆ-VASILIĆ**, Faculty of Physical Chemistry, University of Belgrade
Electrochemistry	SNEŽANA **GOJKOVIĆ**, Faculty of Technology and Metallurgy, University of Belgrade
Analytical Chemistry	RADA **BAOŠIĆ**, Faculty of Chemistry, University of Belgrade
Polymers	BRANKO **DUNJIĆ**, Faculty of Technology and Metallurgy, University of Belgrade
Thermodynamics	MIRJANA **KIJEVČANIN**, Faculty of Technology and Metallurgy, University of Belgrade
Chemical Engineering	TATJANA **KALUĐEROVIĆ RADOIČIĆ**, Faculty of Technology and Metallurgy, University of Belgrade
Materials	RADA **PETROVIĆ**, Faculty of Technology and Metallurgy, University of Belgrade
Metallic Materials and Metallurgy	ANA **KOSTOV**, Mining and Metallurgy Institute Bor, University of Belgrade
Environmental and Geochemistry	VESNA **ANTIĆ**, Faculty of Agriculture, University of Belgrade
History of and Education in Chemistry	DRAGICA **TRIVIĆ**, Faculty of Chemistry, University of Belgrade
English Language Editors:	LYNNE **KATSIKAS**, Serbian Chemical Society VLATKA **VAJS**, Serbian Chemical Society JASMINA **NIKOLIĆ**, Faculty of Technology and Metallurgy, University of Belgrade
Technical Editors:	VLADIMIR **PANIĆ**, Institute of Chemistry, Technology and Metallurgy, University of Belgrade, MARIO **ZLATOVIĆ**, Faculty of Chemistry, University of Belgrade
Journal Manager & Web Master:	MARIO **ZLATOVIĆ**, Faculty of Chemistry, University of Belgrade
Office:	VERA **ĆUŠIĆ**, Serbian Chemical Society

Editorial Board

From abroad: **R. Adžić**, Brookhaven National Laboratory (USA); **A. Casini**, University of Groningen (The Netherlands); **G. Cobb**, Baylor University (USA); **D. Douglas**, University of British Columbia (Canada); **G. Inzelt**, Etvos Lorand University (Hungary); **J. Kenny**, University of Perugia (Italy); **Ya. I. Korenman**, Voronezh Academy of Technology (Russian Federation); **M. D. Lechner**, University of Osnabrueck (Germany); **S. Macura**, Mayo Clinic (USA); **M. Spiteller**, INFU, Technical University Dortmund (Germany); **M. Stratakis**, University of Crete (Grecce); **M. Swart**, University de Girona (Cataluna, Spain); **G. Vunjak-Novaković**, Columbia University (USA); **P. Worsfold**, University of Plymouth (UK); **J. Zagal**, Universidad de Santiago de Chile (Chile).

From Serbia: **B. Abramović**, **V. Antić**, **R. Baošić**, **V. Beškoski**, **J. Csanadi**, **Lj. Damjanović-Vasilić**, **A. Dekanski**, **V. Dondur**, **B. Dunjić**, **M. Đuran, B. Glišić, S. Gojković**, **I. Gutman**, **B. Jovančićević**, **I. Juranić**, **T. Kaluđerović Radoičić**, **L. Katsikas**, **M. Kijevčanin**, **A. Kostov**, **V. Leovac**, **S. Milonjić**, **V.B. Mišković-Stanković**, **O. Nedić**, **B. Nikolić**, **J. Nikolić**, **D. Opsenica**, **V. Panić**, **M. Petkovska**, **R. Petrović**, **I. Popović**, **B. Radak**, **S. Ražić**, **D. Sladić**, **S. Sovilj**, **S. Šerbanović**, **B. Šolaja**, **Ž. Tešić**, **D. Trivić**, **V. Vajs, M. Zlatović**.

Subscription: The annual subscription rate is **150.00 €** including postage (surface mail) and handling. For Society members from abroad rate is **50.00 €**. For the proforma invoice with the instruction for bank payment contact the Society Office (E-mail: shd@shd.org.rs) or see JSCS Web Site: http://www.shd.org.rs/JSCS/, option Subscription.
Godišnja pretplata: Za članove SHD: **2.500,00 RSD**, za penzionere i studente: **1000,00 RSD**, a za ostale: **3.500,00 RSD**:za organizacije i ustanove: **16.000,00 RSD**. Uplate se vrše na tekući račun Društva: **205-13815-62**, poziv na broj **320**, sa naznakom "pretplata za JSCS".

Nota: Radovi čiji su svi autori članovi SHD prioritetno se publikuju.
Odlukom Odbora za hemiju Republičkog fonda za nauku Srbije, br. 66788/1 od 22.11.1990. godine, koja je kasnije potvrđena odlukom Saveta Fonda, časopis je uvršten u kategoriju međunarodnih časopisa (**M-23**). Takođe, aktom Ministarstva za nauku i tehnologiju Republike Srbije, 413-00-247/2000-01 od 15.06.2000. godine, ovaj časopis je proglašen za publikaciju od posebnog interesa za nauku. **Impact Factor** časopisa objavljen 28. juna 2023. godine je **1,000**, a petogodišnji **Impact Factor 1,100**.

Journal of the Serbian Chemical Society
JSCS-info@shd.org.rs • www.shd.org.rs/JSCS

J. Serb. Chem. Soc. Vol. 90, No. 3(2025)

CONTENTS*

Published by the Serbian Chemical Society
Karnegijeva 4/III, P.O. Box 36, 11120 Belgrade, Serbia
Printed by the Faculty of Technology and Metallurgy
Karnegijeva 4, P.O. Box 35-03, 11120 Belgrade, Serbia

* For colored figures in this issue please see electronic version at the Journal Home Page: http://www.shd.org.rs/JSCS/

Journal of the Serbian Chemical Society
JSCS@tmf.bg.ac.rs • www.shd.org.rs/JSCS
J. Serb. Chem. Soc. *90* (3) 271–276 (2025)
JSCS–5385
Short communication
Published 24 March, 2025

SHORT COMMUNICATION

Phytochemical investigation from wood residues of *Dalbergia spruceana* Benth

HELENA GARCIA RAMOS[1], JENNIFER ARAÚJO DE OLIVEIRA LIMA[1], HENRIQUE CATIVO DOS SANTOS[1], CLAUDETE CATANHEDE DO NASCIMENTO[2], LUIZ HENRIQUE KENG QUEIROZ-JUNIOR[3] and MARIA DA PAZ LIMA[2]*

[1]Instituto de Ciências Exatas, Universidade Federal do Amazonas, Manaus, CEP 69080-900, Amazonas, Brazil, [2]Coordenação de Tecnologia e Inovação, Instituto Nacional de Pesquisas da Amazônia, Manaus, CEP 69067-375, Amazonas, Brazil and [3]Instituto de Química, Universidade Federal de Goiás, Goiânia, CEP 74001970, Goiás, Brazil

(Received 6 June, revised 21 July, accepted 21 September 2024)

Abstract: *Dalbergia spruceana* Benth (Fabaceae: Papilionoideae), known in the Brazilian Amazon as ¨jacarandá-do-pará" recognized for the natural resistance of its wood has little scientific information about its secondary metabolism. In this paper, we report a phytochemical study of the wood residues of *D. spruceana* using classical chromatographic techniques. Thus, the chromatographic fractionation of methanolic extract resulted in the isolation of phenylpropanoid, isoflavonoids of different types (pterocarpan, isoflavonol, isoflavan, isoflavone) in addition to a neoflavonoid. A new isoflavonoid with an oxygenation pattern not previously reported was elucidated as 8,4,2'-trihydroxy-7,4'-dimethoxyisoflavonol. The structures of all the isolated compounds were determined by using 1D- and 2D-NMR techniques, mass spectrometry ESI-MS and by comparison with literature data. Most of the compounds that were identified are isoflavonoids, which are types of flavonoids that are especially recognized for their contribution to the natural resistance of the wood.

Keywords: Fabaceae; flavonoid; pterocarpan; neoflavonoid; natural resistance.

INTRODUCTION

Dalbergia spruceana Benth (*Miscolobium spruceanum* Benth, Fabaceae: Papilionoideae) is a species that is native to northern South America, and is known in the Brazilian Amazon as "jacarandá-do-pará". It has registered occurrence in the states of Amazonas, Amapá, Rondônia and Pará[1,2] and has great economic potential because its wood can be used for special purposes such as the manufacture of luxury furniture, decorative objects and musical instruments. It

* Corresponding author. E-mail: mdapaz@inpa.gov.br
https://doi.org/10.2298/JSC240606091R

has medium to fast growth and easy propagation and is therefore recommended for reforestation and forest restoration programs.[3]

There is little scientific information about the secondary metabolism of *D. spruceana.* The chemical composition of the genus *Dalbergia* is represented mainly by phenolic compounds, which are found in different vegetative parts.[4] The planting of this species is very promising because it has propagation potential, economic potential because the wood has natural resistance, and it is also sought after for making string instruments, among other purposes. Woods with natural strength often have interesting secondary metabolites that have promising bioactive compounds.[5–10] In this paper, we evaluated the secundary metabolites extracted from the heartwood of *D. spruceana* using classical chromatographic techniques.

EXPERIMENTAL

General experimental procedures

NMR spectra were recorded on a Bruker Fourier 300 UltraShield (300 MHz for ^{1}H- and 75 MHz for ^{13}C-NMR) and Bruker Avance III 400 (400 MHz for ^{1}H- and 100 MHz for ^{13}C--NMR) spectrometers, at a temperature of 25 °C. The spectra were referenced to the residual solvent signal. HRESIMS data were obtained on an MicroTOF–Q–II, Bruker Daltonics, the ESI was operated in the positive and negative mode, and nitrogen was used as the drying gas (4.0 L/min) and nebulizing gas at 0.4–0.6 bar. Mass-to-charge ratio was scanned in the *m*/*z* 50–980 range. For column chromatography (CC), silica gel (particle size 70–230 and 230–300 mesh, Sigma–Aldrich), hexane, ethyl acetate, acetone and methylene chloride were used. Analytical and preparative TLC was carried out on silica gel 60 GF254 20 cm×20 cm plates, with a layer thickness of 0.25 mm (Merck).

Acquisition and identification of wood residues

D. spruceana from wood residues was supplied to the Wood Technology Laboratory of the National Institute for Amazonian Research (INPA) by a luthier. The largest residues had been previously evaluated for their technological properties and the smaller residues resulting from these procedures became available for phytochemical studies. The identification of the wood samples was done via macroscopic comparisons with standard samples from the xylotheque at INPA (INPA-Xil N0 4329).

Extraction and isolation

The residues were chopped and ground (1.117 g) and submitted to maceration at room temperature with *n*-hexane and then methanol (seven days in each solvent), which provided yields of 0.05 and 3.67 %, respectively. The methanol extract (19 g) was purified on silica gel CC using gradient elution with Hexane/EtOAc (98:2 to 60:40) to obtain 90 fractions. The fraction 46 (20 mg) was purfied with preparative TLC using mixture of CH_2Cl_2/acetone (98:2) for isolation of compound **1** (10 mg). The additional purification of the fraction 61 (70 mg) with silica gel column chromatography (230–400 mesh; 46 cm×2.6 cm) and CH_2Cl_2 as eluent lead to further purification of subfractions 15 and 17 and final isolation of compounds **3** (3.5 mg) and **4** (5.5 mg). The fractions 71 (52.0 mg) and 73 (80.0 mg) were subjected to additional silica gel CC with mixture of CH_2Cl_2/acetone (98:2) as eluent for obtaining compounds **5**

(10.0 mg) and **6** (3.5 mg). Fractions 50 (970 mg) and 83 (18.1 mg) represent the solid compounds **2** (805 mg) and **7** (5.8 mg), respectively.

RESULTS AND DISCUSSION

From the methanol extracts of *Dalbergia spruceana* Benth wood residues five known compounds as phenylpropanoid elemycin (**1**),[11] flavonoids maackiain (**2**),[12] 8-hydroxy-7-methoxy-3',4' methylenedioxypterocarpane (**3**),[13,14] dalbergine (**5**),[15] 3',4'-dihydroxy-7,8,2'-trimethoxy-isoflavan (**6**), pseudobaptigenin (**7**)[16] and one (**4**) previously undescribed isoflavonoid were isolated. The isolated compounds were identified using 1D (^{1}H and ^{13}C) and 2D NMR (HSQC and HMBC), HRESIMS spectra and by comparison with the literature data (Fig. 1). HMBC correlations provide identification of flavonoids and reveal the oxygenation patterns, Fig. 1 (for additional data see Supplementary material to this paper).

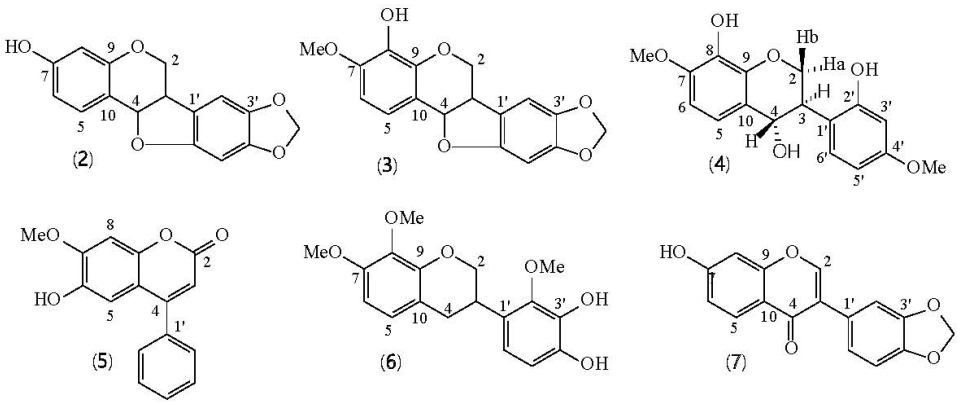

Fig. 1. Structures of the flavonoids from the wood residues of *Dalbergia spruceana*.

The molecular formula of compound **4**, $C_{17}H_{18}O_7$, was determined based on the HRESIMS ion $[M+Na]^+$ at *m/z* 341.0994. The ^{1}H-NMR spectrum revealed an aromatic system of ABX-type spins observed by the set of hydrogen signals in the δ region 7.26–6.38 ppm, in addition to the *ortho*-coupled signals at δ 6.97 and 6.69 ppm (Table I). The signals of oxymethylene at δ 4.34 and 3.63 ppm, methine at δ 3.65 ppm and oxymethine at δ 5.58 ppm were indicative of 4-hydroxyisoflavonol. The ^{1}H- and ^{13}C-NMR data with significant NOESY and HMBC correlations are presented in Table I. The HMBC correlations H-5/C-4, C-7 and C-9 and H-6'/C-3, C-1' and C-2' revealed oxygenation patterns for A and B rings. The NOESY correlations H-2a/H-3 and H2b/H-4 indicated *trans* orientation of H-3 and H-4. Based on 1D and 2D NMR data, the structure of new isoflavonoid was labelled as 8,4,2' trihydroxy-7,4'-dimethoxyisoflavonol.

In the Fabaceae family, the isoflavonoids are restricted almost entirely to Papilionoideae[17] and are especially recognized for their contribution to the natural resistance of the wood containing them, such as is the case of *D. spruceana*.

TABLE I. ^{1}H- and ^{13}C-NMR spectroscopic data (δ / ppm) for compound **4** in $(CD_3)_2CO$; ^{1}H-NMR (300 MHz, J / Hz); ^{13}C-NMR (75 MHz)

H/C	δ H (J in Hz)	NOESY	δ C	HMBC
2	4.33 *m* (2a) 3.63 *m* (2b)	H-3, H4	66.5	C-3, C-4, C-9, C-1’
3	3.65 *m*	H-2a	39.6	C-2, C-4, C-1’
4	5.58 *d* (6.7)	H-2b	78.6	C-2, C-3, C-10, C-1’
5	6.97 *d* (8.5)		120.5	C-4, C-7, C-9
6	6.74 *d* (8.5)	H_3-7	105.8	C-5, C-7, C-8, C-9, C-10
7			148.1	
8			135.1	
9			144.2	
10			114.5	
1’			119.4	
2’			160.8	
3’	6.38 *d* (2.2)		96.2	C-1’, C-4’, C-5’
4’			161.2	
5’	6.47 *dd* (8.1 and 2.2)	H_3-4’	106.0	C-1, C-3’
6’	7.26 *d* (8.1)		125.0	C-3, C-1’, C-2’
OMe-7	3.84 *s*		55.7	C-7
OMe-4’	3.74 *s*		54.8	C-4’

CONCLUSION

A phytochemical analysis of woody residues of *Dalbergia spruceana* was conducted and resulted in the identification of mainly isoflavonoids of different types (pterocarpan, isoflavonol, isoflavan, isoflavone) in addition to a neoflavonoid. Among these, the compound **4** was previously undescribed. The woody residues of this species of Fabaceae gave us an opportunity to gain further knowledge regarding its secondary metabolism and therefore increase the value of solid residues from *D. spruceana* discarded by the wood processing sector.

SUPPLEMENTARY MATERIAL

Additional data and information are available electronically at the pages of journal website: https://www.shd-pub.org.rs/index.php/JSCS/article/view/12948, or from the corresponding author on request.

Acknowledgements. The authors are grateful for the support from the Fundação de Amparo à Pesquisa Estado do Amazonas, Grant No 01.02.016301.03412/2021-78 and for the scholarship granted to Helena Garcia Ramos (Call 2021-2022 - POSGRAD) and Maria da Paz Lima (Call No. 013/2022 – Produtividade - CT&I).

ИЗВОД

ФИТОХЕМИЈСКО ИСПИТИВАЊЕ ДРВНИХ ОСТАТАКА *Dalbergia spruceana* BENTH

HELENA GARCIA RAMOS[1], JENNIFER ARAÚJO DE OLIVEIRA LIMA[1], HENRIQUE CATIVO DOS SANTOS[1], CLAUDETE CATANHEDE DO NASCIMENTO[2], LUIZ HENRIQUE KENG QUEIROZ-JUNIOR[3] и MARIA DA PAZ LIMA[2]

[1]Instituto de Ciências Exatas, Universidade Federal do Amazonas, Manaus, CEP 69080-900, Amazonas, Brazil, [2]Coordenação de Tecnologia e Inovação, Instituto Nacional de Pesquisas da Amazônia, Manaus, CEP 69067-375, Amazonas, Brazil и [3]Instituto de Química, Universidade Federal de Goiás, Goiânia, CEP 74001970, Goiás, Brazil

Биљка *Dalbergia spruceana* Benth (Fabaceae: Papilionoideae) позната у бразилском Амазону као „jacarandá-do-pará”, иако је препозната по природној отпорности има мало научних информација о њеном секундарном метаболизму. У овом раду описано је фитохемијско испитивање дрвних остатака *D. spruceana* применом класичних хроматографских техника. Хроматографским фракционисањем метанолног екстракта изоловани су фенилпропаноиди, изофлавоноиди различитих типова (птерокарпан, изофлавонол, изофлаван, изофлавон), као и неофлавоноиди. Нови изофлавоноид, са јединственом структуром која је настала оксидацијом која раније није пријављена, дефинисан је као 8,4,2'-трихидрокси-7,4'-диметоксиизофлавонол. Структуре свих изолованих једињења одређене су коришћењем 1D и 2D NMR техника, масене спектрометрије ESI--MS и поређењем са литературним подацима. Већина идентификованих једињења су изофлавоноиди, типови флавоноида за које је веома познато да доприносе природној отпорности дрвета.

(Примљено 6. јуна, ревидирано 21. јула, прихваћено 21. септембра 2024)

REFERENCES

1. *Tropicos – Missouri Botanical Garden 2024*. Available from: https://www.tropicos.org/name/Search?name=Dalbergia%20spruceana (accessed on 06/05/2024)
2. L. A. G. Souza, *Guia da biodiversidade de Fabaceae do Alto Rio Negro*, INPA, Ed., Manaus-AM, 2012, p. 118 (ISBN 583.322)
3. J. R. V. Gama, J. C. Pinheiro, *Floresta* **40** (2010) 585 (ISSN 0015-3826).
4. A. A. Carvalho, L. R. Santos, J. S. Freitas, M. H. Chaves, *Quim. Nova* **9** (2020) 1294 (http://dx.doi.org/10.21577/0100-4042.20170588)
5. N-l. Zan, Z-H. Lu, X-Y. R-Y. Wang, N-Y. Liang, H-X. Huo, Y-F. Zhao, Y-L. Song, P-F. Tu, J. Zheng, J. Li, *Nat. Prod. Res*. **37** (2023) 928 (https://doi.org/10.1080/14786419.2022.2098494)
6. F. Shao, L. Panahipour, M. B, Sordi, F. Tang, R. Liu, R. Gruber, *Molecules* **27** (2022) 1321 (https://doi.org/10.3390/molecules27041321)
7. B. Lee, J.W. Lee, Q. Jin, D. S. Jang, S-J. Lee, D. Lee, J. T. Hong, Y. Kim, M. K. Lee, B. Y. Hwang, *Bioorg. Med. Chem*. Lett. **23** (2013) 4263 (https://doi.org/10.1016/j.bmcl.2013.04.032)
8. F. Shao, L. Panahipour, A. Omerbasic, F. Tang, R. Gruber, *Clin. Oral Invest.* **26** (2022) 5419 (https://doi.org/10.1007/s00784-022-04509-7)
9. S. Cheenpracha, T. Ritthiwigrom, C. Karalai, S. Laphookhieo, *Phytochem. Lett*. **5** (2012) 708 (https://doi.org/10.1016/j.phytol.2012.07.007)
10. H. Wang, W. Mei, Y. Zeng, W. Zuo, Z. Guo, L. Chen, H. Zhong, H. Dai, *Phytochem. Lett*. **9** (2014) 168 (https://doi.org/10.1016/j.phytol.2014.06.008)

11. F. R. Garcez, W. S. Garcez, L. Hamerski, C. H. Miguita, *Quim. Nova* **32** (2009) 407 (https://doi.org/10.1590/S0100-40422009000200026)
12. C. K. Swapan, L. Huang, F. Fekadu, D. M. Brown, M. C. Wani, M. E. Wall, J. C. Tucker, C. W. W. Beecher, A. D. Kinghorn, *J. Nat. Prod*. **58** (1995) 1966 (https://doi.org/10.1021/np50126a030)
13. H. J. Jung, S. S. Kang, S. K. Hyun, J. S. Choi, *Arch. Pharm. Res*. **28** (2005) 534 (https://doi.org/10.1007/BF02977754)
14. S. Cheenpracha, C. Karalai, C. Ponglimanont, A. Kanjana-Opas, *J. Nat. Prod*. **72** (2009) 1395 (https://doi.org/10.1021/np900077h)
15. N. T. Nhan, P. H. Nguyen, D. T. B. Hanh, D. T. T. My, N. P. D. Nguyen, T. B. Phong, D. C. To, *Eur. J. Inflamm.* **20** (2022) 172 (https://doi.org/10.1177/1721727X221132273)
16. N. Gampe, A. Darcsi, L. Kursinszki, S. Béni, *J. Chromatogr., B* **1091** (2018) 21 (https://doi.org/10.1016/j.jchromb.2018.05.023)
17. N. C. Veitch, *Nat. Prod. Rep*. **30** (2013) 988 (https://doi.org/10.1039/b511238a).

Journal of the Serbian Chemical Society
JSCS@tmf.bg.ac.rs • www.shd.org.rs/JSCS
J. Serb. Chem. Soc. 90 (3) S85–S90 (2025) *Supplementary material*

SUPPLEMENTARY MATERIAL TO

Phytochemical investigation from wood residues of *Dalbergia spruceana* Benth

HELENA GARCIA RAMOS[1], JENNIFER ARAÚJO DE OLIVEIRA LIMA[1], HENRIQUE CATIVO DOS SANTOS[1], CLAUDETE CATANHEDE DO NASCIMENTO[2], LUIZ HENRIQUE KENG QUEIROZ-JUNIOR[3] and MARIA DA PAZ LIMA[2]*

[1]*Instituto de Ciências Exatas, Universidade Federal do Amazonas, Manaus, CEP 69080-900, Amazonas, Brazil,* [2]*Coordenação de Tecnologia e Inovação, Instituto Nacional de Pesquisas da Amazônia, Manaus, CEP 69067-375, Amazonas, Brazil and* [3]*Instituto de Química, Universidade Federal de Goiás, Goiânia, CEP 74001970, Goiás, Brazil*

J. Serb. Chem. Soc. 90 (3) (2025) 271–276

EXTRACTION AND ISOLATION OF COMPOUNDS

The wood residues of *Dalbergia spruceana* were submitted to maceration for 7 days with hexane and methanol, which provided yields of 0.05 and 3.67%, respectively. The fractionation of the methanol extract (19 g) was carried out on a silica gel column (70-230 mesh; h x ø = 30 x 5 cm), eluted with hexane-EtOAc (2-40%), and generated ninety fractions. Fr. 27 (47 mg) showed a predominance of β-sitosterol and stigmasterol. Fr. 46 (20 mg) was obtained by preparative thin layer chromatography (PTLC) eluted with CH_2Cl_2-acetone (98:2) and resulted in the purification of compound **1** (10 mg). Fr. 50 gave the solid compound **2** (900 mg). Fr. 61 (70.0 mg) was fractionated over a silica gel column (230-400 mesh; h x ø = 46 x 2.6 cm) and eluted with CH_2Cl_2. Subfractions 15 and 17 were submitted to new fractioning. Subfraction 15 (23.0 mg) was fractionated over silica gel column (230-400 mesh; h x ø = 38.5 x 1.2 cm) and eluted with CH_2Cl_2-MeOH (98:2) to obtain compound **3** (3.5 mg). Subfr. 17 (35 mg) resulted the isolation of compound **4** (5.5 mg), after purification in PTLC and elution with of CH_2Cl_2-MeOH (98:2). The fractionation of 71 (52.0 mg) over a silica gel column (230-400 mesh; h x ø = 37.0 x 2.6 cm) and elution with CH_2Cl_2-acetone (98:2) provided compound **5** (10.0 mg). The fraction 73 (80 mg) was fractionated over a silica gel column (230-400 mesh; h x ø = 8.0 x 0.7 cm), eluted with CH_2Cl_2-acetone (98:2) and resulted in the purification of **6** (3.5 mg). The fraction 83 gave the solid compound **7** (5.8 mg).

CHARACTERIZATION DATA FOR COMPOUNDS **1-3** AND **5-7**

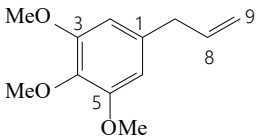

* Corresponding author. E-mail: mdapaz@inpa.gov.br

*Elemycin (**1**).* ^{1}H NMR (300 MHz, $CDCl_3$, J/Hz): 6.43 (s, H-2 and H-6), 5.97 (m, H-8), 5.11 (m, H-9), 3.87 (s, OC**H$_3$**-3 and 5), 3.84 (s, OC**H$_3$**-4), 3.36 (d, J = 6.7 Hz, H-7). ^{13}C NMR (75 MHz, $CDCl_3$): 153.1 (C-3 and C-5), 137.2 (C-8), 136.2 (C-4), 135.8 (C-1), 116.0 (C-9), 105.4 (C-2 and C-6), 60.8 (O**C**H$_3$-4), 56.0 (O**C**H$_3$-3 and 5), 40.55 (C-7).

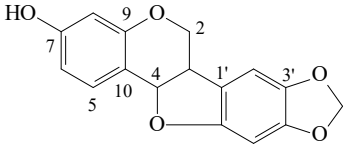

*Maackiain (**2**).* White solid. ^{1}H NMR (300 MHz, $(CD_3)_2CO$, J/Hz): 8.64 (s, OH), 7.31 (d, J = 8.3 Hz, H-5), 6.90 (s, H-2'), 6.57 (dd, J = 8.3 and 2.3 Hz, H-6), 6.40 (s, H-5'), 6.36 (d, J = 2.3 Hz, H-8), 5.93 and 5.91 (s, CH_2O_2), 5.50 (d, J = 6.5 Hz, H-4), 4.29 (dd, J = 10.5 and 3.9 Hz, H-2), 3.65 (t, J = 9.9 Hz, H-2), 3.57 (m, H-3). ^{13}C NMR (75 MHz, $(CD_3)_2CO$: 158.8 (C-7), 156.7 (C-9), 154.4 (C-6'), 147.9 (C-4'), 141.5 (C-3'), 132.1 (C-5), 118.6 (C-1'), 111.8 (C-10), 109.5 (C-6), 105.0 (C-2'), 103.0 (C-8), 101.2 (C-3'and C-4'), 93.0 (C-5'), 78.4 (C-4), 66.0 (C-2), 40.1 (C-3). ESI-MS m/z 283.0661 $[M-H]^-$.

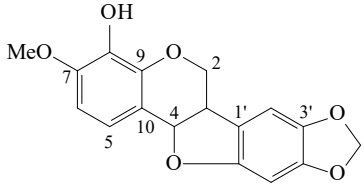

*8-hydroxy-7-methoxy-3',4'-methylenodioxypterocarpan (**3**)*. White solid. ^{1}H NMR (300 MHz, $CDCl_3$, J/Hz): 7.06 (d, J = 8.6 Hz, H-5), 6.74 (s, H-5'), 6.69 (d, 8.6 Hz, H-6), 6.44 (s, H-2'), 5.94 and 5.91 (s, CH_2O_2), 5.54 (d, J = 7.0 Hz, H-4), 4.38 (dd, J = 10.8 and 3.9 Hz, H-2), 3.74 (t, J = 10.8 Hz, H-2), 3.57 (m, H-3). ^{13}C NMR (75 MHz, $CDCl_3$): 154.2 (C-6'), 148.1 (C-4'), 147.3 (C-7), 143.3 (C-9), 141.7 (C-3'), 133.9 (C-8), 121.0 (C-5), 117.6 (C-1'), 113.9 (C-10), 105.0 (C-6), 104.7 (C-2'), 101.3 (C-3'and C-4'), 93.8 (C-5'), 78.3 (C-4), 66.8 (C-2), 56.3 (MeO), 40.2 (C-3). ESI-MS m/z 313.0730 $[M-H]^-$.

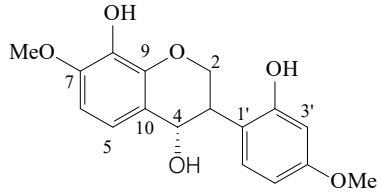

8,4,2' trihydroxy-7,4'-dimethoxyisoflavonol (**4**). Yellow amorphous solid. ^{1}H, ^{13}C NMR, NOESY, HSQC and HMBC (see the spectra below). ESI-MS 341.0994 $[M+Na]^+$.

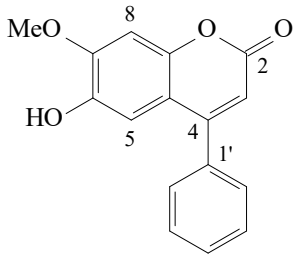

*Dalbergin (**5**)*. Yellow solid. ^{1}H NMR (500 MHz, $CDCl_3$, J/Hz): 7.52 (m, H-3', H-4'and H-5'), 7.52 (m, H-4'), 7.45 (m, H-2' and H-6'), 7.01(s, H-5), 6.92 (s, H-8), 6.27 (s, H-3), 4.01 (MeO-7). ^{13}C NMR (125 MHz, $CDCl_3$): 161.4 (C-2), 155.7 (C-4), 150.1 (C-7), 149.3 (C-9), 142.5 (C-6), 135.6 (C-1'), 129.5 (4'), 128.8 (C-3', C-5'), 128.3 (C-2', C-6'), 112.5 (C-3), 112.3 (C-10), 110.5 (C-5), 99.6 (C-8), 56.4 (MeO-7). ESI-MS m/z 267.0666 $[M+H]^+$.

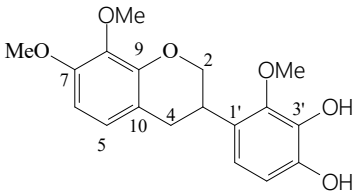

*3',4'-Dihydroxy-7,8,2'-trimethoxyisoflavan (**6**)*. Whith solid. ^{1}H NMR (500 MHz, $CDCl_3$, J/Hz): 6.73 (d, J = 8.3 Hz, H-5), 6.67 (d, J =8.5 Hz, H-5'), 6.63 (d, J =8.5 Hz, H-6'), 6.55 d (d, J = 8.3 Hz, H-6), 4.42 (m, H-2a), 4.03 (t, J =10.3 Hz, H-2b), 3.94 (s, O**C**$\mathbf{H_3}$-8), 3.92 (s, O**C**$\mathbf{H_3}$-2'), 3.91 (s, O**C**$\mathbf{H_3}$-7), 3.59 (m, H-3), 2.95 (m, H-4b), 2.92 (m, H-4a). ^{13}C NMR (125 MHz, $CDCl_3$): 145.7 (C-2'), 147.5 (C-7 and C-9), 139.2 (C-4'), 138.7 (C-3'), 134.9 (C-8), 127.2 (C-1'), 124.2 (C-5), 116.9 (C-6'), 115.3 (C-10), 107.0 (C-6), 106.4 (C-5'), 70.5 (C-2), 61.0 (O**C**H_3-8), 60.9 (O**C**H_3-2'), 56.2 (O**C**H_3-7), 31.6 (C-3), 31.5 (C-4). ESIMS m/z 333.1313 $[M+H]^+$.

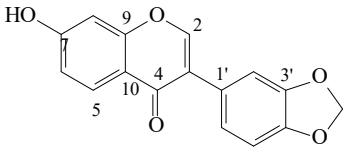

Pseudobaptigenin (**7**). White solid. ^{1}H NMR (500 MHz, C_5D_5N, J/Hz): 8.46 (d, J = 8.7Hz, H-5), 8.19 (s, H-2), 7.49 (d, J = 1.5 Hz, H-2'), 7.26 (dd, J = 8.7 and 2.3 Hz, H-6), 7.25 (d, J = 8.0 Hz, H-5'), 7.15 (d, J = 2.3 Hz, H-8), 7.0 (dd, J = 8.0 and 1.5 Hz , H-6'), 6.00 (s, CH_2O_2). ^{13}C NMR (125 MHz, C_5D_5N): 75.2 (C-4),163.9 (C-7), 158.3 (C-9), 152.7 (C-2), 147.8 (C-3'), 147.6 (C-4'), 127.9 (C-5), 126.6 (C-3), 124.3 (C-1'), 122.6 (C-5'), 117.5 (C-10), 115.7 (C-6), 110.1 (C-2'), 108.8 (C-6'), 102.8 (C-8), 101.4 (C-3',4').

SPECTRA OF THE NEW COMPOUND **4**

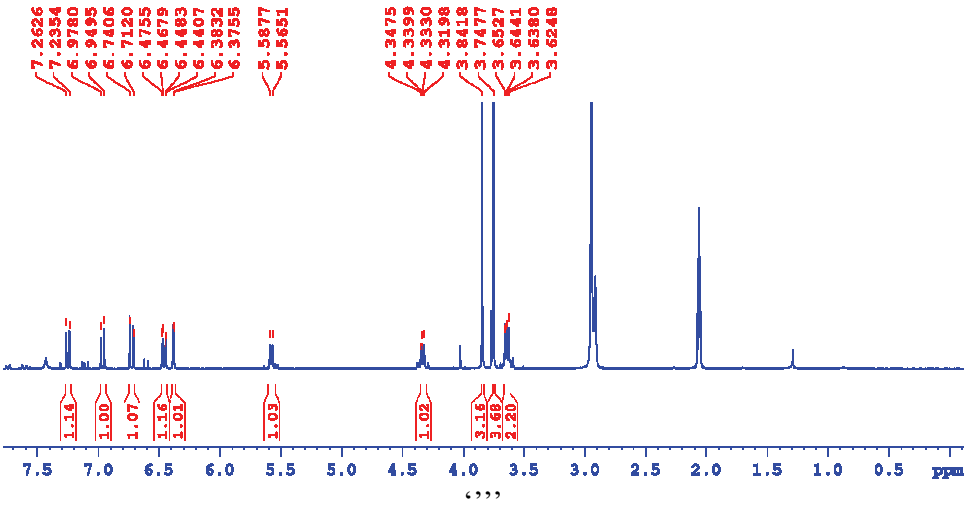

Figure S-1. ^{1}H-NMR spectrum of compound **4**

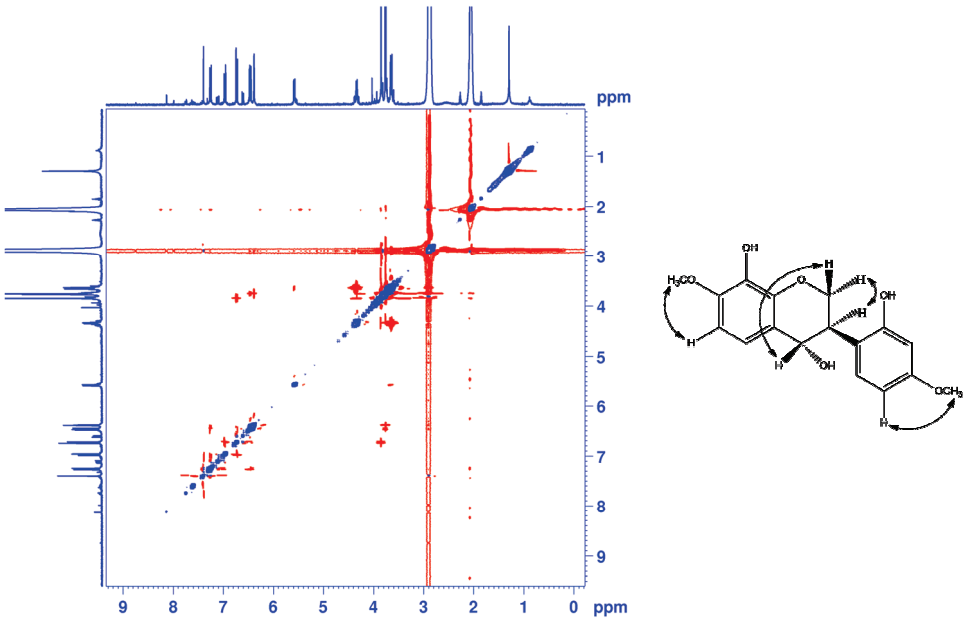

Figure S-2 NOESY spectrum of compound **4**

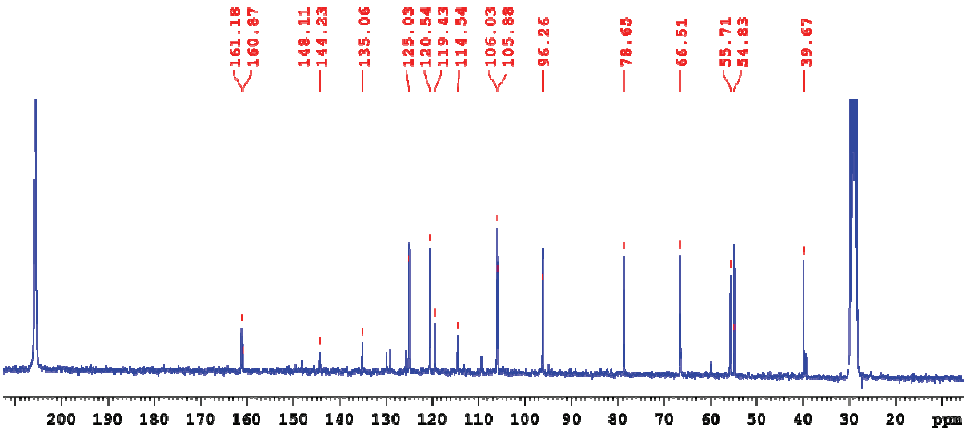

Figure S-3. ^{13}C RMN of compound **4**

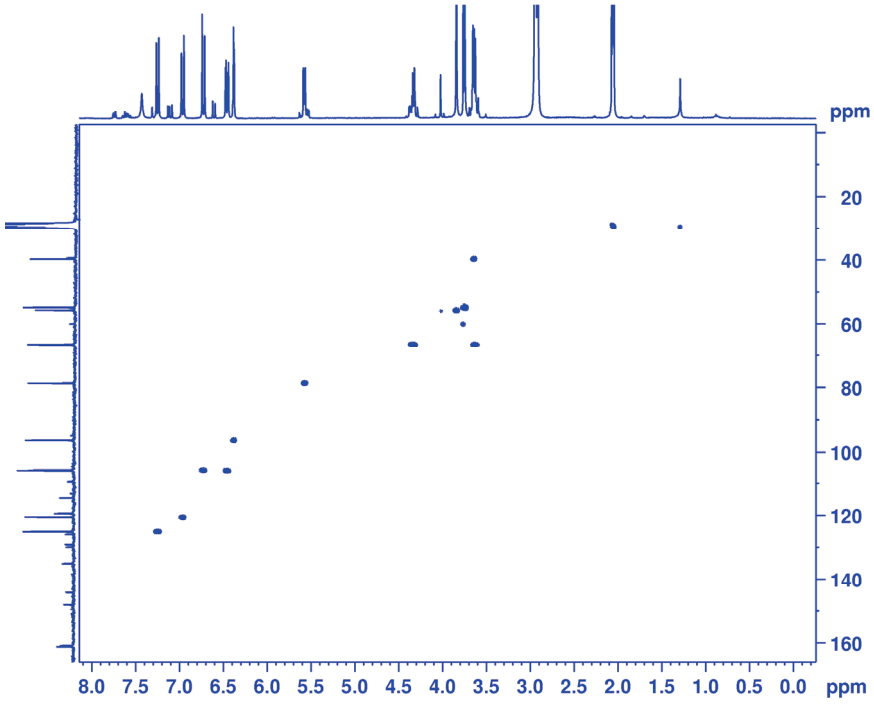

Figure S-4. HSQC spectrum of compound **4**.

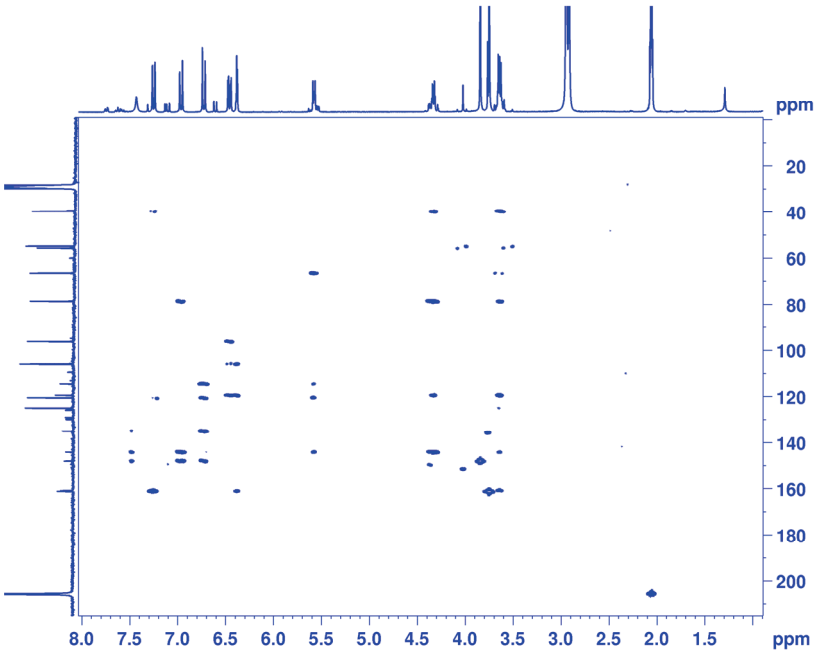

Figure S-5. HMBC spectrum ([300 MHz, 75 MHz $(CD_3)_2CO$]) of compound **4**.

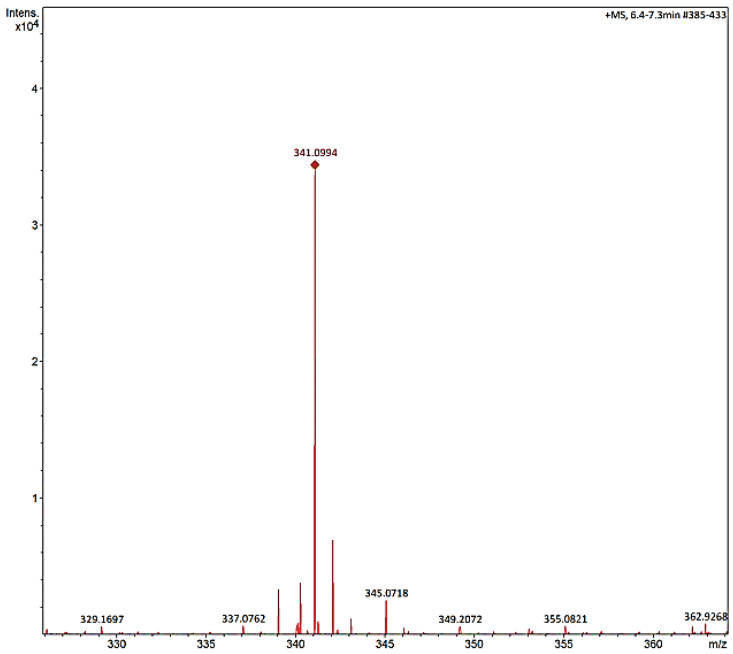

Figure S-6. HR-ESIMS spectrum of compound **4**.

Journal of the Serbian Chemical Society
JSCS-info@shd.org.rs • www.shd.org.rs/JSCS
J. Serb. Chem. Soc. *90* (3) 277–290 (2025)
JSCS–5386
Original scientific paper
Published 24 March, 2025

Investigation of the bioactivities of *Saponaria mesogitana* methanolic extract along with its phytochemical composition

CENNET OZAY[1]*, BURCU CERCI ALKAC[2], AYBALA TEMEL[3] and MELEK PEHLIVAN[4]

[1]*Department of Basic Pharmaceutical Sciences, Faculty of Pharmacy, Izmir Katip Celebi University, Izmir, Türkiye,* [2]*Department of Medical Biology, Faculty of Medicine, Izmir Katip Celebi University, Izmir, Türkiye,* [3]*Department of Pharmaceutical Microbiology, Faculty of Pharmacy, Izmir Katip Celebi University, Izmir, Türkiye and* [4]*Department of Medical Laboratory Techniques, Vocational School of Health Services, Izmir Katip Celebi University, 35620, Izmir, Türkiye*

(Received 26 May, revised 8 August, accepted 15 October 2024)

Abstract: *Saponaria* species are known to contain saponins which have a wide variety of biological activities. But up to now, the phenolic compounds of *Saponaria mesogitana* have not been clarified. Therefore, this study aimed to determine the phenolic composition and some biological activities of *S. mesogitana* for the first time. The antioxidant activities of the methanol and water extracts were assessed using the DPPH, FRAP and *β*-carotene/linoleic acid assays, while the total secondary metabolite content, including phenolics, flavonoids and saponins, was also determined for both extracts. Based on the antioxidant activity and total phenolic and flavonoid contents, further HPLC analysis, as well as anticancer and antimicrobial activity experiments, were conducted using the methanol extract. The anticancer potential was assessed using the MTT assay and wound healing migration test, while antibacterial activity was evaluated through disc diffusion and MIC assays. Additionally, the antibiofilm properties of the extract were examined using the crystal violet method. The methanolic extract showed high antioxidant activity, while caffeic acid and epicatechin were characterized as major phenolic compounds by HPLC. *S. mesogitana* inhibited not only bacterial growth but also the levels of migration of SHSY-5Y cancer cells. These findings indicate that *S. mesogitana* possesses potent antioxidant, anticancer, antimicrobial and antibiofilm activities associated with its bioactive phenolic constituents.

Keywords: HPLC; phenolics; antioxidant; cytotoxic; antimigration; antibiofilm.

* Corresponding author. E-mail: cennet.ozay@ikcu.edu.tr
https://doi.org/10.2298/JSC240526088O

INTRODUCTION

Traditional plant knowledge acquired by a nation for centuries has mostly been passed on to the next generation. This precious knowledge, assembled via ethnobotanical research, is vital for the protection, and for understanding the uses of native and local plants.[1] These days, literature is loaded with accumulating proof highlighting the necessity to incessantly screen medicinal plants to discover key details on their medicinal significance. In fact, within years, the comprehensive growth of nutraceutical, pharmaceutical, cosmeceutical and food industries has dramatically enhanced the requisition for medicinal plants and their bioactive components.[2]

Saponaria L. is a genus of flowering plants belonging to a family commonly known as the pink or the carnation family (Caryophyllaceae), which has 81 genera distributed throughout Mediterranean and temperate regions.[3] The genus *Saponaria* consists of about 40 species worldwide. In Turkey, this genus is represented by 20 species, which is the richest diversity in the world.[4] It has been demonstrated that members of this genus have acaricidal, antibacterial, antioxidant and antiproliferative properties.[5–8] *Saponaria* species, commonly known as soapworts, derive their name from their notable high content of triterpene saponins.[9] These species also include fatty acids, quillaic acid, flavonoids and other phenolic compounds in addition to saponins.[10,6] Phenolic compounds commonly found in plants have a wide range of biological activities, including antioxidant properties.

Antioxidants could prevent the oxidation of biomolecules in food as well as in human cells. Industrial antioxidants are mostly synthetic components that could negatively impact human health. Natural antioxidants are crucial in fight against free radicals, which could be related to many diseases such as Alzheimer's disease, atherosclerosis, emphysema and many forms of cancer.[11] Due to their nature, green plants, fruits and vegetables are often used as primary natural antioxidant sources. Phenolic compounds, found in plant extracts, are known to act as strength-free radical scavengers and exhibit antioxidant properties.[12]

Cancer is a significant global health issue, causing 11 million deaths by 2030.[13] Neuroblastoma is one of the most common pediatric cancer and the prognosis is poor. Neuroblastoma treatment involves chemotherapy, surgery, and radiotherapy. However, systemic toxicity in treatment hinders patient well-being, necessitating a new, affordable approach. Medicinal plants are crucial in cancer drug discovery, as they contain notable anti-cancer agents.[14] The cytotoxic effect of several natural compounds and plant extracts has been shown *in vitro* and *in vivo* studies on neuroblastoma cells.[15,16]

Today, while antibiotic resistance rates are rapidly increasing, the investment made by the pharmaceutical industry in antibiotic discovery is gradually decreasing due to the resistance problem. For this reason, the importance of antimic-

robial effective compounds obtained from natural sources in the treatment of infectious diseases is increasing. In infections caused by multidrug-resistant bacteria, one of the most important factors that increase the virulence of these bacteria is the biofilm structure. Bacterial biofilms mediate recurrent infections and antimicrobial resistance through different mechanisms.[17] Evaluating the antimicrobial and antibiofilm effects of compounds with different chemical groups (such as phenolic compounds) isolated from natural sources, especially plants, is critical for treating infectious diseases.[18]

In this context, *Saponaria* species are one of the plants whose antimicrobial effects have been investigated, and the majority of the studies in the literature are on the *Saponaria officinalis* species. However, there is no previously published data about the biological activity of *Saponaria mesogitana*, as well as its phytochemical composition. Therefore, the potential antioxidant, anticancer, antimicrobial and antibiofilm activities of *S. mesogitana*, were investigated in this study.

EXPERIMENTAL

Plant material and extraction

S. mesogitana was collected at the flowering stage in midsummer 2018 from Isparta, Eğirdir-Turkey, and identified (Voucher No: NS 3050) by Prof. Olcay Dusen, Pamukkale University. The aerial parts of the plant were air-dried in shadow, powdered as a fine grain (10 g), and then extracted with 100 mL methanol and water at 45 °C for 6 h in a controlled shaker. At the end of this period, the mixture was filtered and the filtrate was evaporated under reduced pressure at 37 °C using a rotary evaporator. The water in the extract was freeze-dried under a vacuum at −51 °C and the resultant extracts were stored at −20 °C until use. In the case of the water extract, the rotary evaporation step was omitted, and the lyophilization process was applied directly.[19] The dried extracts were weighed to determine the percent of yield. The percentage yield was obtained using this formula: $100W1/W0$, where $W1$ is the final weight of the extract and $W0$ is the initial weight of the sample.

Determination of total secondary metabolites amount

To obtain total levels of phenolic, flavonoid, and saponin contents in the methanol and water extracts, colorimetric assays were used as described in the previous paper.[20] Folin–Ciocalteu, aluminum colorimetric and vanillin sulphuric acid methods were used to detect total phenolic, flavonoid and saponin contents in the extracts, respectively. These contents were expressed as gallic acid (mg GAE g^{-1}), quercetin (mg QE g^{-1}) and quillaja (mg QAE g^{-1}) equivalents, respectively.

Phenolic compound characterization by HPLC

The phenolic constituents of *S. mesogitana* were analyzed using RP-HPLC (Shimadzu, Japan) with separation conducted at 30 °C on a reversed-phase column (250 mm×4.6 mm, 5 μm, Agilent Eclipse XDB C-18) employing a mobile phase consisting of a mixture of acetic acid (3 %) and methanol. The mobile phase was pumped at a flow rate of 0.8 mL min^{-1}. The polyphenolic chemicals in the methanol extract of *S. mesogitana* were measured in μg g^{-1} and analyzed using a diode array detector at specific wavelengths. Then, retention time and spectrum matching were combined to identify each target chemical.

Antioxidant activity

DPPH radical scavenging antioxidant activity. The capacity of the extracts to eliminate the 1,1-diphenyl-2-picrylhydrazyl (DPPH) radical was determined with the described method with slight modifications.[21] Various concentrations of the extracts were added to the DPPH solution and the mixture was allowed to incubate for 30 min in the dark at room temperature. After incubation, the absorbances were measured at 517 nm. The synthetic antioxidant, butylated hydroxytoluene (BHT) was used as the positive control. The results were indicated as IC_{50}.

β-*Carotene/linoleic acid assay*. The β-carotene test system was used to investigate the extracts' ability to inhibit linoleic acid oxidation with slight modifications to the described method.[21] This method is based on the monitoring of the color opening of *β*-carotene by alkyl peroxides formed by free radical chain reaction by heat and air oxidation of linoleic acid. The results were calculated with the following formula as inhibition rate, %, $100(1 - ((A_C - - A_S)/(A_C^o - A_S^o))$, where A_C and A_C^o were absorbance values initial and final measurement of the control group; A_S and A_S^o were absorbance values of samples or standard, respectively. BHT was used as a standard antioxidant.

Ferric reducing antioxidant power (FRAP) assay. This assay was carried out according to Apak *et al.* with slight modifications.[22] The principle of this method is based on the reduction of a Fe(III)–tripyridyltriazine (TPTZ) complex to Fe(II)–TPTZ in the presence of antioxidants. The results measured at 593 nm are given as equivalent to Trolox (mg TE/g extract).

Cytotoxic activity

The cytotoxic effect of the aerial parts of *S. mesogitana* methanol extract was tested against human neuroblastoma cancer cell line SHSY-5Y using the MTT assay. SHSY-5Y cells were grown in Dulbecco's Modified Eagle Medium (DMEM) supplemented with L-glutamine, penicillin, streptomycin and 10 % heat-inactivated fetal bovine serum (FBS) in a humidified atmosphere of 5 % CO_2 air at 37 °C. SHSY-5Y cells were seeded at a density of 5×10^3 cells/well in 96-well plates and incubated overnight for cytotoxicity experiments. After treatment with extracts (1–100 μg mL^{-1}), MTT solution was added. The formed formazan crystals were dissolved in DMSO, and then absorbance was measured at 570 nm. The control cells were considered 100 % viable, and the IC_{50} value was calculated.[23]

Antimigration activity

The effect of *S. mesogitana* methanol extract on the migration of cells was determined with wound healing migration assay. SHSY-5Y cells were seeded into (2×10^5 cells/well) 6-well plates and after 24 h incubation, wells were scratched straightly with a sterile 200 μL pipette tip. After scratching, cells were washed with serum-free DMEM and treated with IC_{50} concentration (47.68 μg mL^{-1}) of the extract. DMEM supplemented with 10 % FBS was used for the control group. Cells were incubated for 24 h at 37 °C in a humidified, 5 % CO_2 air and photographed under an inverted phase-contrast microscope (Olympus CKX53, Japan) for the comparison of the cell movements.[24] Quantification of the wound area was measured by using the ImageJ/Fiji program, which is a wound healing size tool, allowing for the measure of the wound area and scratch width in μm.

Antibacterial activity

Test microorganisms and mediums. Antibacterial activity profiles of the *S. mesogitana* methanol extract against the American Type Culture Collection (ATCC) bacterial strains Gram-negative (*Escherichia coli* ATCC 25922, *Pseudomonas aeruginosa* ATCC 27853) and Gram-positive (*Staphylococcus aureus* ATCC 29213, *Enterococcus faecalis* ATCC 29212)

were investigated by disc diffusion test and broth microdilution method under the recommendations of the European Committee on Antimicrobial Susceptibility Testing (EUCAST).[25] Bacterial strains were grown on Mueller–Hinton agar (MHA). Mueller–Hinton broth (MHB) and tryptic soy broth with 2 % glucose (TSBG) mediums were used for broth microdilution and biofilm formation experiments, respectively. *E. faecalis* was used as a positive control strain for biofilm quantification experiments.

Disc diffusion method. The extract's antibacterial activity was tested using a Kirby–Bauer disc diffusion susceptibility test, with bacterial suspensions prepared from fresh colonies on MHA and adjusted to 0.5 McFarland turbidity using a densitometer device (Biosan, DEN-1). The suspensions were spread onto agar plates using sterile cotton swabs, and 10 µL of the 40 mg mL^{-1} extract was absorbed into sterile blank discs (6 mm, Oxoid), and the discs were placed on the agar plates. The plates were incubated at 37 °C for 24 h, with ciprofloxacin discs used for internal quality control. The inhibition zone diameters (mm) on agar plates were measured for each strain at the end of the incubation period.

Broth microdilution method. The minimum inhibitory concentrations (*MIC*s) of the extract against bacterial strains were determined by the broth microdilution method.[25] Bacterial strains were grown on MHA, suspended in sterile saline, and diluted. 50 µL of MHB was added to the first wells of 96-well U-bottom microplates, followed by 50 µL of extract, and serial dilutions were prepared using side wells. Bacterial suspensions (50 µL) were inoculated into microplates and incubated at 37 °C for 24 h. The lowest extract concentration that inhibited bacterial growth was determined as the *MIC* value of the extract.

Antibiofilm activity

The antibiofilm effect of the *S. mesogitana* methanol extract was assessed using the spectrophotometric microplate method with crystal violet (CV) staining. First, *E. faecalis* and *S. aureus* were allowed to form mature biofilms on the bottom of the sterile 96-well, F-bottom microplates. TSBG medium (180 µL) and bacterial suspension (20 µL) were added to the wells. The microplates were then incubated at 37 °C for 24 h to enable biofilm formation. Following the aspiration of well contents, 200 µL of extract was added to each well, directly onto the mature bacterial biofilm layer. The microplates were further incubated for 24 h. After the incubation period, the well contents were aspirated, and the microplates underwent CV staining.[26,27] The wells were incubated with 0.1 % CV solution for 15 min, then rinsed with tap water until colorless, dried, and then destained with 200 µL of 95 % ethanol for 15 min.

Spectrophotometric measurements were performed using a microplate reader (CLARIOstar Plus, BMG Labtech, Germany) to obtain the optical density (*OD*) values at 570 nm. To determine the percentages of biofilm inhibition, the *OD* values were used in the following formula:

$$\text{Percentage of biofilm inhibition} = 100(OD_A - OD_B)/OD_A \quad (1)$$

where OD_A: the optical density of biofilm control well without plant extract and OD_B: the optical density in the presence of the plant extract.

The biofilm production capacities for bacterial isolates were categorized according to the following criteria: $OD \leq ODc$: no biofilm production, $ODc < OD \leq (2ODc)$: weak biofilm producer, $(2ODc) < OD \leq (4ODc)$: moderate biofilm producer and $(4ODc) < OD$: strong biofilm producer.

Statistical analysis

Each experiment was done in triplicate. The results obtained are expressed as mean ± standard deviation (*SD*). The IC_{50} values were determined with GraphPad Prism 9 software

(San Diego, CA, USA). Statistical comparisons were performed using an analysis of variance followed by Tukey's post hoc test. The significance was accepted as *p<0.05, ****p<0.0001.

RESULTS AND DISCUSSION

The abundance of peer-reviewed studies on herbs that research groups have published demonstrates the extent to which herbal medicine research is being conducted in this day and age. The ongoing search for novel drugs from plants, despite the abundance of research being conducted, remains a crucial necessity.[28]

One of the most important plant genera with traditional folklore importance is *Saponaria*, which makes it a possible source of bioactive chemicals.[29] In this study, the total phenolic content of *S. mesogitana* extracts was calculated as equivalent to gallic acid, and the highest content was observed in methanol extract (32.28 mg GAE g^{-1}). Our results showed that methanol extract has the highest total flavonoid amount (24.07 mg QE g^{-1}), while water extract has the highest total saponin amount (65.30 mg QAE g^{-1}). The yield of extracts from *S. mesogitana* is listed in Table I. The efficiency of extracts prepared with two solvents with different polarities was calculated. The highest extract amount was obtained from water extract (21.08 %). This result can be related to water highest polarity. However, methanol presents a lower extraction yield with a percentage of 14.80 %.

TABLE I. Extract yield and total secondary metabolites amount of *S. mesogitana* (mean ± *SD*); *TPA:* total phenolic amount; *TFA:* total flavonoid amount; *TSA:* total saponin amount; GAE: gallic acid equivalents; QE: quercetin equivalents; QAE: quillaja equivalents, nd: not detected. In each row, different letters indicate a significant difference (p<0.05)

Parameter	Methanol	Water
Extraction yield, %	14.80±0.10^{a}	21.08±018^{b}
TPA / mg GAE g^{-1}	32.28±0.21^{c}	25.30±0.18^{b}
TFA / mg QE g^{-1}	24.07±0.20^{b}	20.15±0.22^{b}
TSA / mg QAE g^{-1}	48.12±0.33^{c}	65.30±0.52^{d}

To compare the results and produce more accurate data, the antioxidant activity of *S. mesogitana* extracts prepared with methanol and water was assessed using three different methods, including β-carotene/linoleic acid, DPPH and FRAP assay. The methanolic extract showed a slightly higher antioxidant activity than the aqueous extract in all assays. DPPH radical scavenging activity of the extracts was found to be close to the synthetic antioxidant, BHT. Our results suggested that free radical scavenging activities increased with the phenolic contents of the extract. The total phenolic amount of *Saponaria cypria* methanol extract was reported earlier as 13.62 mg GAE g^{-1}.[30] According to this result, *S. mesogitana* methanolic extract had more abundant (32.28 mg GAE g^{-1}) total phenolic amounts than *S. cypria.* Phenolic compounds are known to be molecules with antioxidant activity due to their hydroxyl groups and phenolic rings.[31] The antioxidant activity of the extracts is presented in Table II.

TABLE II. Antioxidant activity of *S. mesogitana* extracts (mean ± *SD*); TE: trolox equivalents. In each row, different letters indicate significant differences ($p<0.05$)

Assay	Methanol	Water	BHT
β-carotene/linoleic acid (inhibition, %)	74.52±1.44^{c}	70.24±1.40^{c}	94.15±1.60^{d}
DPPH (IC_{50} / μg mL^{-1})	11.65±0.09^{b}	13.44±0.10^{b}	10.02±0.07^{a}
FRAP (mg TE g^{-1})	83.17±1.61^{d}	55.31±1.38^{c}	–

Although numerous studies have focused on the saponins of the genus *Saponaria*, research on its phenolic compounds is quite limited.[10,32] Methanol extract was utilized in HPLC analysis and other bioactivity tests since it has a greater antioxidant capacity and total phenolic content than water. To identify the phenolic compounds in the methanolic extracts of the aerial parts of *S. mesogitana*, 15 standard compounds (gallic acid, 3,4-dihydroxybenzoic acid, 4-hydroxybenzoic acid, 2,5-dihydroxybenzoic acid, chlorogenic acid, vanillic acid, epicatechin, caffeic acid, *p*-coumaric acid, ferulic acid, rutin, ellagic acid, naringin, cinnamic acid, quercetin) were used in the HPLC analysis. The phenolic compounds were detected in the extract with varying amounts and have been listed in Table III. According to these results, caffeic acid (11410.76 μg g^{-1}), epicatechin (4394.09 μg g^{-1}), 2,5-dihydroxybenzoic acid (4173.63 μg g^{-1}) and quercetin (1413.89 μg g^{-1}) are most common phenolic compounds of the extract. It has been reported that these phenolics possess antioxidant, anticancer, and antibacterial activities.[33–35]

TABLE III. Phenolic compounds characterization of methanolic *S. mesogitana* extract by HPLC (mean ± *SD*); *RT*: retention time, *LOD*: limit of detection

No.	Identified phenolic compound	*RT* min	UV λ_{max} nm	*LOD* μg mL^{-1}	Content, μg/g extract (mean±*SD*)
1	Gallic acid	6.8	280	0.015	18.63±0.45
2	3,4-Dihydroxybenzoic acid	10.7	280	0.031	09.24±0.16
3	4-Hydroxybenzoic acid	15.7	280	0.014	11.09±0.24
4	2,5-Dihydroxybenzoic acid	17.2	320	0.753	4173.63±65.47
5	Chlorogenic acid	18.2	320	0.011	146.18±1.83
6	Vanillic acid	19.2	320	0.112	802.52±4.87
7	Epicatechin	21.3	260	0.433	4394.09±67.00
8	Caffeic acid	22.7	280	0.018	11410.76±242.4
9	*p*-Coumaric acid	26.1	320	0.020	31.38±0.26
10	Ferulic acid	30.1	320	0.012	608.71±4.12
11	Rutin	45.6	360	0.576	316.91±3.11
12	Ellagic acid	47.7	240	0.455	607.27±4.06
13	Naringin	49.7	280	0.404	88.22±0.62
14	Cinnamic acid	67.8	280	0.016	59.73±0.50
15	Quercetin	71.1	360	0.578	1413.89±14.74

Using herbs and medicinal plants for primary human health care is a universal phenomenon. Today, as much as 80 % of the people in the world depend on traditional medicine as primary health care.[36] Therefore, such plants need to be investigated to understand their chemical constituents and pharmacological activities. *S. mesogitana* is used in folk medicine for kidney stones (as litholytic), joint inflammation, acne, stomach aches and liver diseases.[37] There is no prior research on this plant's ability to fight cancer. To evaluate its anticancer activity, we have chosen SHSY-5Y neuroblastoma cells, which have not previously been studied in the context of this genus. We have selected these cells due to their rapid proliferation, experimental accessibility and established role as a model system in neurodegenerative disease research.[38] MTT assay and wound healing migration assay were used to investigate the plant's anticancer activity. The effect of methanolic extracts of *S. mesogitana* against SHSY-5Y neuroblastoma cells resulted in a concentration-dependent decrease in cell viability. The half--inhibition concentration (IC_{50}) value was determined to be 47.68±2.01 μg mL^{-1} (Fig. 1). According to cell migration results, obtained using wound-healing assay, the extract reduced cell migration in SHSY-5Y cells, compared with the control group. 0 and 24 h images were given in Fig. 2. In this assay, it was observed that the control cells migrated faster than the cells treated with the plant extract when both the differences in the wound areas and the width of the scratch were evaluated, as the control groups and *S. mesogitana*-treated groups were compared (Fig. 3). Wound closure percent was calculated as 63 and 28 % in control and extract-treated cells, respectively. When we compared the cell migration rate (μm/h) between extract-treated and non-treated cells, *S. mesogitana*-treated cells had a rate of 3.5 μm/h while non-treated cells had 4.18 μm/h (Fig. 4).

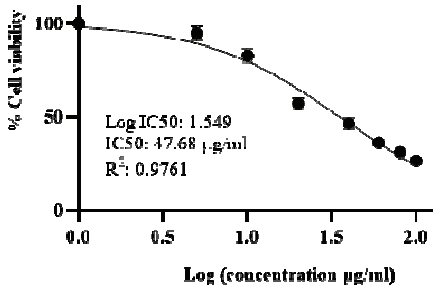

Fig. 1. Percentage cell viability of SHSY-5Y cells treated by *S. mesogitana* extract in different concentrations calculated by MTT assay.

Anticancer activity is attributed to saponins found in the roots of other *Saponaria* species.[10] In this study, the anticancer properties of the extract obtained from the aerial part seem to be related to the phenolic compounds of the plant. We used SHSY-5Y cells to show the effect on the *S. mesoginata* for the first time. We believe that it can be helpful to maintain further studies focused on neuroscience and *S. mesogitana*.

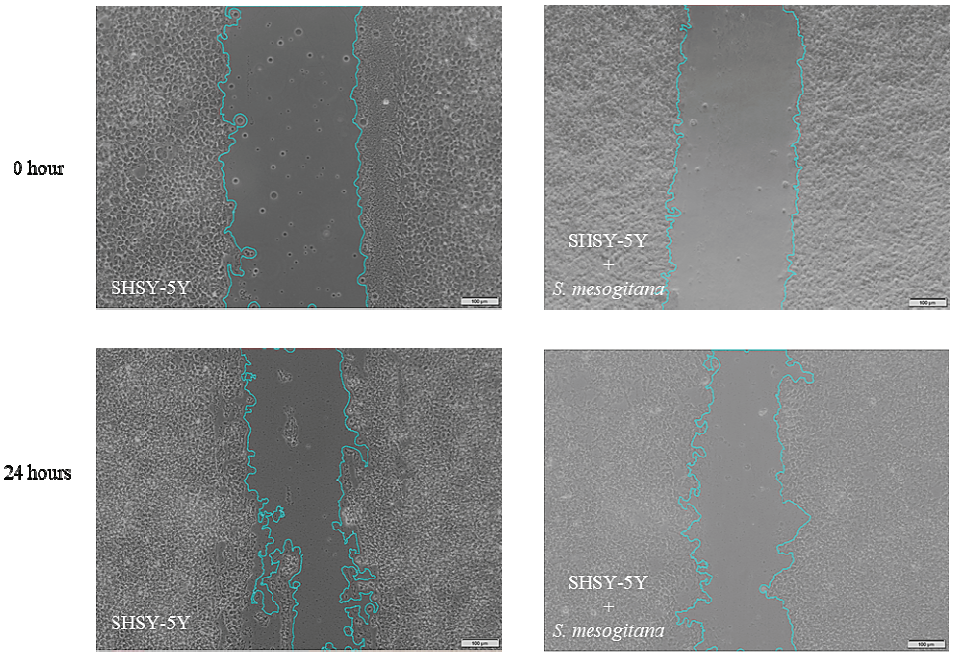

Fig. 2. Wound healing images of SHSY-5Y and SHSY-5Y treated with *S. mesogitana* at 0 and 24 h.

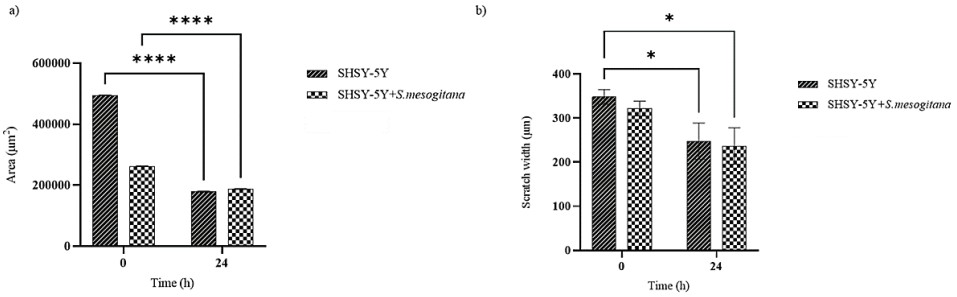

Fig. 3. a) Wound area at time 0 and after 24 h incubation. b) Scratch width at time 0 and after 24 h incubation. *p<0.05, ****p<0.0001.

In the disk diffusion experiments conducted in this study, 11 and 10 mm zone diameters were measured around the extract-containing disks for *S. aureus* and *E. faecalis*, respectively. No inhibition zone was measured for *P. aeruginosa* and *E. coli* strains in Kirby–Bauer disc diffusion susceptibility test. In the line with these results, the broth microdilution method was applied to determine the minimum inhibitory concentrations of the extract against *S. aureus* and *E. faecalis* strains.

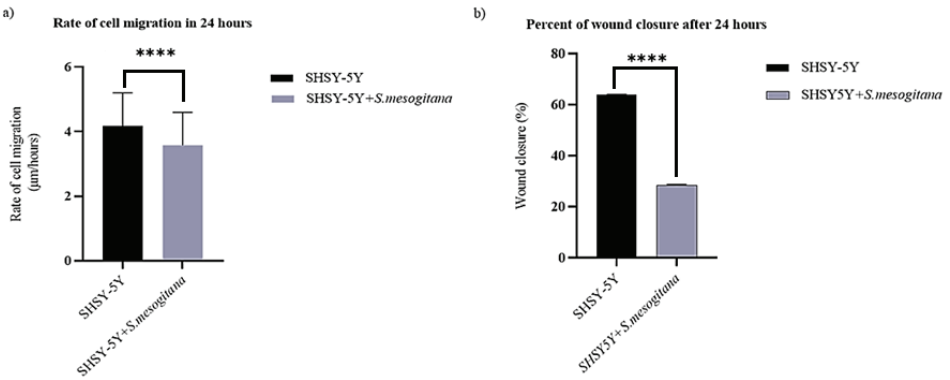

Fig. 4. a) Rate of cell migration in 24 h and b) percent of wound closure. ****p<0.0001.

As a result of broth microdilution assays to determine the antimicrobial activity of *S. mesogitana* extract, the minimum inhibitory concentrations against *S. aureus* and *E. faecalis* bacteria were determined as 1.56 and 0.195 mg mL^{-1} (Table IV). Biofilm quantification and antibiofilm activity of the extract were investigated with the spectrophotometric microplate method. It was determined that biofilm production of *S. aureus* and *E. faecalis* decreased by 69.0 and 85.2 %, respectively, in the presence of the extract.

TABLE IV. The minimum inhibitory concentrations (*MIC*s) and antibiofilm effects of *S. mesogitana*; *OD*: optical density on 570 nm

Bacterial strain	*MIC* mg mL^{-1}	*OD*	Biofilm forming capacity	*OD* in the presence of the extract	Biofilm inhibition, %
S. aureus ATCC 29213	1.56	0.2443	Weak biofilm producer	0.0761	69.0
E. faecalis ATCC 29212	0.195	0.4364	Strong biofilm producer	0.0645	85.2

The zone diameter for *S. aureus* in the methanolic extract for *S. officinalis* was reported as 18 mm by Sengul *et al.* while the zone diameter of the methanol extract against the same bacteria was recorded as 11 mm in our study.[7] Eren *et al.* determined the *MIC* value of *S. officinalis* against *E. faecalis* as 8 mg mL^{-1}, in our study, the *MIC* value for the methanol extract of *S. mesogitana* species against the same bacterial species was detected as lower than 8 mg/mL.[39]

There are several studies in the literature that draw attention to the antimicrobial effects of different *Saponaria* species, especially focused on *S. officinalis*. Similar to our study, previous studies have examined different gram-positive and gram-negative bacterial species and generally reported higher antimicrobial effects of *Saponaria* extracts against gram-positives. Among them, Charalambous *et al.* conducted with *Saponaria cypria* Boiss. root extracts, the *MIC* values

for *S. cypria* methanol extracts against *S. aureus* and *E. faecalis* were 1.563 and 3.125 mg mL^{-1}, respectively.[30] The *MIC* value of *S. mesoginata* species against *E. faecalis* bacteria was much lower in the present study.

The antifungal and antibacterial activities of the *Saponaria prostrata* plant samples against different bacterial and fungal strains were investigated by Aras and Alan.[40] They indicated that the highest antibacterial activity was detected against the *S. aureus* ATCC 25923. It was also reported that the extract did not demonstrate any antimicrobial activity against *E. coli*, *P. aeroginosa*, *C. albicans*, *Y. lipolytica* and *S. cerevicia*. Similarly, we detected no inhibition zone for *S. mesoginata* extract against *P. aeruginosa* and *E. coli* strains in the disk diffusion tests.

To the best of our knowledge, there is no data on the antibiofilm effect of *S. mesogitana*. In this study, in addition to the antimicrobial effect of *S. mesogitana*, its antibiofilm activity against two bacterial strains was also investigated. The effect of *Saponaria* species, including the widely studied *S. officinalis*, on bacterial biofilms is not yet known. Our study is unique in terms of investigating the antibiofilm activity of *S. mesogitana*, and a strong antibiofilm effect was detected on the biofilm structures of *S. aureus* and *E. faecalis* species. In this study, we found that the methanol extract of *S. mesogitana* inhibited biofilm formation at a high level in two tested bacterial strains. The methanol extract of *S. mesogitana* showed an inhibitory effect on *S. aureus* and *E. faecalis* biofilm formation, 80.7 and 85.2 %, respectively (Table IV). These results are promising in terms of benefiting from the potential antibiofilm effect of the extract obtained from *Saponaria* species. Considering that the discovery of new antimicrobial agents is quite limited, and the frequency of infections associated with bacterial biofilms, antibacterial and antibiofilm it is clear that effective extracts/compounds obtained from natural sources are of critical importance.

CONCLUSION

Phytochemicals, a class of bioactive substances found in medicinal plants, have been utilized extensively worldwide to treat a wide range of diseases. Unlike the genus *Saponaria*, which is known for the saponins it contains, the phenolic constituents of the extract obtained from the aerial parts of *S. mesogitana* species belonging to the same genus were investigated for the first time in this study. Besides its phytochemical composition, various pharmacological effects of *S. mesogitana*, including antioxidant, anticancer, antimicrobial and antibiofilm effects are also firstly explored. It can be suggested that the observed biological activities of the extract are due to the presence of different phenolic compounds. Our results showed that *S. mesogitana* could be accepted as a novel and alternative natural source of antioxidative, antitumoral, and antimicrobial agents. For this reason, this plant may contribute to the development of new drug

or food additive formulations. Additionally, such studies are valuable for uncovering the contents of traditional plants. Despite being the first study on this plant, more *in vitro* and *in vivo* research is required to fully grasp its potential.

Acknowledgements. The authors would like to thank Nuray Sarac and Prof Olcay Dusen for the collection and identification of plant material, respectively.

ИЗВОД

ИСПИТИВАЊЕ БИОАКТИВНОСТИ И ФИТОХЕМИЈСКОГ САСТАВА МЕТАНОЛНОГ ЕКСТРАКТА *Saponaria mesogitana*

CENNET OZAY[1] BURCU CERCI ALKAC[2], AYBALA TEMEL[3] и MELEK PEHLIVAN[4]

[1]Department of Basic Pharmaceutical Sciences, Faculty of Pharmacy, Izmir Katip Celebi University, Izmir, Türkiye, [2]Department of Medical Biology, Faculty of Medicine, Izmir Katip Celebi University, Izmir, Türkiye, [3]Department of Pharmaceutical Microbiology, Faculty of Pharmacy, Izmir Katip Celebi University, Izmir, Türkiye u [4]Department of Medical Laboratory Techniques, Vocational School of Health Services, Izmir Katip Celebi University, 35620, Izmir, Türkiye

Врста *Saponaria* садржи сапонине који имају различите биолошке активности. Фенолна једињења *S. mesogitana* нису до сада испитана. У овој студији је одређен фенолни састав и биолошка активност једињења из *S. mesogitana*. Одређена је антиоксидативна активност метанолног и воденог екстракта применом DPPH, FRAP и теста на бази *β*-каротена и линолне киселине, као и садржај укупних секундарних метаболита, укључујући фенолна једињења, флавоноиде и сапонине. На основу антиоксидативне активности и садржаја фенолних једињења и флавоноида, изабран је метанолни екстракт за даљу HPLC анализу и експерименте одређивања антитуморске и антимикробне активности. Антитуморски потенцијал је мерен применом MTT и теста миграције код зарастања рана, а антибактеријски применом теста дифузије на диску и одређивањем *MIC*. Способност екстракта да спречи формирање биофилма одређивана је кристал виолет методом. Метанолни екстракт је испољио велику антиоксидативну активност, а кафеинска киселина и епикатехин су главна фенолна једињења идентификована HPLC методом. *S. mesogitana* је способна да инхибира бактеријски раст, као и миграцију канцерских ћелија SHSY-5Y. Добијени резултати показују да *S. mesogitana* има јаку антиоксидативну, антиканцерску, антимикробну активност и да инхибира стварање биофилма, захваљујући својим фенолним једињењима.

(Примљено 26. маја, ревидирано 8. августа, прихваћено 15. октобра 2024)

REFERENCES

1. A. Akgul, A. Akgul, S. G. Senol, H. Yildirim, O. Secmen, Y. Dogan, *J. Ethnobiol. Ethnomed.* **14** (2018) 12 (https://doi.org/10.1186/s13002-017-0201-8)
2. M. Selseleh, S. N. Ebrahimi, A. Aliahmadi, A. Sonboli, M. H. Mirjalili, *Ind. Crop Prod.* **153** (2020) 112609 (https://doi.org/10.1016/j.indcrop.2020.112609)
3. M. J. Christenhusz, J. W. Byng, *Phytotaxa* **261** (2016) 201 (https://doi.org/10.11646/phytotaxa.261.3.1)
4. A. Dashti, M. Assadi, F. Sharifnia, *Iran J. Bot.* **20** (2014) 146 (https://doi.org/10.22092/IJB.2014.11008)
5. R. Pavela, *Plant Protect. Sci.* **52** (2016) 54 (https://doi.org/10.17221/62/2015-PPS)

6. G. B. Endonova, T. P. Antsupova, S. D. Zhamsaranova, D. V. Lygdenov, *Biosci. Biotech. Res. Asia* **12** (2015) 2017 (http://dx.doi.org/10.13005/bbra/1869)
7. M. Sengul, S. Ercişli, H. Yildiz, N. Gungor, A. Kavaz, B. Çetin, *Iran. J. Pharm. Res.* **10** (2011) 49 (https://www.ncbi.nlm.nih.gov/pmc/articles/PMC3869595/)
8. J. J. Balsevich, I. Ramirez-Erosa, R. A. Hickie, D. M. Dunlop, G. G. Bishop, L. K Deibert, *Fitoterapia* **83** (2012) 170 (http://dx.doi.org/10.1016/j.fitote.2011.10.010)
9. J. P. Vincken, L. Heng, A. de Grot, H. Gruppen, *Phytochem*. **68** (2007) 275 (http://dx.doi.org/10.1016/j.phytochem.2006.10.008)
10. Y. Lu, D. Van, L. Deibert, G. Bishop, J. Balsevich, *Phytochem*. **113** (2015) 108 (http://dx.doi.org/10.1016/j.phytochem.2014.11.021)
11. B. Akbari, N. Baghaei-Yazdi, M. Bahmaie, F. Mahdavi Abhari, *BioFactors* **48** (2022) 611 (https://doi.org/10.1002/biof.1831)
12. Q. Z. Lv, J. T. Long, Z. F. Gong, K. Y. Nong, X. M. Liang, T. Qin, W. Huang, L. Yang, *Nat. Prod. Commun*. **16** (2021) 1 (https://doi.org/10.1177/1934578x211027745)
13. P. B. Benil, P. Nimisha, S. Arokiyaraj, R. Rajakrishnan, A. Alfarhan, A. Al-Ansari, *J. King Saud Univ. Sci.* **32** (2020) 2582 (https://doi.org/10.1016/j.jksus.2020.04.016)
14. A. Lichota, K. Gwozdzinski, *Int. J. Mol. Sci.* **19** (2018) 3533 (https://doi.org/10.3390/ijms19113533)
15. F. Morandi, V. Bensa, E. Calarco, F. Pastorino, P. Perri, M. V. Corrias, M. Ponzoni, C. Brignole, *Nutrients* **13** (2021) 2178 (https://doi.org/10.3390/nu13072178)
16. A. Kafoud, Z. Salahuddin, R. S. Ibrahim, R. Al-Janahi, A. Mazurakova, P. Kubatka, D. Büsselberg, *Biomol.* **13** (2023) 563 (https://doi.org/10.3390/biom13030563)
17. E. Önem, A. G. Özaydın, H. C. Sarısu, *Braz. J. Pharm. Sci.* **59** (2023) e20412 (http://dx.doi.org/10.1590/s2175-97902023e20412)
18. S. M. Mandal, R. O. Dias, O. L. Franco, *J. Med. Food* **20** (2017) 1031 (https://doi.org/10.1089/jmf.2017.0017)
19. C. Ozay, R. Mammadov, *Acta Biol. Hung*. **68** (2017) 310 (https://doi.org/10.1556/018.68.2017.3.8)
20. R. Mammadov, A. Kaska, C. Ozay, *Indian J. Pharm. Sci.* **79** (2017) 585 (https://doi.org/10.4172/pharmaceutical-sciences.1000266)
21. C. Ozay, *Riv. Ital. Sostanze Gr*. **100** (2023) 177 (https://www.innovhub-ssi.it/kdocs/2108136/2023_risg_100_3_4_ozay.pdf)
22. R. Apak, M. Özyürek, K. Güçlü, E. Çapanoğlu, *J. Agric. Food Chem.* **64** (2016) 997 (https://doi.org/10.1021/acs.jafc.5b04739)
23. I. Urkmez, H. I. Karahan Coven, A. Eldem, M. Pehlivan, *Eur. J. Biol.* **81** (2022) 251 (https://doi.org/10.26650/EurJBiol.2022.1167842)
24. N. Şirin, L. Elmas, M. Seçme, Y. Dodurga, *Gene* **737** (2020) 144428 (https://doi.org/10.1016/j.gene.2020.144428)
25. EUCAST. The European Committee on Antimicrobial Susceptibility Testing, *Breakpoint tables for interpretation of* MIC*s and zone diameters*, version 13.0, 2023 (http://www.eucast.org)
26. S. Stepanović, D. Vuković, V. Hola, G. Di Bonaventura, S. Djukić, I. Cirković, F. Ruzicka, *APMIS* **115** (2007) 891 (https://doi.org/10.1111/j.1600-0463.2007.apm_630.x)
27. A. Temel, B. Erac, *Curr. Microbiol.* **79** (2022) 256 (https://doi.org/10.1007/s00284-022-02943-0)

28. D. B. Singh, R. K. Pathak, D. Rai, *Rev. Bras. Farmacogn.* **32** (2022) 147 (https://doi.org/10.1007/s43450-022-00235-z)
29. S. Chandra, D. S. Rawat, *Integr. Med. Res*. **4** (2015) 123 (https://doi.org/10.1016/j.imr.2015.06.004)
30. D. Charalambous, M. Christoforou, E. N. Kitiri, M. Andreou, D. Partassides, C. Papachrysostomou, M. Frantzi, G. A. Karikas, M. Pantelidou, *Molecules* **27** (2022) 5812 (https://doi.org/10.3390/molecules27185812)
31. N. Kumar, N. Goel, *Biotechnol. Rep.* **24** (2019) e00370 (https://doi.org/10.1016/j.btre.2019.e00370)
32. W. Smułek, A. Zdarta, A. Pacholak, A. Zgoła-Grześkowiak, Ł. Marczak, M. Jarzębski, E. Kaczorek, *Colloids Surf., B:* **150** (2017) 209 (https://doi.org/10.1016/j.colsurfb.2016.11.035)
33. M. Aijaz, N. Keserwani, M. Yusuf, N.H. Ansari, R. Ushal, P. Kalia, *Biointerface Res. Appl. Chem*. **13** (2022) 324 (https://doi.org/10.33263/BRIAC134.324)
34. Z. Qu, A. Liu, P. Li, C. Liu, W. Xiao, J. Huang, Z. Liu, S. Zhang, *Crit. Rev. Food Sci. Nutr.* **61** (2021) 211 (https://doi.org/10.1080/10408398.2020.1723057)
35. W. Sun, M. H. Shahrajabian, *Molecules* **28** (2023) 1845 (https://doi.org/10.3390/molecules28041845)
36. N. Kimutai, *WJPPS* **6** (2017) 144 (https://doi.org/10.20959/wjpps20176-9263)
37. H. Azaizeh, B. Saad, K. Khalil, O. Said, *Evid. Based Comp. Alternat. Med.* **3** (2006) 229 (https://doi.org/10.1093/ecam/nel034)
38. J. Kovalevich, D. Langford, in: S.,Amini, M. White, Eds., *Neuronal Cell Culture, Methods in Molecular Biology,* Humana Press, Totowa, NJ, 2013, pp. 9–21 (https://doi.org/10.1007/978-1-62703-640-5_2)
39. M. M. Eren, B. Dikmen, C. Vatansever, H. Servi, H. C. Yeğin, G. Ozan, *Ann. Med. Res.* **28** (2021) 516 (https://dx.doi.org/10.5455/annalsmedres.2020.05.487)
40. A. Aras, Y. Alan, *Erzincan Uni. J Sci. Tech.* **15** (2022) 135 (https://doi.org/10.18185/erzifbed.995560).

Journal of the Serbian Chemical Society
JSCS-info@shd.org.rs • www.shd.org.rs/JSCS
J. Serb. Chem. Soc. *90* (3) 291–303 (2025)
JSCS–5387
Original scientific paper
Published 24 March, 2025

A computational study of the potential bioactivity of hibiscus and garcinia acids against SARS-CoV-2

WENDOLYNE LÓPEZ-OROZCO, LUIS HUMBERTO MENDOZA-HUIZAR*, GIAAN ARTURO ÁLVAREZ-ROMERO and J. DE JESÚS MARTIN TORRES-VALENCIA

Área Académica de Química, Universidad Autónoma del Estado de Hidalgo, carretera Pachuca–Tulancingo, 42184, Mineral de la Reforma, Hidalgo, México

(Received 28 April, revised 5 June, accepted 21 August 2024)

Abstract: A computational chemical study was conducted on the diastereoisomers of hibiscus acid (HA) and garcinia acid (GA), investigating their docking capabilities with the main protease (6LU7) of SARS-CoV-2. Electrostatic potential mappings unveiled negative charges associated with the carboxyl and hydroxyl groups positioned at C-2 and C-3 for both hibiscus and garcinia acids. However, the presence of more negative potentials around C-2 and C-3 of hibiscus acid, compared to garcinia acid, suggests that substituents in the (2*S*,3*R*) configuration possess a stronger electron-attracting capacity than those in the (2*S*,3*S*) configuration. Molecular docking studies indicated that both hibiscus acid and garcinia acid bind to the main protease through the catalytic pocket. Nonetheless, molecular dynamics simulations revealed that only HA remained bound to the active site for 100 ns with an *RMSD* of less than 1 Å, whereas GA dissociated from the complex within the initial 16 ns. These findings illuminate the differential binding behaviors of the two compounds, with implications for potential therapeutic interventions against SARS-CoV-2. These findings shed light on the differential binding behaviors of the two compounds, holding implications for potential therapeutic interventions against SARS-CoV-2.

Keywords: 6LU7; hibiscus; molecular docking; molecular dynamics.

INTRODUCTION

The rapid spread of the COVID-19 pandemic over the past three years has highlighted the urgent need for developing effective treatments for this and other diseases. This is possible, if effective and specific drugs are available against specific viruses or bacteria. Nevertheless, it is well known that the design and synthesis of specific drugs may take several decades. Different strategies have been employed in the discovery of antiviral drugs against COVID-19.[1] These strategies encompass drug repurposing, where approved or investigational drugs

* Corresponding author. E-mail: hhuizar@uaeh.edu.mx
https://doi.org/10.2298/JSC240428074L

are utilized beyond their original indications, alongside high-throughput screening, computer-assisted virtual screening and structure-based drug discovery among others.[1–3] In this regard, natural sources like plants and fruits may contain bioactive compounds that have antiviral, antibiotic or anti -inflammatory properties useful against different diseases.[4,5] It could lead to the development of alternative treatments, which may become more accessible and affordable in a shorter time. Thus, research on medicinal compounds of natural origin may lead to the discovery of substances with antiviral or immunomodulatory properties, which could be crucial for the development of effective treatments against SARS-CoV-2 and its variants.[5–12]

Phytochemicals derived from *Hibiscus sabdariffa* [13–22] and compounds extracted from garcinia species,[23–33] have been analyzed employing experimental and computational approaches because have shown therapeutic potential against SARS-CoV2.[5–12] In this sense, it has been reported that the *Garcinia kola*, *Garcinia cambogia*, *Garcinia mangostana* and *H. sabdariffa* extracts are able to reduce cytokine storms during the late phase of SARS-CoV-2 infections by decreasing S1-glycoprotein secretion.[16,23] In addition, the therapeutic use of *H. sabdariffa* in controlling the inflammatory response against COVID-19 by blocking the ACE-2 receptor has been proposed because it contains a number of compounds structurally similar to hydroxychloroquine and mannose,[15,16,34] that could act as agonists for ACE2 and MLB receptors.[15] Also, in silico studies have allowed for the analysis of the interactions of bioactive compounds like mangiferin present in *G. mangostana* with the receptors spike RDM, helicase, 3CLpro and RdRp of SARS-CoV-2,[24,28,35–37] and the biomolecules present in *H. sabdariffa* with 3CLpro and PLppo.[13,16–18,20,22] In summary, the results indicate that various molecules from *H. sabdariffa* and *Garcinia* species exhibit strong binding affinity to the main proteases of SARS-CoV-2, suggesting their potential therapeutic use against SARS-CoV-2 infection.

Specifically, hibiscus acid (HA, (2*S*,3*R*)-3-hydroxy-5-oxooxolane-2,3-dicarboxylic acid), see Fig. 1a, which is found in *H. sabdariffa*,[38] and *Hibiscus schizopetalus*[39] and garcinia acid (GA, (2*S*,3*S*)-3-hydroxy-5-oxooxolane-2,3-dicarboxylic acid)), see Fig. 1b (present in *G. cambogia*),[38,40] have been shown to have a vasorelaxant effect in addition to inhibiting the neuraminidase of influenza.[41,42] Also, it has recently been reported that their anti-inflammatory and antioxidant properties are able to treat the symptoms of COVID-19.[16,20,22] Additionally, isolated HA has proven to be neither clastogenic nor cytotoxic,[38] whereas *G. kola* extract has shown antigenotoxic activity and the ability to repair damage caused by mutagenic agents.[23] Thus, in this study, we analyze the binding of HA and GA to the Mprotease of SARS-CoV-2 through molecular docking to identify whether HA and GA are suitable candidates for acting as antiviral medicines against SARS-CoV-2. Additionally, we conducted dynamic molecular (MD) stu-

dies. We believe that this research may prove valuable in understanding the role of HA and GA in inhibiting the ACE2 receptor for SARS-CoV-2.

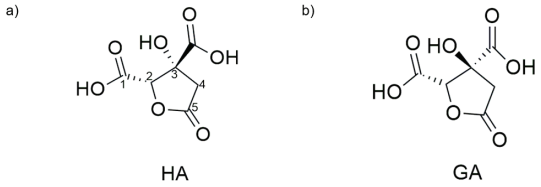

Fig. 1. Chemical structure of hibiscus acid ((2*S*,3*R*)-3-hydroxy-5-oxooxolane-2,3-dicarboxylic acid) and garcinia acid ((2*S*,3*S*)-3-hydroxy-5-oxooxolane-2,3-dicarboxylic acid).

EXPERIMENTAL

The HA and GA structures were subjected to full geometrical optimization employing the B3LYP/6-311G (d,p) level of theory.[43] Vibrational frequencies were calculated to ensure that the stationary points correspond to a minimum on the potential energy surface. Protein––ligand docking studies of the HA and GA ligands with the 3CL-M^{pro} enzyme of SARS-CoV-2 (PDB ID: 6LU7) were performed *via* the web server SwissDock.[44] Visualizations of the protein–ligand complex were performed through the programs Chimera[45] and Discovery Studio Visualizer 2019,[46] while molecular dynamics calculation and visualization were performed using the programs GROMACS[47] and VMD,[48] respectively. The OPLS/AA force field was employed in all of the MD simulations.[49] To perform the MD study, a simulation box was generated, and the complex protein–ligand was placed in the center of the box. At least 1.0 nm from the rim of the protein ligand to the boundary of the cubic box was kept and it was filled with water molecules modelled using the TIP_3P equation.[50] Also, 4 Na^+ for both molecules were added to the simulation box to equilibrate the charges in the system. The integration of the motion equations was performed at a time step of 2 fs with fully periodic boundary conditions (PBC). Prior to the MD simulation, an energy minimization process was performed to ensure a reasonable starting structure in terms of geometry and solvent orientation. Then equilibration was conducted in two stages. The first one was conducted under an NVT ensemble until the temperature of the system reached a plateau at the desired value. In the second one, the equilibrium of pressure was conducted under an NPT ensemble for 1 ns. Then a MD for 100 ns was conducted to analyze the stability of the protein–ligand complex.

RESULTS AND DISCUSSION

Lipinski's rule of five and ADMET prediction

By predicting the physicochemical and pharmacological properties of compounds, it is possible to evaluate the ability of molecules as potential drugs using parameters related to their oral bioavailability and their administration in the body. Lipinsky's rule of five and the ADMET parameters of HA and GA were evaluated using ADMETlab 2.0,[51] see Table I. HA and GA obey Lipinsky's rule of five, which includes the following properties (optimal values in parentheses):[52] log *P* from –0.40 to –0.33 (<5), number of AHB hydrogen bond acceptors of 7 (<10), number of DHB hydrogen bond donors equal to 3 (<5), number of rotational bonds equal to 2 (<10), and molecular weight of 190 g/mol

(<500). On the other hand, the two acids showed Caco-2 permeability and total clearance values lower than the limit. However, they do not show hepatoxicity, mutagenicity, oral toxicity in rats or carcinogenicity. Also, they have a good half--life. Finally, for their metabolism, it was predicted that the acids would act as substrates for the cytochrome P450 C9 subtype.

TABLE I. *In silico* study of the ADMET properties of hibiscus acid and garcinia acid

Property	Model name	Optimum value	Hibiscus acid	Garcinia acid
Absorption	Caco-2 permeability	>–5.15 (log (*Papp* in 10^{-6} cm/s))	–6.105	–6.139
	Intestinal absorption (human)	% Absorbed	0.176	0.029
Distribution	Plasma protein binding	<90 %	13.24	15.37
	Volume distribution	0.04-20 L / Kg	0.218	0.281
Metabolism	CYPA2 Inhibitor	Categorical (Yes/No)	No	No
	CYPA2 Substrate		No	No
	CYP2C19 Inhibitor		No	No
	CYP2C19 Substrate		No	No
	CYP2C9 Inhibitor		No	No
	CYP2C9 Substrate		Yes	Yes
	CYP2CD6 Inhibitor		No	No
	CYP2CD6 Substrate		No	No
	CYP3A4 Inhibitor		No	No
	CYP3A4 Substrate		No	No
Excretion	Clearance	High >15 Moderate 5–15 Low <5 (log ml min^{-1} kg^{-1})	1.894	2.176
	$T_{1/2}$	Long half-life > 3h Short half-life < 3h	0.825	0.727
Toxicity	Human hepatotoxicity	Category: positive, negative	Negative	Negative
	AMES toxicity		Negative	Negative
	Rat oral acute toxicity	Low 0 High 1 (log mg kg_bw^{-1} day^{-1}	0.01	0.011
	Carcinogenicity	Probability	0.009	0.014

Analysis of interfering compounds

Molecules that contain substructures with a high potential to interfere with biological assays are known as Pan-assay interference compounds (PAINs).[53] Although this is not valid in all cases, care should be taken if an active compound contains some substructures.[53] In this sense, there are databases that allow the comparison of compounds with known PAIN molecules. In the present work, the structures of hibiscus acid and garcinia acid were analyzed using the ZINC database,[54] and no interfering structures or substructures were identified in either case.

Mapping of the electrostatic potentials

Understanding the electrostatic potential of molecules is crucial for elucidating their interaction mechanisms, especially in the context of ligand–protein binding. Electrostatic interactions play a significant role in molecular recognition and binding processes. Fig. 2 shows the MEP of the molecules hibiscus acid and garcinia acid evaluated at the B3LYP/6-311G (d,p) level of theory. In this figure, the negative potential areas (red color) represent electron-abundant zones, while the positive potential areas (blue color) show a relative lack of electrons. Note the presence of negative potential areas, particularly around the carboxyl and hydroxyl groups, which suggests regions of high electron density that could participate in interactions with positively charged residues on the protein surface. From Fig. 2, the carboxyl and hydroxyl groups at C-2 and C-3 of HA exhibit more negative potential values than those of GA, indicating that the substituents in the (2*S*,3*R*) conformation are more electrophilic compared to those in the (2*S*,3*S*) conformation.

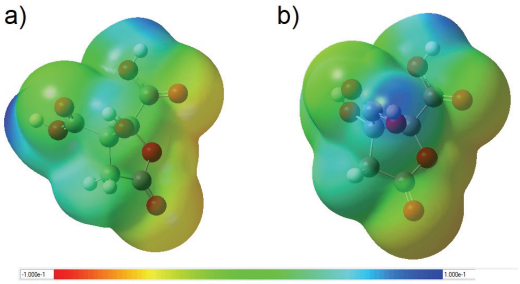

Fig. 2. Mapping of the electrostatic potentials evaluated at the B3LYP/6-311G (d,p) level of theory on a density isosurface (valor = 0.002 e/a.u.^{3}) for: a) HA and b) GA.

Docking study

In order to analyze the ability of HA and GA to inhibit the replication of SARS-CoV-2, A molecular docking study was performed to study the binding of HA and GA to the main protease (6LU7) of this virus, see Figs. 3 and 4. Since 6LU7 has been identified as a target for inhibition of viral replication, Fig. 3a shows the HA-6LU7 configuration, where the binding energy was –6.76 kcal* mol^{-1} and Fig. 4a shows the GA-6LU7 configuration. Garcinia acid interacts with 6LU7 with a binding energy of –6.93 kcal mol^{-1}. These binding energy values compare favorably with those found for caffeoylshikimic acid, chlorogenic acid, cianidanol and kaempferol when they are docked with strong affinity to the 3CLpro main protease of SARS-CoV-2.[13] Also, the delta energy binding may be associated with the formation of different numbers of hydrogen bonds and

* 1 kcal = 4184 J

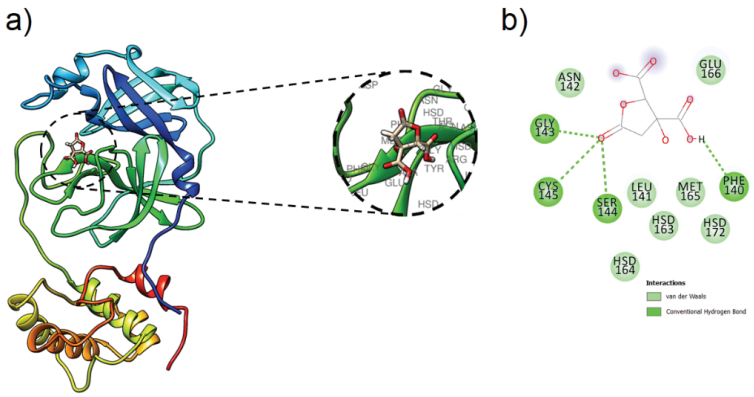

Fig. 3. a) HA binding site in the 6LU7 of SARS-CoV-2, b) 2D mapping of ligand/6LU7 configuration interactions for HA.

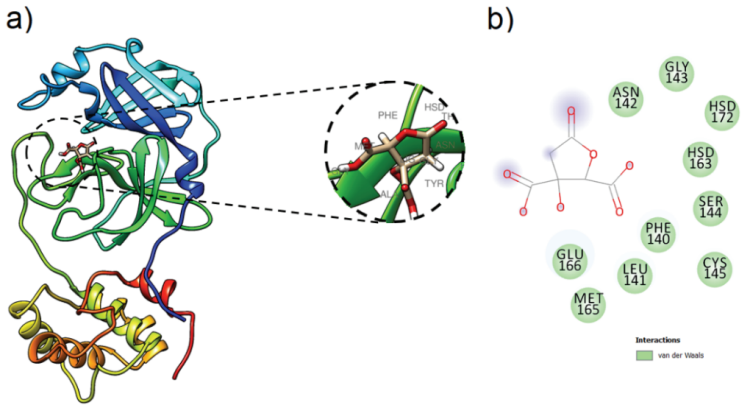

Fig. 4 a) GA binding site in the 6LU7 of SARS-CoV-2, b) 2D mapping of ligand/6LU7 configuration interactions for GA.

interactions between ligand and receptor, caused by the change in the orientation of the carbonyl substituent in HA and GA diasteroisomers. Similar behavior has been observed in the case of diastereomers of nelfinavir, which are identified as potent inhibitors of dimeric SARS-CoV-2 M^{pro},[55] hydrazones *trans*-E and *cis*-E when docked into the binding pocket of 7BQY protease,[56] and remdesivir diastereoisomeric derivatives.[57] In this sense, the Gibbs energy change of binding between an antigen and its receptor is of great relevance for the interaction and entry of a virus into its host on the cell surface.[58–62] Due to infecting a host cell, the virus must have an antigen with a negative Gibbs energy change of binding to the host cell receptor, *e.g.*, the glycoprotein in the receptor for SARS--CoV-2.[63] According to biothermodynamics, the Gibbs free energy change of binding involved in virus–host interactions at the membrane level can help to

better understand these interactions.[58] Thus, a higher Gibbs free energy change of binding results in a faster binding rate, more rapid entry of viruses into host cells, and therefore increased infectivity.[62] Based on the above and the fact that HA and GA show negative Gibbs binding energy change with 6LU7, it is possible to suggest that these diastereoisomers can bind to 6LU7 to inhibit the SARS-COV-2 virus. In addition, the interactions around 3 Å were identified, and a 2D plot was performed as shown in Figs. 3b and 4b. It is observed that hibiscus acid and garcinia acid have van der Waals interactions with residues of the catalytic site of 6LU7 reported,[64] ASN142, HSD163, MET165 and GLU166. Interestingly, the (2*S*,3*S*) conformation of garcinia acid improves the complex interactions and favors hydrogen bond stabilization with PHE140[O–H···N] and the catalytic dyad residue CYS145[O···N] with a distance of 4.74 and 4.13 Å.

Molecular dynamics simulation study

To analyze whether the HA-6LU7 and GA-6LU7 complexes derived from the docking study are stable, we performed a molecular dynamics study at 100 ns. Fig. 5 depicts the docked structures at 0 and 100 ns, respectively, for the docking of garcinia acid at the 6LU7 site. It is clear that GA is not stable at the initial pocket site (see Fig. 5a and b), because GA docked at the original site (Fig 5a), and at the end of 100 ns, it docked at a new site (see Fig. 5b). This can also be seen in the *RMSD* plot (Fig. 5c), where at approximately 16 ns the *RMSD* increases significantly, greater than 3 Å, suggesting the mobilization of garcinia acid away from another active site, which has not been identified with the associated site in 6LU7 to prevent SARS-COV-2 virus replication.

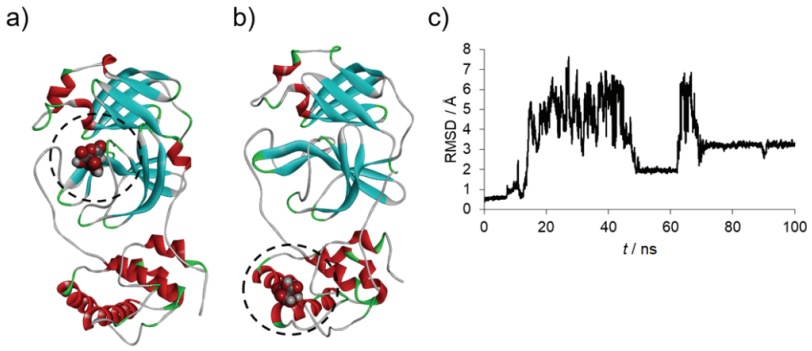

Fig. 5. Molecular dynamics simulation results for GA: a) initial docking configuration, b) docking configuration at 100 ns and c) The *RMSD* profile depicts the equilibrium trajectory of the GA-6LU7 complex through 100 ns.

In the case of the HA-6LU7 complex, in Fig. 6, the structures HA docked at 6LU7 are shown at 0 and 100 ns, respectively. It is clear that HA remains in the pocket site during the 100 ns, suggesting that the complex formed is stable (see

Fig. 6a and b). The last one is corroborated by the *RMSD* graph (Fig. 6c), which shows that the *RMSD* is less than 1 Å. The last results suggest the formation of the HA-6LU7 complex is stable.

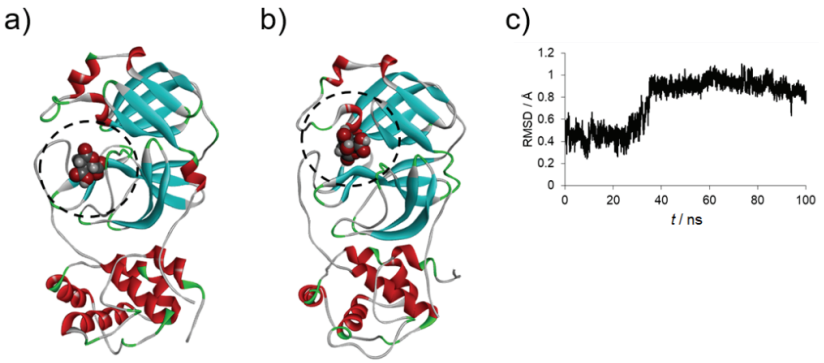

Fig. 6. Molecular dynamics simulation results for HA: a) initial docking configuration, b) docking configuration at 100 ns and c) the *RMSD* profile depicts the equilibrium trajectory of the HA-6LU7 complex through 100 ns.

In addition, Fig. 7 shows the behavior of the potential energy of the complexes during the MD simulation. It can be seen that the potential energies of the GA-6LU7 and HA-6LU7 complexes are in the range of $–9.49\times10^5$ to $–9.43\times10^5$ kJ mol$^{–1}$ and reach a constant level from the beginning of the simulation. The latter illustrates the energetically stable nature of the GA-6LU7 and HA-6LU7 complexes.

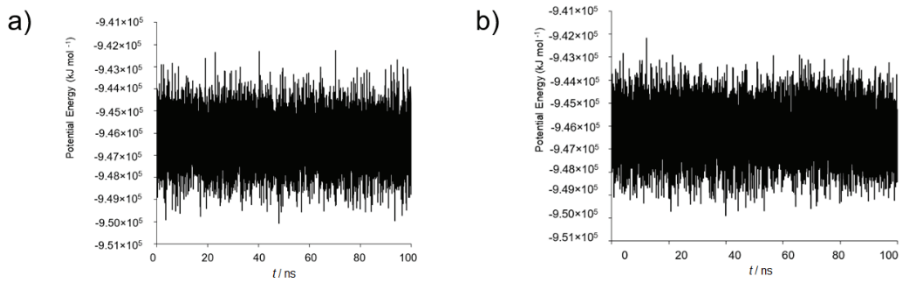

Fig 7. Potential energy graph illustrates the energetic stability of: a) GA and b) HA.

CONCLUSION

Binding pose and binding energy were also analyzed for the HA-6LU7 and GA-6LU7 configurations, where the formation of the complex at the active site position was confirmed, with binding energies equal to –6.76 kcal mol$^{–1}$ and –6.93 kcal mol$^{–1}$, respectively. Analysis of the interactions between HA and GA with 6LU7 revealed that HA shows van der Waals-type interactions with

ASN142, HSD163, MET165 and GLU166, and in the case of garcinia acid, the interactions were with residues PHE140 [O–H·N·] and CYS145 [O–H·N·]. Finally, by molecular dynamics simulation, it was possible to verify the permanence of hibiscus acid in the active site of 6LU7, whereas garcinia acid did not remain in the protease active site.

Acknowledgements. WLO acknowledges CONACYT for the scholarship granted for Doctoral studies. L. H. M. H. thankfully acknowledges the computer resources, technical expertise and support provided by the Laboratorio Nacional de Supercómputo del Sureste de México, CONACYT member of the network of National laboratories through the project No. 202501011N. The authors thank to the Universidad Autónoma del Estado de Hidalgo for the funding granted for this work through Project PAO-2022-1389 UAEH. LHMH, GAAR and JJMTV acknowledge to the SNI for the distinction of their membership and the stipend received.

ИЗВОД

РАЧУНАРСКА СТУДИЈА ПОТЕНЦИЈАЛНЕ БИОАКТИВНОСТИ ХИБИСКУСНЕ И ГАРСИНИЈСКЕ КИСЕЛИНЕ ПРОТИВ SARS-COV-2

WENDOLYNE LÓPEZ-OROZCO, LUIS HUMBERTO MENDOZA-HUIZAR, GIAAN ARTURO ÁLVAREZ-ROMERO и J. DE JESÚS MARTIN TORRES-VALENCIA

Área Académica de Química, Universidad Autónoma del Estado de Hidalgo, carretera Pachuca–Tulancingo, 42184, Mineral de la Reforma, Hidalgo, México

Рачунарско хемијска студија је проведена на дијастереоизомерима хибискусне (HA) и гарсинијске (GA) киселине, истражијући њихове способности доковања са главном протеазом (6LU7) од SARS-CoV-2. Мапирања електростатских потенцијала су открила да су негативна наелектрисања придружена карбоксилним и хидроксилним групама на положајима C-2 и C-3 и за хибискусну и за гарсинијку киселину. Међутим, присуство негативнијег потенциала око C-2 и C-3 код хибискусне киселине, у поређењу са гарсинијском киселином, сугерише да супституенти у (2*S*,3*R*) поседују јачи електрон-привлачни капацитет од оних у (2*S*,3*S*) конфигурацији. Студије молекулског докинга указују да се и хибискусна и гарсинијска киселина везују за главну протеазу путем каталитичког џепа. Ипак, симулације молекулскединамике откривају да само (HA) остаје везана за активно место током 100 ns са *RMSD* мањом од 1 Å, док (GA) дисосује из комплекса унутар почетних 16 ns. Ови налази расветљавају различито везивно понашање два једињења, са импликацијом потенцијалне терапијске интервенције против SARS-CoV-2. Ови налази бацају светло на различито везивно понашање два једињења, подржавајући импликације за потенцијалне терапијске интервенције против SARS-CoV-2.

(Примљено 28. априла, ревидирано 5. јуна, прихваћено 21. августа 2024)

REFERENCES

1. T. I. Ng, I. Correia, J. Seagal, D. A. Degoey, M. R. Schrimpf, D. J. Hardee, E. L. Noey, W. M. Kati, *Viruses* **14** (2022) 961 (http://dx.doi.org/10.3390/V14050961)
2. Y. L. Ng, C. K. Salim, J. J. H. Chu, *Pharmacol. Ther.* **228** (2021) 107930 (http://dx.doi.org/10.1016/J.PHARMTHERA.2021.107930)
3. C. L. Bellera, M. Llanos, M. E. Gantner, S. Rodriguez, L. Gavernet, M. Comini, A. Talevi, *Expert Opin. Drug Discov.* **16** (2021) 605 (http://dx.doi.org/10.1080/17460441.2021.1863943)

4. I. Aanouz, A. Belhassan, K. El-Khatabi, T. Lakhlifi, M. El-ldrissi, M. Bouachrine, *J. Biomol. Struct. Dyn.* **39** (2021) 2971 (http://dx.doi.org/10.1080/07391102.2020.1758790)
5. S. Yagi, A. Yagi, *Curr. Tradit. Med.* **9** (2023) 39 (http://dx.doi.org/10.2174/2215083809666230206114117)
6. A. Ghosh, S. Chakraborty, S. Majumder, M. Bhattacharya, *Lett. Appl. NanoBioScience* **12** (2023) 26 (http://dx.doi.org/10.33263/LIANBS124.108)
7. M. T. Quimque, K. I. Notarte, X. A. Adviento, M. H. Cabunoc, V. N. de Leon, F. S. L. delos Reyes, E. J. Lugtu, J. A. Manzano, S. N. Monton, J. E. Muñoz, K. D. Ong, D. Y. Pilapil, V. Roque, S. M. Tan, J. A. Lim, A. P. Macabeo, *Comb. Chem. High Throughput Screen.* **26** (2021) 459 (http://dx.doi.org/10.2174/1386207325666210917113207)
8. R. B. Malabadi, K. P. Kolkar, N. T. Meti, R. K. Chalannavar, *Int. J. Innov. Sci. Res. Rev.* **3** (2021) 1507 (https://journalijisr.com/sites/default/files/issues-pdf/IJISRR-600.pdf)
9. Y. T. M. Alharbi, W. M. Abdel-Mageed, O. A. Basudan, R. A. Mothana, M. Tabish Rehman, A. A. ElGamal, A. S. Alqahtani, O. I. Fantoukh, M. F. AlAjmi, *Saudi Pharm. J.* **32** (2024) 102023 (http://dx.doi.org/10.1016/J.JSPS.2024.102023)
10. M. Ariefin, R. R. Saputra, I. N. Pramesti, *AIP Conf. Proc.* **3055** (2024) 040001 (https://doi.org/10.1063/5.0193646)
11. S. T. Selvan, M. K. D. Jothinathan, *Cureus* **16** (2024) 1 (http://dx.doi.org/10.7759/CUREUS.57151)
12. M. A. Khanfar, M. I. Saleh, *Curr. Med. Chem.* **16** (2024) e57151 (http://dx.doi.org/10.2174/0109298673271674231109052709)
13. E. Akbaba, D. Karatas, *J. Inst. Sci. Tech.* **13** (2023) 872 (http://dx.doi.org/10.21597/jist.1187616)
14. S. Das, S. Satapathy, D. Acharya, S. Kumar Sahu, *Res. Sq.* **2023** (2023) 1 (http://dx.doi.org/10.21203/RS.3.RS-2837087/V1)
15. C. Parga-Lozano, *Duazary* **17** (2020) 1 (http://dx.doi.org/10.21676/2389783x.3597)
16. C. H. Parga-Lozano, *Biomed. J. Sci. Tech. Res.* **35** (2021) 28000 (http://dx.doi.org/10.26717/bjstr.2021.35.005761)
17. N. Balmeh, S. Mahmoudi, N. Mohammadi, A. Karabedianhajiabadi, *Informatics Med. Unlocked* **20** (2020) 100407 (http://dx.doi.org/10.1016/J.IMU.2020.100407)
18. S. Mahmoudi, N. Balmeh, N. Mohammadi, T. Sadeghian-Rizi, *Avicenna J. Med. Biotechnol.* **13** (2021) 107 (http://dx.doi.org/10.18502/AJMB.V13I3.6370)
19. N. Ohta, K. Inokuma, K. Miyabayashi, M. Miyake, I. Yagi, *Electrochemistry* **78** (2012) 132 (http://dx.doi.org/10.5796/electrochemistry.78.132)
20. N. F. Ramadhani, A. P. Nugraha, D. Rahmadhani, M. S. Puspitaningrum, Y. Rizqianti, V. D. Kharisma, T. N. E. B. T. A. Noor, R. D. Ridwan, D. S. Ernawati, A. P. Nugraha, *J. Pharm. Pharmacogn. Res.* **10** (2022) 418 (http://dx.doi.org/10.56499/jppres21.1316_10.3.418)
21. S. Guardiola, N. Mach, *Endocrinol. y Nutr.* **61** (2014) 274 (http://dx.doi.org/10.1016/j.endonu.2013.10.012)
22. E. Shawky, A. A. Nada, R. S. Ibrahim, *RSC Adv.* **10** (2020) 27961 (http://dx.doi.org/10.1039/d0ra05126h)
23. O. A. Olajide, V. U. Iwuanyanwu, I. Lepiarz-Raba, A. A. Al-Hindawi, M. A. Aderogba, H. L. Sharp, R. J. Nash, *Phyther. Res.* **35** (2021) 6963 (http://dx.doi.org/10.1002/ptr.7315)

24. H. Y. Aati, A. Ismail, M. E. Rateb, A. M. AboulMagd, H. M. Hassan, M. H. Hetta, *Plants* **11** (2022) 2521 (http://dx.doi.org/10.3390/PLANTS11192521)
25. A. J. Akindele, A. Sowemimo, F. O. Agunbiade, M. O. Sofidiya, O. Awodele, O. Ade-Ademilua, I. Orabueze, I. O. Ishola, C. I. Ayolabi, O. B. Salu, M. O. Akinleye, I. A. Oreagba, *Nat. Prod. Commun.* **17** (2022) 1 (https://doi.org/10.1177/1934578X221096968)
26. O. P. Abodunrin, O. F. Onifade, A. E. Adegboyega, *Informatics Med. Unlocked* **31** (2022) 100964 (http://dx.doi.org/10.1016/J.IMU.2022.100964)
27. D. Muralitharan, V. Varadharajan, B. Venkidasamy, *J. Mol. Recognit.* **36** (2023) e3055 (http://dx.doi.org/10.1002/JMR.3055)
28. N. S. Aini, V. D. Kharisma, M. H. Widyananda, A. A. A. Murtadlo, R. T. Probojati, D. D. R. Turista, M. B. Tamam, V. Jakhmola, E. Yuniarti, S. Al Aziz, M. R. Ghifari, M. T. Albari, R. S. Mandeli, M. A. Ghifari, D. Purnamasari, B. Oktavia, A. P. Lubis, F. Azra, F. Fitri, A. N. M. Ansori, M. Rebezov, R. Zainul, *Pharmacogn. J.* **14** (2022) 575 (http://dx.doi.org/10.5530/pj.2022.14.138)
29. A. N. M. Ansori, V. D. Kharisma, A. A. Parikesit, F. A. Dian, R. T. Probojati, M. Rebezov, P. Scherbakov, P. Burkov, G. Zhdanova, A. Mikhalev, Y. Antonius, M. R. F. Pratama, N. I. Sumantri, T. H. Sucipto, R. Zainul, *Pharmacogn. J.* **14** (2022) 85 (http://dx.doi.org/10.5530/pj.2022.14.12)
30. V. D. Kharisma, A. N. M. Ansori, Y. Antonius, I. Rosadi, A. A. A. Murtadlo, V. Jakhmola, M. Rebezov, N. Maksimiuk, E. Kolesnik, P. Burkov, M. Derkho, P. Scherbakov, M. E. Ullah, T. H. Sucipto, H. Purnobasuki, *J. Pharm. Pharmacogn. Res.* **11** (2023) 743 (http://dx.doi.org/10.56499/JPPRES23.1650_11.5.743)
31. O. A. Kolawole, T. G. Femi, O. E. Kolawole, O. O. Monisola, O. Temitope, A. B. Benjamin, A. S. Adewale, S. Banj, *Nat. Sci.* **18** (2020) 78 (http://dx.doi.org/10.7537/marsnsj180920.10)
32. A. Kalita, M. Das, B. Das, M. R. Baro, *Beni-Suef Univ. J. Basic Appl. Sci.* **11** (2022) 1 (http://dx.doi.org/10.1186/S43088-022-00214-2/FIGURES/10)
33. N. Khamthong, N. Hutadilok-Towatana, *Nat. Prod. Commun.* **12** (2017) 453 (http://dx.doi.org/10.1177/1934578x1701200337)
34. G. I. P. Pozos, M. A. Ruiz-López, J. F. Z. Nátera, C. Á. Moya, L. B. Ramírez, M. R. Silva, R. R. Macías, P. M. García-López, R. G. Cruz, E. S. Pérez, J. J. V. Radillo, *Appl. Sci.* **10** (2020) 560 (http://dx.doi.org/10.3390/app10020560)
35. P. M. Afladhanti, M. D. Romadhan, H. A. Hamzah, Q. Bhelqis, *Sriwij. J. Med.* **5** (2022) 31 (http://dx.doi.org/10.32539/SJM.V5I1.127)
36. A. N. M. Ansori, V. D. Kharisma, A. A. Parikesit, F. A. Dian, R. T. Probojati, M. Rebezov, P. Scherbakov, P. Burkov, G. Zhdanova, A. Mikhalev, Y. Antonius, M. R. F. Pratama, N. I. Sumantri, T. H. Sucipto, R. Zainul, *Pharmacogn. J.* **14** (2022) 85 (http://dx.doi.org/10.5530/PJ.2022.14.12)
37. D. Ganjewala, H. Bansal, R. Mittal, G. Srivastava, *Herb. Med. A Boon Heal. Hum. Life* (2022) 471 (http://dx.doi.org/10.1016/B978-0-323-90572-5.00012-3)
38. J. A. Izquierdo-Vega, D. A. Arteaga-Badillo, M. Sánchez-Gutiérrez, J. A. Morales-González, N. Vargas-Mendoza, C. A. Gómez-Aldapa, J. Castro-Rosas, L. Delgado-Olivares, E. Madrigal-Bujaidar, E. Madrigal-Santillán, *Biomedicines* **8** (2020) 100 (http://dx.doi.org/10.3390/BIOMEDICINES8050100)

39. R. A. El-Shiekh, U. R. Abdelmohsen, H. M. Ashour, R. M. Ashour, *Antibiotics* **9** (2020) 756 (http://dx.doi.org/10.3390/antibiotics9110756)
40. L. O. Chuah, W. Y. Ho, B. K. Beh, S. K. Yeap, *Evidence-Based Complement. Altern. Med.* **2013** (2013) 751658 (http://dx.doi.org/10.1155/2013/751658)
41. S. Kim, Y. Kim, J. W. Kim, Y. Hwang, S. H. Kim, Y. H. Jang, *J. Life Sci.* **32** (2022) 375 (https://doi.org/10.5352/JLS.2022.32.5.375)
42. Y. Takeda, Y. Okuyama, H. Nakano, Y. Yaoita, K. Machida, H. Ogawa, K. Imai, *Food Environ. Virol.* **12** (2020) 9 (http://dx.doi.org/10.1007/s12560-019-09408-x)
43. R. Krishnan, J. S. Binkley, R. Seeger, J. A. Pople, *J. Chem. Phys.* **72** (1980) 650 (http://dx.doi.org/10.1063/1.438955)
44. A. Grosdidier, V. Zoete, O. Michielin, *Nucleic Acids Res.* **39** (2011) W270 (http://dx.doi.org/10.1093/NAR/GKR366)
45. E. F. Pettersen, T. D. Goddard, C. C. Huang, G. S. Couch, D. M. Greenblatt, E. C. Meng, T. E. Ferrin, *J. Comput. Chem.* **25** (2004) 1605 (http://dx.doi.org/10.1002/jcc.20084)
46. Biovia Dassault Systèmes, *Discovery Studio Visualiser 2019*, Dassault Systèmes, San Diego, CA, 2020 (http://dx.doi.org/https://discover.3ds.com/discovery-studio-visualizer-download)
47. C. Kutzner, S. Páll, M. Fechner, A. Esztermann, B. L. De Groot, H. Grubmüller, *J. Comput. Chem.* **36** (2015) 1990 (http://dx.doi.org/10.1002/JCC.24030)
48. J. V. Vermaas, D. J. Hardy, J. E. Stone, E. Tajkhorshid, A. Kohlmeyer, *J. Chem. Inf. Model.* **56** (2016) 1112 (http://dx.doi.org/10.1021/acs.jcim.6b00103)
49. W. L. Jorgensen, D. S. Maxwell, J. Tirado-Rives, *J. Am. Chem. Soc.* **118** (1996) 11225 (http://dx.doi.org/10.1021/ja9621760)
50. W. L. Jorgensen, J. Chandrasekhar, J. D. Madura, R. W. Impey, M. L. Klein, *J. Chem. Phys.* **79** (1983) 926 (http://dx.doi.org/10.1063/1.445869)
51. G. Xiong, Z. Wu, J. Yi, L. Fu, Z. Yang, C. Hsieh, M. Yin, X. Zeng, C. Wu, A. Lu, X. Chen, T. Hou, D. Cao, *Nucleic Acids Res.* **49** (2021) W5 (http://dx.doi.org/10.1093/nar/gkab255)
52. C. A. Lipinski, *Drug Discov. Today Technol.* **1** (2004) 337 (http://dx.doi.org/10.1016/J.DDTEC.2004.11.007)
53. J. L. Dahlin, M. A. Walters, *Assay Drug Dev. Technol.* **14** (2016) 168 (http://dx.doi.org/10.1089/adt.2015.674)
54. J. J. Irwin, K. G. Tang, J. Young, C. Dandarchuluun, B. R. Wong, M. Khurelbaatar, Y. S. Moroz, J. Mayfield, R. A. Sayle, *J. Chem. Inf. Model.* **60** (2020) 6065 (http://dx.doi.org/10.1021/ACS.JCIM.0C00675)
55. M. Sargolzaei, *J. Mol. Graph. Model.* **103** (2021) 107803 (http://dx.doi.org/10.1016/j.jmgm.2020.107803)
56. M. A. Said, D. J. O. Khan, F. F. Al-Blewi, N. S. Al-Kaff, A. A. Ali, N. Rezki, M. R. Aouad, M. Hagar, *Vaccines* **9** (2021) 1012 (https://doi.org/10.3390/vaccines9091012)
57. A. Marques Da Fonseca, A. Luthierre, G. Cavalcante, R. Mateus, M. Carvalho, J. Falcão Do Amaral, R. P. Colares, E. S. Marinho, M. M. Neto, P. Colares, *Int. J. Res. - GRANTHAALAYAH* **8** (2020) 164 (http://dx.doi.org/10.29121/GRANTHAALAYAH.V8.I11.2020.2342)
58. P. Gale, *Microb. Risk Anal.* **21** (2022) 100198 (http://dx.doi.org/10.1016/j.mran.2021.100198)
59. M. Popovic, *Vaccines* **10** (2022) 2112 (http://dx.doi.org/10.3390/vaccines10122112)

60. M. Popovic, J. H. Martin, R. J. Head, *Heliyon* **9** (2023) e17174 (http://dx.doi.org/10.1016/j.heliyon.2023.e17174)
61. P. Gale, *Microb. Risk Anal.* **16** (2020) 100140 (http://dx.doi.org/10.1016/j.mran.2020.100140)
62. M. E. Popović, G. Šekularac, M. Popović, *Microb. Risk Anal.* **26** (2024) 100290 (http://dx.doi.org/10.1016/J.MRAN.2024.100290)
63. J. M. Casasnovas, T. A. Springer, *J. Biol. Chem.* **270** (1995) 13216 (http://dx.doi.org/10.1074/jbc.270.22.13216)
64. Z. Jin, X. Du, Y. Xu, Y. Deng, M. Liu, Y. Zhao, B. Zhang, X. Li, L. Zhang, C. Peng, Y. Duan, J. Yu, L. Wang, K. Yang, F. Liu, R. Jiang, X. Yang, T. You, X. Liu, X. Yang, F. Bai, H. Liu, X. Liu, L. W. Guddat, W. Xu, G. Xiao, C. Qin, Z. Shi, H. Jiang, Z. Rao, *Nature* **582** (2020) 289 (http://dx.doi.org/10.1038/S41586-020-2223-Y).

Journal of the Serbian Chemical Society
JSCS-info@shd.org.rs • www.shd.org.rs/JSCS
J. Serb. Chem. Soc. *90* (3) 305–310 (2025)
JSCS–5388
Short communication
Published 24 March, 2025

SHORT COMMUNICATION

A simple method for identification of native collagen by reversed-polarity electrophoresis: Short report

MARIO CHOPIN-DOROTEO[1], LUÍS MENDOZA[1,2], ENRIQUE LIMA[3] and EDGAR KRÖTZSCH[1]*

[1]*Laboratory of Connective Tissue, Centro Nacional de Investigación y Atención de Quemados, Instituto Nacional de Rehabilitación "Luis Guillermo Ibarra Ibarra", Mexico City, Mexico,* [2]*Facultad de Estudios Superiores Cuautitlán, State of Mexico, Mexico and* [3]*Instituto de Investigaciones en Materiales, Universidad Nacional Autónoma de México, Mexico City, Mexico*

(Received 5 July, revised 5 November, accepted 9 November 2024)

Abstract: The high molecular weight of collagen and the high uncommon amino acid composition (proline and hydroxyproline) make the protein particular at structural and physicochemical levels compared to others. Polyacrylamide gel electrophoresis (PAGE) is a simple and inexpensive method to identify collagen integrity; however, native forms of proteins generally show low quality bands. In this work, we considered the charge of the protein to perform a very simple method to identify the native form of type I collagen, exhibiting an appropriate electrophoretic resolution. First, we determined the collagen charge at different pHs and then modified a previously published method by changing the gel buffer and reversing the polarity of the electrophoresis chamber by turning the power cords; now the protein was moved from the anode to the cathode. The result was well-resolved protein bands that maintained their classical structure without degradation after PAGE, which were confirmed by extracting the protein from the native-PAGE and electrophoresing it in a sodium dodecyl sulphate-PAGE. This advantage could be useful when the electrophoresed native collagen is used by Western blotting for recognition with antibodies.

Keywords: extracellular matrix; native protein separation methods; polyacrylamide gel electrophoresis; protein electric charge.

INTRODUCTION

Collagen is a superfamily of proteins characterised by triple-α helical domains, where the most abundant member in vertebrates is type I. Type I collagen

* Corresponding author. E-mail: kroted@yahoo.com.mx
https://doi.org/10.2298/JSC240705092C

plays structural and informational roles in connective tissues, and its heterotrimeric structure $[\alpha_1(I)]_2,\alpha_2(I)]$, gives collagen its particular helical shape with the Gly-X-Y sequence (where X and Y are frequently proline and hydroxyproline, respectively).[1] Furthermore, the protein is considered to be among the fibril-forming colloid group of the superfamily,[2] therefore its physicochemical properties should be considered when handling it. The salting-out effect is evident for collagens; the high molecular weight of the protein and the electrostatic interactions between collagen fibres can be easily modified by neutralising the surface charge of the protein.[3,4] For example, NaCl can dissolve or precipitate neutral collagen solutions at concentrations less than or greater than 1 M/l, respectively,[3] where ionic strength and pH contribute to fibrillogenesis *in vitro*.[5] Among the different methods for the identification, semiquantification and separation of collagens, sodium dodecyl sulphate polyacrylamide gel electrophoresis (SDS-PAGE) is the most commonly used,[6] because it is easy and inexpensive to perform and the required device is regularly part of a laboratory of general biochemistry. However, the method is based on the ability of collagen to be negatively charged by SDS, which ultimately also denatures the protein.[7] So, when it is necessary to identify collagen under native conditions, a non-denaturing PAGE method is the choice. In this process, SDS is excluded and acidic conditions must be used.[8] Unfortunately, non-denaturing or native-PAGE shows some limitations due to the resolution of the collagen bands in the gel, contrary to the excellent images observed after SDS-PAGE. Unlike SDS-PAGE protocols, the use of native gel electrophoresis typically requires the optimisation of the separation conditions for specific samples (*i.e.*, collagens).[9] In this work, we introduce a simple method for performing native-PAGE to enhance the resolution of native collagen molecules by reversing the polarity of the electrophoretic chamber.

EXPERIMENTAL

We used type I pepsinized collagen (10 mg ml^{-1}), obtained from porcine sources (DSM Branch Pentapharm, Aesch, Switzerland) that was dialysed against 5 mM acetic acid to have a lower strength sample; collagen samples were diluted with 50 mM acetic acid. To measure the protein charge, 0.66 mg ml^{-1} collagen were evaluated in triplicates in a pH range of 3–7, with Nanotrac Wave equipment (Verder Scientific, Haan, Germany). Denaturing SDS-PAGE was conducted following the Laemmli method.[10] Briefly, 5.5 µg of heat-denatured collagen were loaded onto Mini Protean III Cell (Bio-Rad, Hercules, CA, USA) in a 0.75 mm thick discontinuous gel (4 % stacking gel, pH 6.8, and 6 % resolving gel, pH 8.8). The gel was stained with a 0.2 % Coomassie brilliant blue R-250 solution, 50 % methanol and 10 % glacial acetic acid for 2 h, and destained with a solution of 20 % methanol and 10 % glacial acetic acid for at least 4 h. Images of the bands were captured using the Gel Doc XR Gel Documentation System (Bio-Rad).

On the other hand, native-PAGE was performed according to the method described by Ramshaw JA and Werkmeister JA,[11] with some modifications. The collagen sample was dissolved in 0.1 M aqueous lactic acid containing 10 % sucrose. Samples were dissolved in 5 X

loading buffer (5 ml of 0.1 M lactic acid buffer with 10 ml of glycerol). Then, 8.3 μg of native or 1 h heat hydrolysed collagen samples were loaded into Mini Protean III Cell (Bio-Rad) in a 1.0 mm thick continuous gel, 3.2 %, pH 6.6. Before loading the samples, the gel was run for 30 min at 70 mA in 0.1 M lactic acid as cathode buffer and 50 mM Tris-HCl pH 6.6 as anode buffer. The loaded gel was run with running buffer (50 mM Tris-HCl pH 6.6) and reversed the chamber polarity for 6.5 h and 70 V in a cold room (3–4 °C). The gel was stained and destained as before. Finally, after staining, protein bands were excised and isolated from gel using 200 μl of elution buffer (50 mM Tris, pH 7.9, 0.1 mM EDTA, 0.15 M NaCl, 0.1 % SDS) for 24 h at 30 °C in a water bath. The eluate was concentrated five times using a CentriVap Concentrator (Labconco, Kansas City, MO, USA) and electrophoresed by SDS-PAGE.

RESULTS AND DISCUSSION

Native collagen evaluation by PAGE is much less frequent as a result of the particular physicochemical properties of the protein or the need for sophisticated devices. Our group has been working with native collagen and collagen copolymers,[12] so we face the need to evaluate collagen using a simple method such as PAGE. When attempting to replicate previously published methods, we encountered challenges, such as difficulty in reproduction, as a result of the lack of reagents or devices, and issues such as the resolution of bands in the published gel photographs.

In an attempt to adapt the Ramshaw JA and Werkmeister JA methods, by modifying the gel buffer, we observed the absence of collagen bands, leading us to suspect the involvement of the protein charge. Consequently, we conducted collagen charge determinations at different pHs. Our findings revealed a positive charge for the protein in the acidic range (Table I).

TABLE I. Relationship between pH and collagen charge; charge = average of triplicates, fC = femtocoulombs, *SD* = standard deviation

pH	Charge, fC	*SD*
3.06	+3.07	0.81
4.05	+3.22	0.89
4.95	+5.20	1.20
6.50	+5.71	0.41
7.12	+6.91	0.08

With this insight, we decided to reverse the polarity of the chamber by simply switching the power cords in the power supply. The result was a well-defined band of commercially purified type I collagen, as was also observed in the SDS-PAGE bands (Fig. 1a and b). The rationale for the polarity reversal was based on the positive charge of collagen, which facilitates protein migration from the anode (+) to the cathode (–) under acidic conditions (loading buffer, gel matrix and running buffer).

To demonstrate possible structural modifications in the protein as a result of the method, we recovered it from the native-PAGE gel and subjected it to extended

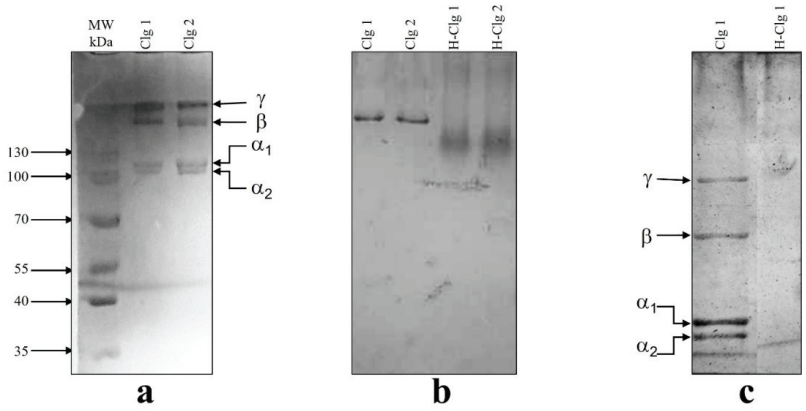

Fig. 1. Images of type I collagen subjected to PAGE. In (**a**), the electrophoretic pattern of collagen is observed under denaturing conditions (SDS-PAGE). The left lane is the molecular weight (MW) ladder in kDa, and the middle and right lanes (Clg 1 and Clg 2) show the pattern of denatured collagen samples. In (b), after the native-PAGE method described here, the first two lanes are single bands corresponding to native collagens (Clg 1 and Clg 2), and the third and fourth lanes exhibit the smear pattern corresponding to the heat-hydrolysed collagen samples (H-Clg 1 and H-Clg 2). Gel image (c) shows the SDS-PAGE of the collagen eluate bands (Clg 1), previously electrophoresed under native conditions. The left lane shows the typical pattern of denatured collagen, whereas the hydrolysed protein was absent in the right lane due to the small size of the protein fragments.

electrophoresis by SDS-PAGE. The goal was to highlight additional protein bands that might be in proximity to the main band, perhaps by degradation. The result revealed the typical electrophoretic pattern of type I collagen, where the α1 and α2 bands were evident, together with the β and γ bands (Fig. 1c). Despite the need to know the integrity of collagens, which has been a concern for researchers long time ago, the different works in which the protein was shown exhibited different issues. For example, in the work of Ramshaw and Werkmeister, 1988, the authors proposed a method for electrophoretic identification of native collagen, although their work only shows the electroblots, leaving out the possibility of knowing the electrophoretic pattern of the native proteins.[11] Furthermore, Ricard-Blum *et al*. published an electrophoretic method to assess various homo- or heterotrimeric collagens using a Phast System apparatus with a reversed polarity electrode assembly.[8] However, they never provided insight into the rationale behind reversing the polarity of the system, and their gel images exhibit blurriness with multiple small protein bands. Otherwise, with the method shown in this work, it was evident that the electrophoresed collagen was not degraded, which is important when the protein was Western blotted for recognition with antibodies. Also, with this approach, it becomes possible to analyse the extracted native collagen from the different tissues, in order to know the real proportion of the entire molecule, without the interference of the contamination of the α bands

present in the continuously turnover collagen. This strategy allows us to easily assess native collagen in cell-derived matrices,[13] to evaluate the real effect of biologically active enzymes from different sources on collagen[14] or to evaluate the collagenolytic enzymes involved in pathological conditions,[15] with the advantage that the analytical method would be focused on obtaining the effects on the real substrate, which can only be observed by native-PAGE, instead of the regular use of the typical denaturing SDS-PAGE. An additional advantage is that by this method, the protein in the native or denatured state could be easily semi-quantified by densitometry.

CONCLUSION

The method shown here was carried out taking advantage of the electrical properties of collagen under acidic conditions. Identification of native collagen by reversed-polarity electrophoresis is now a straightforward method that utilises common reagents and devices readily available to any laboratory conducting basic biochemical analyses.

Acknowledgements. The authors thank Salvador López-Morales, M.Sc., from the Instituto de Investigaciones en Materiales, Universidad Nacional Autónoma de México, Mexico City, Mexico, for technical assistance during the collagen charge assessment. Language revision was performed using Writefull AI.

ИЗВОД

ЈЕДНОСТАВНА МЕТОДА ЗА ИДЕНТИФИКАЦИЈУ НАТИВНОГ КОЛАГЕНА РЕВЕРСНОМ ЕЛЕКТРОФОРЕЗОМ: КРАТАК ИЗВЕШТАЈ

MARIO CHOPIN-DOROTEO[1], LUÍS MENDOZA[1,2], ENRIQUE LIMA[3] и EDGAR KRÖTZSCH[1]

[1]Laboratory of Connective Tissue, Centro Nacional de Investigación y Atención de Quemados, Instituto Nacional de Rehabilitación "Luis Guillermo Ibarra Ibarra", Mexico City, Mexico, [2]Facultad de Estudios Superiores Cuautitlán, State of Mexico, Mexico и [3]Instituto de Investigaciones en Materiales, Universidad Nacional Autónoma de México, Mexico City, Mexico

Висока молекулска маса и неуобичајени састав аминокиселина (пролин и хидроксипролин) чине колаген посебним међу протеинима у погледу структуре и физичко–хемијских својстава. Електрофореза у полиакриламидном гелу (PAGE) је једноставна и јефтина метода за идентификацију интегритета колагена, међутим, природни облици протеина генерално показују низак квалитет трака. У овом раду је узето у обзир наелектрисање протеина за извођење врло једноставне методе за идентификацију природног облика колагена типа I, који показује одговарајућу електрофоретску резолуцију. Прво је одређено наелектрисање колагена при различитим pH вредностима, а затим је претходно објављена метода модификована променом пуферског гела и променом поларитета коморе за електрофорезу окретањем каблова за напајање услед чега се протеин сада кретао од аноде ка катоди. На овај начин су добијене добро раздвојене протеинске траке које су задржале своју класичну структуру без деградације након PAGE, што је потврђено екстракцијом протеина из нативног PAGE и електрофорезом у натријум-додецил-сулфат–PAGE. Ова предност би могла бити корисна када се природни колаген, подвргнут електрофорези, користи у *Western blot* анализи за препознавање антителима.

(Примљено 5. јула, ревидирано 5. новембра, прихваћено 9. новембра 2024)

REFERENCES

1. S. Ricard-Blum, *Cold Spring Harb, Perspect. Biol*. **3** (2011) a004978 (https://doi.org/10.1101%2Fcshperspect.a004978)
2. M. Shenoy, N. S. Abdul, Z. Qamar, B. M. A. Bahri, K. Z. K. Al Ghalayini, A. Kakti, *Cureus* **14** (2022) e24856 (https://doi.org/10.7759/cureus.24856)
3. I. N. Amirrah, Y. Lokanathan, I. Zulkiflee, M. F. M. R. Wee, A. Motta, M. B. Fauzi, *Biomedicines* **10** (2022) 2307 (https://doi.org/10.3390/biomedicines10092307)
4. Z. Deyl, M. Adam, *J. Chrom*. *B: Biomed. Sci. App.* **488** (1989) 161 (https://doi.org/10.1016/s0378-4347(00)82945-x)
5. J. R. Harris, A. Soliakov, R. J Lewis, *Micron* **49** (2013) 60 (https://doi.org/10.1016/j.micron.2013.03.004)
6. B. J. Bielajew, J. C. Hu, K. A. Athanasiou, *Nat. Rev. Mater*. **5** (2020) 730 (https://doi.org/10.1038/s41578-020-0213-1)
7. A. B. Nowakowski, W. J Wobig, D. H. Petering, *Metallomics* **6** (2014) 1068 (https://doi.org/10.1039/c4mt00033a)
8. S. Ricard-Blum, D. J. Hartmann, G. Ville, *J. Chrom*. *B: Biomed. Sci. App.* **530** (1990) 432 (https://doi.org/10.1016/s0378-4347(00)82346-4)
9. C. Arndt, S. Koristka, A. Feldmann, M. Bachmann, in: *Electrophoretic Separation of Proteins. Methods in Molecular Biology*, B. Kurien, R. Scofield, Eds., Humana Press, New York, 2019 (https://doi.org/10.1007/978-1-4939-8793-1_8)
10. U. K. Laemmli, *Nature* **227** (1970) 680 (https://doi.org/10.1038/227680a0)
11. J. A. Ramshaw, J. A Werkmeister, *Anal. Biochem*. **168** (1988) 82 (https://doi.org/10.1016/0003-2697(88)90013-9)
12. G. Leyva-Gómez, E. Lima, G. Krötzsch, R. Pacheco-Marín R. N. Rodríguez-Fuentes, D. Quintanar-Guerrero, E. Krötzsch, *J. Phys. Chem., B* **118** (2014) 9272 (https://doi.org/10.1021/jp502476x).
13. D. Shendi, J. Marzi, W. Linthicum, AJ. Rickards, DM. Dolivo, S. Keller, MA. Kauss, Q. Wen, TC. McDevitt, T. Dominko, K. Schenke-Layland, MW. Rolle. *Acta Biomater.* **100** (2019) 292 (https://doi.org/10.1016/j.actbio.2019.09.042).
14. L. Kumar, W. Colomb, J. Czerski, CR. Cox, SK. Sarkar. *Protein Expr Purif.* **148** (2018) 59 (https://doi.org/10.1016/j.pep.2018.04.001).
15. W. Kafienah, DJ. Buttle, D. Burnett, AP. Hollander. *Biochem J*. **330** (Pt 2) (1998) 897 (https://doi.org/10.1042/bj3300897).

Journal of the Serbian Chemical Society
JSCS@tmf.bg.ac.rs • www.shd.org.rs/JSCS
J. Serb. Chem. Soc. *90* (3) 311–324 (2025)
JSCS–5389
Original scientific paper
Published 24 March, 2025

Application of magnetite nanoparticle-modified walnut shell as an adsorbent for the removal of the organic dye Coomassie Brilliant Blue R-250

MOZHGAN BIUKI, HASSAN ZAVVAR MOUSAVI*, MAJID ARVAND and HADI FALLAH MOAFI

Faculty of Chemistry, Department of Analytical Chemistry, University of Guilan, Rasht, Iran

(Received 21 April, revised 10 October, accepted 17 November 2024)

Abstract: In this research, a magnetic nanocomposite, walnut shell@Fe_3O_4, was synthesized as a natural adsorbent for the removal of Coomassie Brilliant Blue (CBB) R-250 organic dye from aqueous solutions, achieving a remarkable removal efficiency of 96.16 %. The morphology of the nanocomposite was characterized using SEM and FTIR, revealing particle sizes of less than 18 nm. Additionally, BET analysis was performed, indicating a high surface area that enhances adsorption capacity. The influential variables affecting dye removal, including solution pH, stirring time, adsorbent dosage, initial dye concentration, temperature and ionic strength, were optimized. The adsorption process was analysed using Langmuir, Freundlich, Temkin and Dubinin–Radushkevich isotherm models. The experimental results indicated that the process followed the Freundlich and Temkin isotherm models, suggesting the heterogeneous nature of the adsorbent surface. The kinetic conditions of adsorption were investigated using pseudo-first order and pseudo-second-order models, with results showing that the adsorption process of CBB followed the pseudo-second-order kinetic model, indicating the chemical adsorption of the dye onto the magnetic nanoparticles. The thermodynamic studies also revealed the spontaneous nature of the adsorption process, with a positive slope of the Van't Hoff curve indicating an exothermic reaction. Due to the equilibrium time of 5 min in the adsorption mechanism, the synthesized magnetic nanocomposite demonstrated a high CBB dye removal rate, making it suitable for treating dye-containing solutions.

Keywords: adsorption; thermodynamic; kinetic; magnetic nanocomposite; isotherm.

INTRODUCTION

Nowadays, water pollution has become one of the major issues. Various pollutants, including heavy metals, dyes, radioactive compounds and organic and

* Corresponding author. E-mail: hzmousavi@guilan.ac.ir
https://doi.org/10.2298/JSC240421095B

inorganic substances, contribute to water pollution.[1] Dyes, due to their wide applications in various industries, can be considered major pollutants in industrial effluents. They can lead to reduced photosynthetic activity in aquatic plants due to decreased light penetration in polluted waters,[2] increased biochemical oxygen demand, the generation of unpleasant odours, and the release of toxic substances.[3] Wastewater containing dyes is challenging to treat, as dyes are highly resistant to digestion and stable against oxidizing agents. Today, experts have realized that surface adsorption using cost-effective adsorbents is a good and economical method for wastewater treatment from dye compounds.[4] The surface adsorption using metallic nanoparticles has emerged as an environmentally friendly technology in recent years and has been investigated as an effective means for eliminating biological pollution in wastewater.[5] Multiple studies have been conducted in the field of removing Coomassie Brilliant Blue R-250 dye, including the use of raw oyster shell for the removal of Coomassie Brilliant Blue R-250 dye from aqueous solutions.[6] Poly(phenylene diamine)-grafted electrospun carbon nanofibers were effectively used for the adsorption of CBB dye.[7] starch/poly(alginic acid-cl-acrylamide) nanohydrogels demonstrated significant efficiency in removing Coomassie Brilliant Blue R-250.[8] Alginate–chitosan nanoparticles showed high adsorption capabilities for CBB.[9] The synthesis of a hybrid structured magnetite crosslinked polyionic liquid was explored for the efficient Coomassie Brilliant Blue R-250 dye removal,[10] as well as the modification of magnetite nanoparticles' surfaces with multifunctional ionic liquids for the Coomassie Brilliant Blue R-250 dye removal.[11] α-Chitin nanoparticles were used for the adsorption of Coomassie Brilliant Blue R-250 dye.[12] Response surface methodology was applied for the removal of Coomassie blue dye, using natural and acid-treated clays.[13] Well-crystalline ZnO nanostructures were investigated for the removal of hazardous dyes, including CBB.[14] Decolorization of Coomassie Brilliant Blue R-250 by dextran aldehyde-modified horseradish peroxidase.[15] adsorption of Coomassie Brilliant Blue R-250 dye onto novel activated carbon prepared from *Nigella sativa* L.[16] Magnetic nanoparticles refer to particles with an independent nature and maximum dimensions of around 100 nm that possess magnetic elements.[17] Among the magnetic nanoparticles, iron-based nanoparticles, especially superparamagnetic Fe_3O_4 nanoparticles (magnetite), have received the most attention due to their abundance, low cost, non-toxicity, rapid response, good biocompatibility, the lack of residual magnetism after removal of the external magnetic field and high efficiency in adsorbing pollutants from contaminated water.[18]

The study aims to synthesize a magnetic nanocomposite using walnut shell and evaluate its effectiveness in removing CBB organic dye from water. The walnut shell is chosen as the adsorbent due to its abundant availability, low cost, and high adsorption capacity. Interestingly, no previous research has explored the

use of magnetic nanocomposites derived from walnut shell for CBB dye removal in aqueous solutions.

EXPERIMENTAL

Materials and methods

Iron (III) chloride hexahydrate ($FeCl_3 \cdot 6H_2O$, 99.9 %), Iron (II) chloride tetrahydrate ($FeCl_2 \cdot 4H_2O$, 99.9 %), ammonium hydroxide (NH_4OH, 25 %), hydrochloric acid (HCl, 37 %), sodium hydroxide (NaOH, 99 %), acetic acid (CH_3COOH, 100 %), nitric acid (HNO_3, 65 %) and sulfuric acid (H_2SO_4, 98 %) were all obtained from Merck and used in the experiment. The walnut shells were collected from mountainous areas near Rudbar; distilled water was used; Coomassie Brilliant Blue R-250 dye ($C_{45}H_{44}N_3NaO_7S_2$) was employed. Silica gel with a mesh size of 60 (equivalent to a pore diameter of 0.0098 in), a magnetic iron remover with a strength of 1.4 T, a dual-beam UV–Vis spectrophotometer (JONIOR model 35, Perkin–Elmer, USA), a pH meter (MTT65 model), mechanical and magnetic stirrers (TM52E model, Fan Azin Gostar, Iran), a digital scale with a precision of 0.0001 g (AS220.R2 model, Radwag, Poland), an oven (Memmert, Germany), a centrifuge (D-7200 model, Hettich Universal, Germany), a scanning electron microscope (SEM, MIRA3 model, Tescan, Czech Republic), a Fourier-transform infrared spectroscopy (FT-IR) instrument (Vertex70 model, Bruker, Germany) and a Brunauer–Emmett–Teller (BET) surface area analyzer (Autosorb iQ, Quantachrome Instruments) were used in this study. Additionally, the laboratory equipment such as porcelain mortars and glassware like beakers, test tubes, and vials were used. The specifications of CBB organic dye are presented in Table I.

Table I. Characteristics of CBB R-250 Organic Dye

Chemical structure	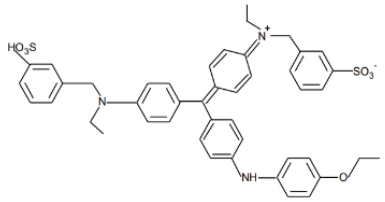
Dye type	Anionic
Chemical formula	$C_{45}H_{44}N_3NaO_7S_2$
Molecular weight, g mol^{-1}	825.97
Maximum absorption wavelength, nm	555

Preparation of walnut shell

First, the walnut shells were dried after being collected by exposing them to direct sunlight. The walnut shells were initially washed with water and then rinsed with distilled water. They were then placed in an oven at a temperature of 60 °C for 24 h to ensure complete drying. Once dried, the shells were placed in a mortar and ground into fine particles. Subsequently, these particles were washed multiple times with distilled water until they lost their original colour. Next, 0.5 g of the desired adsorbent were mixed with 0.5 M solutions of nitric acid, sulfuric acid, hydrochloric acid, acetic acid and sodium hydroxide. The mixture was stirred on a magnetic stirrer at a speed of 400 rpm for 24 h. The mixture was then filtered, and any excess acid or base was removed by washing with distilled water multiple times. The adsorbent was

dried in an oven at 60 °C (overnight). The particles were then passed through a 60--mesh sieve to obtain uniform particles with a diameter less than 250 μm. To modify the surface of these particles and impart magnetic properties for the ease of separation, magnetite nanoparticles were used through a chemical deposition method.[19]

Synthesis of walnut shell magnetic nanocomposite

The magnetic nanocomposite of walnut shell was synthesized using a co-precipitation method with iron (III) and iron (II) chlorides at a mole ratio of 2:1.[20] According to this method, 4.24 g of $FeCl_3 \cdot 6H_2O$ and 1.55 g of $FeCl_2 \cdot 4H_2O$ were dissolved in 100 mL of deionized water inside a flask. The resulting solution was placed under a nitrogen atmosphere for 20 min to remove dissolved oxygen and prevent oxidation. To obtain a homogeneous solution, the mixture was mechanically stirred using a magnetic stirrer. Next, the solution was heated to 80 °C, and then 25 % ammonium hydroxide was added dropwise over a period of 30 min to raise the pH of the solution to 11. Subsequently, 10 g of prepared walnut shell, obtained in the previous step, were added to the suspension mixture. The reaction continued for 30 min with vigorous stirring. Finally, the magnetic composite was separated using a magnet and washed multiple times with distilled water through repeated distillation. In the final step, the magnetic composite was placed in an oven at 70 °C for 4 h to dry. The synthesized adsorbent was then ready for use in subsequent stages.[19]

RESULTS AND DISCUSSION

The morphology of walnut shell@Fe_3O_4 nanocomposite was investigated using scanning electron microscopy (SEM)

The morphology and particle size of the walnut shell@Fe_3O_4 nanocomposite were thoroughly analysed using a scanning electron microscope (SEM). Fig. 1a presents the SEM image of the walnut shell prior to the deposition of magnetite nanoparticles, illustrating the natural structure and texture of the shells. In contrast, Fig. 1b displays the SEM image after the deposition of magnetite nanoparticles, revealing significant changes in morphology. The SEM images indicate a satisfactory size distribution of the magnetite particles, which are uniformly distributed across the walnut shell surface. The analysis shows that the average size of the magnetite particles is below 18 nm, suggesting the successful synthesis of nanoparticles with desirable dimensions for effective adsorption applications. The presence of numerous globules can be observed, indicating a high degree of aggregation and interaction among the magnetite nanoparticles.[21] This fine particle size is advantageous as it enhances the surface area available for adsorption processes, thereby improving the efficacy of the walnut shell @Fe_3O_4 nanocomposite in removing contaminants from aqueous solutions. Overall, the SEM characterization confirms that the walnut shell@Fe_3O_4 nanocomposite has been effectively synthesized with the appropriate morphological properties for its intended applications.

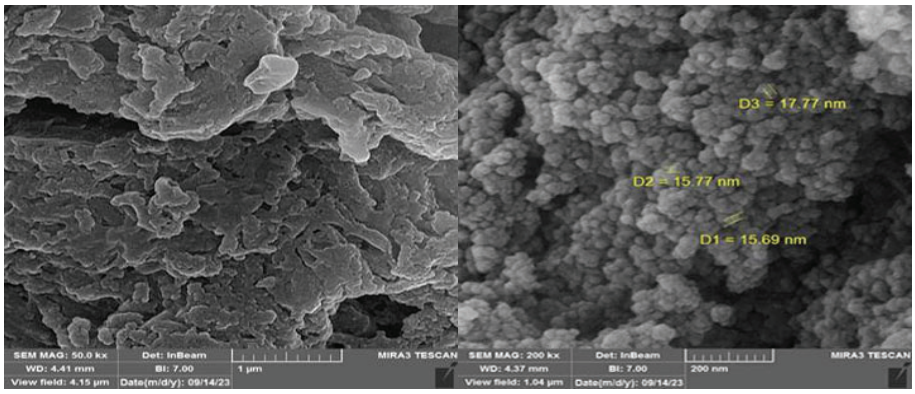

(a) (b)

Fig. 1. SEM images of the walnut shell surface: a) before and b) after magnetite nanoparticle deposition.

BET analysis

To determine the adsorbent's surface area, pore volume and particle diameter, a BET analysis was conducted on 0.3545 g of walnut shell@Fe_3O_4 at a temperature of 77 K using nitrogen gas. The specific surface area of the adsorbent was determined to be 12.311 $m^2\ g^{-1}$, indicating a significantly higher potential for pollutant adsorption compared to many conventional adsorbents. A larger surface area plays a crucial role in adsorption capacity, depending on the type of pollutant. The results are presented in Table II.

TABLE II. Physical properties of walnut shell@Fe_3O_4

Parameter	Surface area, $m^2\ g^{-1}$	Pore volume, $cm^3\ g^{-1}$	Average pore diameter, nm
Value	12.311	0.055	17.918

The pore volume was measured at 0.055 $cm^3\ g^{-1}$, and the average pore diameter was found to be 17.9 nm. This diameter exceeds that of many common pollutants, making it easier for the pollutant molecules to enter the adsorbent's mesostructure. The examination revealed that the material exhibits mesoporous attributes, consistent with IUPAC criteria.[22] The combination of a high specific surface area, appropriate pore volume, and suitable pore diameter makes this adsorbent a promising option for environmental applications. Additionally, the surface of lignocellulose-based adsorbents like walnut shell is rich in various functional groups, enhancing the overall adsorption capacity for charged dye molecules.

Identification of the nanostructure of walnut shell@Fe_3O_4 using Fourier transform infrared (FTIR) spectroscopy

For a more detailed study of the nanostructure of the synthesized magnetic walnut shell nanoparticles, Fourier transform infrared (FTIR) spectroscopy was

utilized. The FTIR spectrum of the synthesized nanoparticles is presented in Fig. 2. In this spectrum, the absorption band at 580 cm^{-1} corresponds to the stretching vibration of the Fe–O bond. The absorption bands at 655 and 995 cm^{-1} are attributed to the bending vibrations of the C–H bonds. The absorption band at 1380 cm^{-1} represents the bending vibrations of the CH_2 group, while the absorption band at 1718 cm^{-1} corresponds to the C=O bond and the absorption band at 3155 cm^{-1} represents the stretching vibration of the O–H bond.[19] Based on the infrared spectrum, it can be concluded that the magnetic nanocomposite of walnut shell has been successfully synthesized.

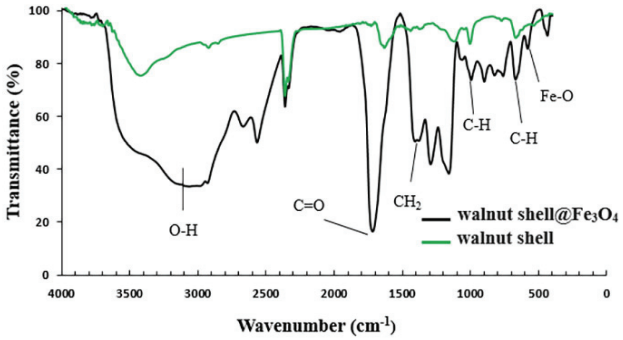

Fig. 2. FT-IR spectrum of walnut shell before and after nano-magnetite.

The point of zero charge (pH_{PZC}) of the walnut shell@Fe_3O_4 nanostructure

The point of zero charge (pH_{PZC}) refers to the pH at which the net surface charge of an adsorbent becomes zero. Determining this point is important for characterizing the surface properties of the adsorbent. Above the pH_{PZC}, the surface of the adsorbent becomes negatively charged, making it easier to adsorb ions with opposite charges (positively charged ions). Similarly, below the pH_{PZC}, the surface charge of the adsorbent becomes positive, leading to faster adsorption of negatively charged ions.[11] In this study, the effect of pH on the magnetic walnut shell nanocomposite was investigated. The solutions with different pH values ranging from 2 to 12 were prepared using sodium hydroxide and hydrochloric acid. The magnetic nanocomposites were added to each solution and stirred for 24 h. After centrifugation, the final pH of each solution was measured.[23] By plotting Fig. 3, the final pH against the initial pH, pH_{PZC} of the nanocomposite was determined to be 6.

Adsorption experiments

The desired solutions were prepared using a dilution process from a stock solution, after which the adsorption experiments were conducted to investigate the effects of pH, contact time, adsorbent amount, initial dye concentration, temperature and ionic strength on the adsorption of CBB by the magnetic walnut

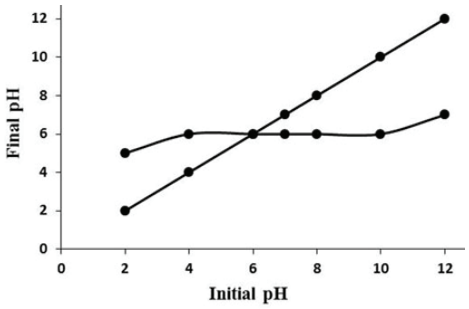

Fig. 3. Zero point of charge diagram.

shell nanocomposite. Solutions of CBB were prepared in 25 mL volumes, changing one of the factors influencing adsorption while keeping the other parameters constant to determine the optimal values. After preparing the solutions, each was stirred with a magnet and a magnetic stirrer at a constant speed (400 rpm). They were then separated using a centrifuge, and their adsorption was measured using a spectrophotometer at a maximum wavelength of 555 nm. The percentage removal and the amount of unabsorbed dye on the nanoparticles were calculated according to the details given in Supplementary material to this paper.

Effect of pH. The pH of the solution affects the adsorption of CBB dye on the adsorbent surface. It changes the surface charge and influences the ionization state of the dye.[24] This affects the kinetics and equilibrium properties of the adsorption process. At an acidic pH, H^+ adsorbs on the nanocomposite surface, giving the active groups a partial positive charge and making them more prone to binding the anionic dye, CBB. In this study, CBB dye solutions with a concentration of 50 mg L^{-1} were prepared at different pH values (2–12). The adsorption process was carried out by mixing the solutions with the adsorbent for 30 min and then measuring the adsorption using a spectrophotometer after centrifugation. The results showed that the adsorption percentage increased as the pH decreased. At lower pH values, the adsorbent surface acquired a positive charge, enhancing the interaction with the negatively charged dye molecules. In fact, at higher pH values, the adsorption was less effective due to the presence of negative ions on the adsorbent surface.[25] pH 4 was identified as the optimal pH for further experiments (Fig. 4a).

Effect of contact time. The another significant factor influencing the adsorption process is contact time. For example, in a study, the most effective adsorbent was identified as the one that achieved the highest removal percentage in the shortest time.[26] In this study, the effect of contact time on the adsorption of CBB dye, using a magnetic nanocomposite was examined. Solutions of CBB dye with a concentration of 50 mg L^{-1} were prepared at the optimal pH, and the adsorbent was added and stirred for different contact times. The results showed that the percentage of CBB removal increased with the contact time. However, after

approximately 5 min, the removal percentage reached equilibrium, indicating minimal changes thereafter. This suggests that 5 min was identified as the optimal contact time for further investigations (Fig. 4b).

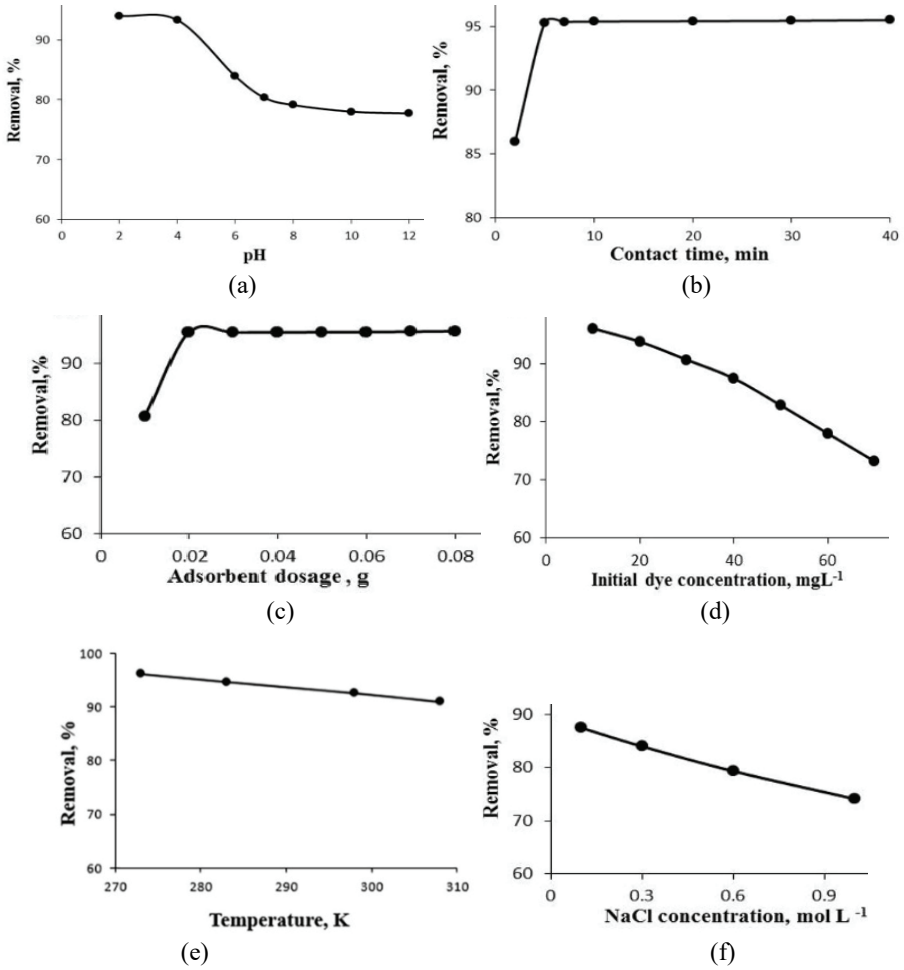

Fig. 4. Effect of different: a) pH, b) contact time, c) absorbent amount, d) initial dye concentration, e) temperature and f) ion strength, on the adsorption of CBB by walnut shell magnetic nanocomposite.

Effect of adsorbent dosage. In this study, the effect of adsorbent dosage on the adsorption process was investigated. Solutions of CBB dye with a concentration of 50 mg L^{-1} at the optimal pH were prepared, and different amounts of the magnetic nanocomposite adsorbent were added to each solution. The results showed that increasing the adsorbent dosage led to higher percentages of CBB dye removal. This can be attributed to the increased surface area and available binding sites

provided by the higher adsorbent dosage.[27] The highest removal percentage was observed at an adsorbent dosage of 0.02 g, beyond which further increases in dosage had minimal impact. Therefore, an optimal adsorbent dosage of 0.02 g was determined for the magnetic nanocomposite (Fig. 4c).

Effect of initial dye concentration. The study investigated the impact of the initial concentration of CBB dye on the adsorption process. Solutions with varying concentrations (10–70 mg L^{-1}) were prepared under optimal conditions. After stirring and filtration, the adsorption data were analysed. The results showed that as the initial dye concentration increased, the percentage of CBB removal gradually decreased. This is because higher concentrations lead to more competition for the available adsorption sites on the adsorbent.[28] Therefore, the optimal initial concentration for CBB dye adsorption was determined to be 10 mg L^{-1} (Fig. 4d).

Effect of temperature. The study examined the effect of temperature on the adsorption of CBB dye by a magnetic nanocomposite. Solutions with a volume of 25 mL and an initial concentration of 10 mg L^{-1} of CBB dye were prepared under optimal pH conditions. The adsorption process was conducted at temperatures ranging from 273 to 308 K with a stirring time of 5 min. The results revealed that as the temperature increased, the percentage of CBB removal by the adsorbent decreased. This indicates an exothermic adsorption process,[29] where higher temperatures reduce the adsorption capacity of the magnetic nanocomposite for CBB dye (Fig. 4e).

Effect of ionic strength. The study investigated the effect of ionic strength on the adsorption of CBB dye by a magnetic nanocomposite. Sodium chloride solutions with concentrations ranging from 0.1 to 1 M were prepared. The results showed that as the salt concentration increased, the removal efficiency of CBB dye by the nanocomposite decreased. The described decrease in efficiency can be attributed to the formation of a protective layer on the surface of the adsorbent, which hinders the electrostatic interaction between the adsorbent and the dye molecules. The optimal condition for the experiment was determined to be zero ionic strength, without increasing the salt concentration (Fig. 4f).[30]

Equilibrium adsorption isotherms

The study aimed to analyse the adsorption data using different adsorption isotherms, namely Langmuir, Freundlich, Temkin and Dubinin–Radushkevich isotherms (for details, see Supplementary material). These isotherms help in understanding the interaction mechanism between the adsorbate species and the adsorbent material.[31,32]

Based on the results presented in Table III and the correlation coefficients (R^2) obtained for the different models, it can be concluded that the adsorption data in this study for the walnut shell magnetic nanocomposite follows the Freundlich and Temkin isotherms. This suggests that the adsorption process occurs heterogene-

ously and involves multiple layers. The maximum monolayer surface adsorption capacity of the magnetic nanocomposite, as determined from the Langmuir isotherm, is observed to be 212.76 mg g^{-1}. Moreover, the equilibrium parameter value (R_L) ranging from 0 to 1 and the intensity of adsorption (n) ranging from 1 to 10 indicate favourable adsorption using this adsorbent.[33]

TABLE III. The values of constants and correlation coefficients related to Langmuir, Freundlich, Temkin and Dubinin–Radushkevich equilibrium adsorption isotherms for the adsorption of CBB

Langmuir	Freundlich	Temkin	Dubinin-Radushkevich
$R^2 = 0.9505$	$R^2 = 0.9907$	$R^2 = 0.9917$	$R^2 = 0.9342$
$q_m = 212.76$	$n = 1.23$	$B_T = 33.48$	$q_m = 65.72$
$b = 0.037$	$k_F = 8.94$	$A_T = 0.57$	$\beta = 2.52$
$R_L = 0.34$			

Adsorption kinetics

To gain a better understanding of the surface adsorption process, it is important to study the kinetics of the adsorption. The kinetics of adsorption provide insights into the efficiency of the adsorption process and the stages involved, such as film diffusion, intraparticle diffusion, surface diffusion or a combination of these stages. In this study, two kinetic models were employed to determine the better fit: the pseudo-first-order Lagergren model and the pseudo-second-order Ho model (for details, see Supplementary material). By plotting the graph of t/q_t against t and analyzing the slope and intercept (Fig. S-2 of the Supplementary material), the adsorption capacity at equilibrium (q_{e2}) and the pseudo-second-order rate constant (k_2) can be calculated.[34,35] The kinetic parameters obtained from these models are presented in Table IV.

TABLE IV. Pseudo-first order and pseudo-second order kinetic parameters by walnut shell magnetic nanocomposite

Pseudo-first-order model			Pseudo-second-order model		
K_1 / min^{-1}	q_e / mg g^{-1}	R^2	K_2 / g mg^{-1} min^{-1}	q_{e2} / mg g^{-1}	R^2
0.099	55.28	0.9763	0.13	60.24	0.9999

Based on the coefficient of determination (R^2) obtained, if the pseudo-second-order kinetic model has a higher R^2 value, compared to the pseudo-first-order kinetic model, it can be concluded that the adsorption process in this study follows pseudo-second-order kinetics. Furthermore, the nature of adsorption is considered to be chemical in nature.[36]

Adsorption thermodynamics

In this study, the changes in adsorption capacity with the respect to temperature were examined to determine the nature of the adsorption process (exo-

thermic or endothermic). The optimal temperature for the maximum adsorption and desorption was identified. The adsorption constants and equilibrium constants were calculated based on the slope of the curves. Lower temperatures were found to be more economically favourable for the adsorption process. Thermodynamically, a negative change in Gibbs energy ($\Delta G°$) indicates spontaneous adsorption. A negative standard enthalpy change ($\Delta H°$) suggests an exothermic adsorption process. Changes in standard entropy ($\Delta S°$) indicate changes in system entropy.[37] The details are given in the Supplementary material.

By plotting ln K_c against $1/T$ (Fig. S-3 of the Supplementary material) and determining the slope and intercept from the origin of the resulting curve, the variables $\Delta H°$ and $\Delta S°$ can be obtained.[38,39] The results are presented in Table V.

TABLE V. Thermodynamic parameters of the adsorption process of CBB dye by magnetic nanocomposite at different temperatures

T / K	K_c / mg L^{-1}	$\Delta G°$/ KJ mol^{-1}	$\Delta H°$/ KJ mol^{-1}	$\Delta S°$ / kJ mol^{-1} K^{-1}	R^2
273	5.26	–3.77	–24.42	–0.075	0.9991
283	3.47	–2.92			
298	2.13	–1.87			
308	1.52	–1.08			

According to Table V, $\Delta G°$ for the dye CBB in this study are negative. Therefore, it can be concluded that the adsorption process by the magnetic walnut shell nanocomposite occurs spontaneously. The negative value of $\Delta H°$ indicates that the adsorption process is exothermic and serves as a favourable factor in this process. The negative value of $\Delta S°$ indicates a decrease in disorder within the system, suggesting that at higher temperatures, the adsorbent will have reduced adsorption capacity.[40]

Comparison study

In Table VI, a detailed comparison of the maximum adsorption capacity of various adsorbents for the removal of CBB dye is presented. According to Table VI, it can be concluded that the magnetic walnut shell nanocomposite (walnut

TABLE VI. Comparison of proposed adsorbent with some adsorbents used for CBB removal

Adsorbent	q_{max} / mg g^{-1}	Reference
Natural agalmatolite	11.29	[13]
Natural kaolinite	22.89	[13]
Starch/poly(alginic acid-cl-acrylamide) nanohydrogel	31.24	[8]
p-ECNFs	141.00	[7]
o-ECNFs	107.80	[7]
m-ECNFs	46.90	[7]
Activated carbon (Nigella sativa L)	14.49	[16]
α-Chitin nanoparticles	8.55	[12]
Walnut shell@Fe_3O_4	212.76	This study

shell@Fe_3O_4) has achieved a suitable maximum adsorption capacity compared to other adsorbents, indicating that this adsorbent is effective for the removal of CBB from aqueous solutions.

CONCLUSION

In this study, a simple and effective method was used in this study to remove CBB dye from water using walnut shell modified with magnetic nanoparticles. The walnut shell was chemically coated with magnetite nanoparticles, creating a magnetic walnut shell nanocomposite. The results showed that this modified adsorbent has great potential for CBB dye removal. The removal percentage decreased with increasing dye concentration and decreasing adsorbent dosage. Isotherm studies confirmed multilayer adsorption on the adsorbent's heterogeneous surfaces, with a maximum adsorption capacity of 212.76 mg g^{-1} at the optimal dye concentration. The kinetic studies indicated chemical adsorption on the adsorbent's surface. The thermodynamic investigations revealed that the adsorption process was spontaneous, and the Van't Hoff curve showed an exothermic nature of the dye adsorption on the synthesized adsorbent.

SUPPLEMENTARY MATERIAL

Additional data and information are available electronically at the pages of journal website: https://www.shd-pub.org.rs/index.php/JSCS/article/view/12900, or from the corresponding author on request.

Acknowledgement. All authors would like to thank the Faculty of Chemistry, Department of Analytical Chemistry, University of Guilan, for their support in this research.

ИЗВОД

ПРИМЕНА МОДИФИКОВАНЕ ЉУСКЕ ОРАХА НАНОЧЕСТИЦАМА МАГНЕТИТА КАО АДСОРБЕНСА ЗА УКЛАЊАЊЕ ОРГАНСКЕ БОЈЕ COOMASSIE BRILLIANT BLUE R-250

MOZHGAN BIUKI, HASSAN ZAVVAR MOUSAVI, MAJID ARVAND и HADI FALLAH MOAFI

Faculty of Chemistry, Department of Analytical Chemistry, University of Guilan, Rasht, Iran

Магнетни нанокомпозит, љуска ораха@Fe_3O_4, синтетисан је као природни адсорбенс за уклањање органске боје Coomassie Brilliant Blue (CBB) R-250 из водених раствора, са ефикасношћу од 96,16 %. Морфологија нанокомпозита је окарактерисана коришћењем SEM и FTIR, при чему је утврђена величине честица мања од 18 nm. Додатно, извршена је BET анализа која указује на велику површину која повећава капацитет адсорпције. Оптимизоване су варијабле које утичу на уклањање боје, и то: pH раствора време мешања, количина адсорбенса, почетна концентрација боје, температура и јонска сила. Проценс адсорпције је анализиран применом Langmuir, Freundlich, Temkin и Dubinin–Radushkevich модела изотерми. Експериментални резултати су показали да процес адсорпције прати Freundlich и Temkin изотермне моделе што указује на хетерогену природу површине адсорбенса. Применом модела псеудо-првог и псеудо-другог реда су испитивани кинетички услови адсорпције. Резултати су показали да процес адсорпције CBB прати кинетички модел псеудо-другог реда што указује на хемијску адсорпцију боје на наночестицама. Термодинамичким студијама је утврђена спонтана природа процеса адсорпције, са позитивним нагибом Вант Хофове криве што указује на егзотермну реакцију. Због

кратког времена успостављања равнотеже од 5 min, синтетисани магнетни нанокомпозит је показао велику брзину уклањања CBB боје, што га чини погодним за третман раствора који садрже боје.

(Примљено 21. априла, ревидирано 10. октобра, прихваћено 17. новембра 2024)

REFERENCES

1. R. Zein, H. Fathony, P. Ramadhani, Deswati, *J. Serb. Chem. Soc.* **89** (2024) 123 (https://doi.org/10.2298/JSC230303084Z)
2. M. Vukčević, M. Maletić, B. Pejić, N. Karić, K. Trivunac, A. Perić Grujić, *J. Serb. Chem. Soc.* **88** (2023) 669 (https://doi.org/10.2298/JSC221213015V)
3. Z. Y. Velkova, G. K. Kirova, M. S. Stoytcheva, V. Gochev, *J. Serb. Chem. Soc.* **83** (2018) 107 (https://doi.org/10.2298/JSC170519093V)
4. N. Nourbakhsh, H. Zavvar Mousavi, E. Kolvari, A. Khaligh, *Appl. Chem. Today* **17** (2023) 33 (https://doi.org/10.22075/chem.2021.23896.1991)
5. M. Ghereghlou, A. A. Esmaeili, M. Darroudi, *Sep. Sci. Technol.* **57** (2022) 2005 (https://doi.org/10.1080/01496395.2022.2029490)
6. V. K. Veni, T. H. Brenda, *IOP Conf. Ser.: Earth Environ. Sci.* **765** (2021) 012039 (https://doi.org/10.1088/1755-1315/765/1/012039)
7. B. M. Thamer, A. Aldalbahi, M. Moydeen A, H. El-Hamshary, A. M. Al-Enizi, M. H. El-Newehy, *Mater. Chem. Phys.* **234** (2019) 133 (https://doi.org/10.1016/j.matchemphys.2019.05.087)
8. G. Sharma, M. Naushad, A. Kumar, S. Rana, S. Sharma, A. Bhatnagar, F. J. Stadler, A. A. Ghfar, M. R. Khan, *Process Saf. Environ. Prot.* **109** (2017) 301 (https://doi.org/10.1016/j.psep.2017.04.011)
9. J. A. Putri, A. Suratman, R. Roto, *J. Metastable Nanocrystall. Mater.* **34** (2022) 63 (https://doi.org/10.4028/v-4f958r)
10. A. O. Ezzat, A. M. Tawfeek, J. R. Rajabathar, H. A. Al-Lohedan, *Molecules* **27** (2022) 441 (https://www.mdpi.com/1420-3049/27/2/441)
11. A. O. Ezzat, A. M. Tawfeek, F. Mohammad, H. A. Al-Lohedan, *J. Mol. Liq.* **358** (2022) 119195 (https://doi.org/10.1016/j.molliq.2022.119195)
12. S. Dhananasekaran, R. Palanivel, S. Pappu, *J. Adv. Res.* **7** (2016) 113 (https://doi.org/10.1016/j.jare.2015.03.003)
13. P. F. de Sales, Z. M. Magriotis, M. A. L. S. Rossi, R. F. Resende, C. A. Nunes, *J. Environ. Manage.* **130** (2013) 417 (https://doi.org/10.1016/j.jenvman.2013.08.067)
14. G. R. Chaudhary, P. Saharan, A. Umar, S. K. Mehta, S. Mor, *Sci. Adv. Mater.* **5** (2013) 1886 (https://doi.org/10.1166/sam.2013.1701)
15. M. Altikatoglu, M. Celebi, *Artif. Cells Blood Substit. Biotechnol.* **39** (2011) 185 (https://doi.org/10.3109/10731199.2010.533124)
16. N. T. Abdel-GhANi, G. A. El-Chaghaby, E.-S. A. Rawash, E. C. Lima, *J. Chil. Chem. Soc.* **62** (2017) 3505 (https://doi.org/10.4067/S0717-97072017000200016)
17. S. Dehghan Abkenar, M. Hassannezhad, M. Hosseini, M. R. Ganjali, *J. Serb. Chem. Soc.* **84** (2019) 701 (https://doi.org/10.2298/JSC181228038D)
18. X.-S. Li, G.-T. Zhu, Y.-B. Luo, B.-F. Yuan, Y.-Q. Feng, *TrAC, Trends Anal. Chem.* **45** (2013) 233 (https://doi.org/10.1016/j.trac.2012.10.015)
19. M. Bordbar, N. Negahdar, B. Khodadadi, *J. Nanostruct.* **12** (2022) 262 (https://doi.org/10.22052/JNS.2022.02.005)
20. S. Rahnama, S. Shariati, F. Divsar, *Comb. Chem. High Through. Screen.* **21** (2018) 583 (https://doi.org/10.2174/1386207321666181019111211)

21. M. Khan, S. Naseer, M. Khan, R. Nazir, A. Badshah, Adnan, S. Shujah, A. Parveen, *Desal. Water Treat.* **228** (2021) 286 (https://doi.org/10.5004/dwt.2021.27352)
22. A. Ali Ahmed, Z. Hattab, Y. Berredjem, S. Hamoudi, R. Djellabi, *Desal. Water Treat.* **317** (2024) 100278 (https://doi.org/10.1016/j.dwt.2024.100278)
23. M. Erfani, R. Ansari, H. Zavvar Mousavi, *Appl. Chem. Today* **17** (2022) 149 (https://doi.org/10.22075/chem.2022.23980.1994)
24. S. Temel, E. Yaman, N. Ozbay, F. O. Gokmen, *J. Serb. Chem. Soc.* **85** (2020) 939 (https://doi.org/10.2298/JSC190517114T)
25. D. Kosale, C. Thakur, V. K. Singh, *J. Serb. Chem. Soc.* **88** (2023) 653 (https://doi.org/10.2298/JSC220830021K)
26. S. Jadali, S. M. Sajjadi, H. Zavvar Mousavi, M. Rajabi, *Anal. Bioanal. Chem. Res.* **4** (2017) 171 (https://doi.org/10.22036/abcr.2016.67517.1122)
27. M. Hadnađev Kostić, T. Vulić, Đ. Karanović, M. Milanović, *J. Serb. Chem. Soc.* **87** (2022) 1011 (https://doi.org/10.2298/JSC220228034H)
28. Z. Lotfi, H. Z. Mousavi, S. M. Sajjadi, *Anal. Methods* **9** (2017) 4504 (https://doi.org/10.1039/C7AY01166K)
29. J. Rahchamani, H. Z. Mousavi, M. Behzad, *Desalination* **267** (2011) 256 (https://doi.org/10.1016/j.desal.2010.09.036)
30. S. M. Seyed Danesh, H. Faghihian, S. Shariati, *J. Nano Res.* **52** (2018) 54 (https://doi.org/10.4028/www.scientific.net/JNanoR.52.54)
31. Z. Dahaghin, H. Z. Mousavi, L. Boutorabi, *J. Mol. Liq.* **243** (2017) 380 (https://doi.org/10.1016/j.molliq.2017.08.018)
32. S. Eftekhari, M. R. Sohrabi, S. Mortazavinik, *Iran. J. Chem. Chem. Eng.* (2024) (https://doi.org/10.30492/ijcce.2024.2016928.6343)
33. D. Marković, S. Milovanović, M. Radoičić, Ž. Radovanović, I. Zizovic, Z. Šaponjić, M. Radetić, *J. Serb. Chem. Soc.* **83** (2018) 1379 (https://doi.org/10.2298/JSC180913089M)
34. C. A. P. Almeida, N. A. Debacher, A. J. Downs, L. Cottet, C. A. D. Mello, *J. Colloid Interface Sci.* **332** (2009) 46 (https://doi.org/10.1016/j.jcis.2008.12.012)
35. I. Espinoza, C. Sandoval Pauker, L. Ramos Guerrero, P. Vargas Jentzsch, F. Muñoz Bisesti, *J. Serb. Chem. Soc.* **85** (2020) 547 (https://doi.org/10.2298/JSC190804119E)
36. A. A. Fodeke, O. O. Olayera, *J. Serb. Chem. Soc.* **84** (2019) 1143 (https://doi.org/10.2298/JSC190209042F)
37. S. K. Hassaninejad-Darzi, H. Z. Mousavi, M. Ebrahimpour, *J. Mol. Liq.* **248** (2017) 990 (https://doi.org/10.1016/j.molliq.2017.10.126)
38. K. Gul, H. Khan, N. Muhammad, B. Ara, T. U. H. Zia, *Sep. Sci. Technol.* **56** (2021) 2507 (https://doi.org/10.1080/01496395.2020.1839498)
39. A. C. Enache, P. Samoila, C. Cojocaru, R. Apolzan, G. Predeanu, V. Harabagiu, *Sustainability* **15** (2023) 2704 (https://doi.org/10.3390/su15032704)
40. I. Badran, R. Khalaf, *Sep. Sci. Technol.* **55** (2020) 2433 (https://doi.org/10.1080/01496395.2019.1634731).

Journal of the Serbian Chemical Society
JSCS@tmf.bg.ac.rs • www.shd.org.rs/JSCS
J. Serb. Chem. Soc. 90 (3) S91–S94 (2025) *Supplementary material*

SUPPLEMENTARY MATERIAL TO

Application of magnetite nanoparticle-modified walnut shell as an adsorbent for the removal of the organic dye Coomassie Brilliant Blue R-250

MOZHGAN BIUKI, HASSAN ZAVVAR MOUSAVI*, MAJID ARVAND and HADI FALLAH MOAFI

Faculty of Chemistry, Department of Analytical Chemistry, University of Guilan, Rasht, Iran

J. Serb. Chem. Soc. 90 (3) (2025) 311–324

The percentage removal and the amount of unabsorbed dye on the nanoparticles were calculated using Equations S-1 and S-2.

$$\text{Removal\%} = \frac{C_i - C_f}{C_i} \times 100 \quad \text{(S-1)}$$

$$q_e = \frac{(C_i - C_f) \times V}{W} \quad \text{(S-2)}$$

In the above equations, C_i / mg L^{-1} represents the initial concentration, and C_e / mg L^{-1} represents the unadsorbed or equilibrium concentration. Additionally, q_e / mg g^{-1} represents the adsorption capacity at equilibrium, V / L represents the volume of the solution, and w / g represents the amount of adsorbent.

The equilibrium adsorption isotherms are valuable for determining the distribution of absorbate molecules between the liquid and solid phases at equilibrium during the adsorption process.

$$\frac{C_e}{q_e} = \frac{1}{q_m b} + \frac{C_e}{q_m} \quad \text{(S-3)}$$

$$ln\, q_e = ln\, k_F + \frac{1}{n} ln\, C_e \quad \text{(S-4)}$$

$$q_e = B_T\, ln\, A_T + B_T\, ln\, C_e \quad \text{(S-5)}$$

$$ln\, q_e = ln\, q_m - \beta \varepsilon^2 \quad \text{(S-6)}$$

In the above equations, C_e / mg L^{-1} represents the equilibrium concentration of the solution, q_e / mg g^{-1} denotes the adsorption capacity at equilibrium, q_m / mg g^{-1} represents the maximum adsorption capacity, b / L mg^{-1} stands for the Langmuir constant, k_F / (mg g^{-1}) (L mg^{-1}) $^{(1/n)}$ represents the Freundlich constant where $1/n$ is the heterogeneity factor indicating the nature of the desired adsorption process. B_T / L mol^{-1} and A_T / L g^{-1} are the Temkin constants. β / mol^2 kJ^{-2} represents the useful activity coefficient and ε / kJ mol^{-1} is the Polanyi potential.

* Corresponding author. E-mail: hzmousavi@guilan.ac.ir

The linear plots (Fig. S-1) for the Langmuir (equation S-3), Freundlich (equation S-4), Temkin (equation S-5), and Dubinin-Radushkevich (equation S-6) equations are obtained by plotting C_e/q_e against C_e, $\ln q_e$ against $\ln C_e$, q_e against $\ln C_e$, and $\ln q_e$ against ε^2, respectively.

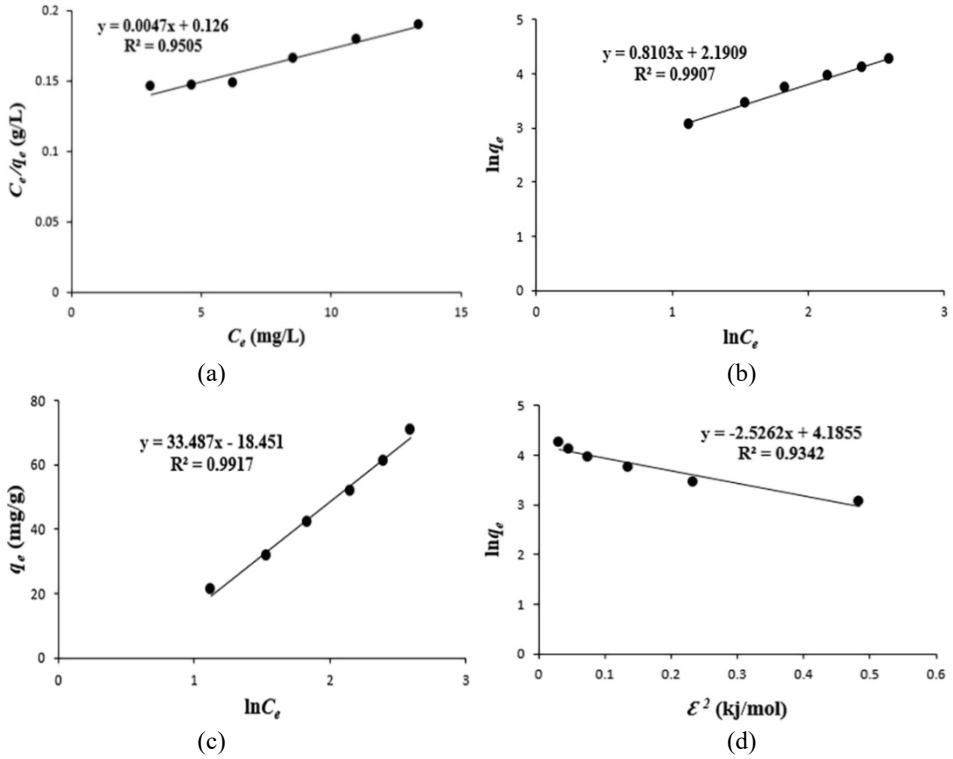

Fig. S-1. Graphs related to equilibrium adsorption isotherms: a) Langmuir, b) Freundlich, c) Temkin, and d) Dubinin-Radushkevich for the adsorption of CBB.

Two kinetic models were employed to determine the better fit: the pseudo-first-order Lagergren model (equation S-8) and the pseudo-second-order Ho model (equation S-9):

$$\frac{dq}{dt} = k_1(q_e - q_t) \tag{S-7}$$

In equation S-7, q_e / mg g^{-1} and q_t / mg g^{-1} represent the adsorption capacities at equilibrium and time t, respectively. k_1 / min^{-1} is the rate constant for surface adsorption in thepseudo-first-order kinetic model. By taking the natural logarithm of both sides of equation 7, another form of the pseudo-first-order kinetic equation is obtained, known as the Lagergren equation:

$$ln(\, q_e - q_t) = ln\, q_{e1} - k_1 t \tag{S-8}$$

In that equation, q_{e1} represents the adsorption capacity obtained based on the pseudo-first-order kinetic model. By plotting a linear graph of $ln(q_e - q_t)$ against t and analyzing the slope and intercept, the values of k_1 and q_{e1} can be determined. The pseudo-second-order kinetic equation, based on the adsorption capacity, is presented as follows:

$$\frac{dq}{dt} = k_2(q_e - q_t)^2 \quad \text{(S-9)}$$

In this equation, k_2 / g (mg min) $^{-1}$ represents the rate constant for the pseudo-second-order kinetic equation. By integrating and rearranging this equation, an another form of the equation can be obtained, as follows:

$$\frac{t}{q_t} = \frac{1}{k_2 {q_{e2}}^2} + \frac{t}{q_{e2}} \quad \text{(S-10)}$$

In the above equation, q_{e2} / mg g $^{-1}$ represents the adsorption capacity obtained based on the pseudo-second-order kinetic model.

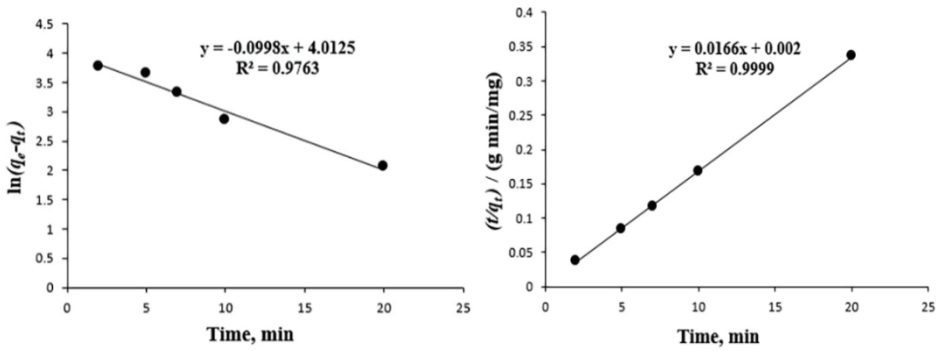

(a) (b)

Fig. S-2. Kinetic graphs of: a) pseudo-first order and b) pseudo-second order for the adsorption of CBB.

In this study, thermodynamic parameters of adsorption such as the changes in Gibbs energy ($\Delta G°$), enthalpy ($\Delta H°$), and entropy ($\Delta S°$) related to the equilibrium constants of adsorption were obtained using equations (S-11) to (S-14). For significant adsorption, the change in Gibbs energy should be negative. The change in Gibbs free energy of adsorption is defined as follows:

$$\Delta G^o = -RT \ ln K_c \quad \text{(S-11)}$$

In that equation, T / K is the temperature, R / 8.314 J mol $^{-1}$K^{-1} is the universal gas constant, and K_c / mg L^{-1} is the equilibrium constant of adsorption. The relationship is expressed as follows:

$$K_c = \frac{q_e}{C_e} \quad \text{(S-12)}$$

In this equation, q_e / mg L^{-1} represents the equilibrium concentration of the adsorbate species on the adsorbent, and C_e / mg L^{-1} represents the equilibrium concentration of the adsorbate species in the solution. Other thermodynamic

variables, such as the change in Gibbs energy, the change in enthalpy, and the standard entropy change of adsorption, can be obtained using the following equation:

$$\Delta G^o = \Delta H^o - T\Delta S^o \quad \text{(S-13)}$$

The thermodynamic parameters such as the changes in enthalpy ($\Delta H°$) and entropy ($\Delta S°$) can also be obtained from the Van't Hoff equation:

$$ln\, K_c = \frac{\Delta S^o}{R} - \frac{\Delta H^o}{RT} \quad \text{(S-14)}$$

Table S-I. Impact of Temperature on the Removal Efficiency of CBB

T / K	q_{exp} / mg g^{-1}	Removal, %
273	10.10	96.16
283	9.19	94.70
298	7.87	92.60
308	6.87	91.00

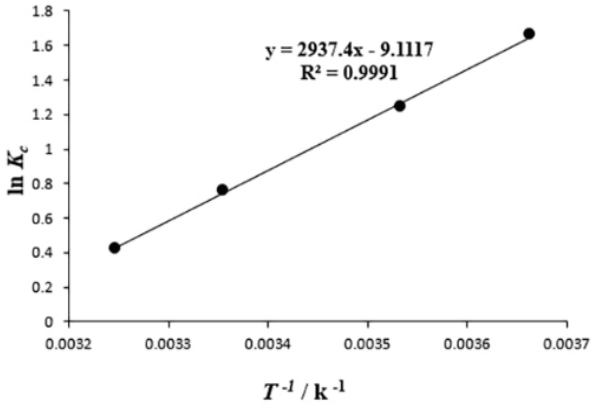

Fig S-3. Thermodynamic graph versus temperature in Kelvin for CBB.

Journal of the Serbian Chemical Society
JSCS-info@shd.org.rs • www.shd.org.rs/JSCS
J. Serb. Chem. Soc. 90 (3) 325–338 (2025)
JSCS–5390
Original scientific paper
Published 24 March, 2025

Recovery of copper from pre-concentrated printed circuit boards (PCBs) by catalyzed acidic leaching

ÖZGE GÖK*

Dokuz Eylul University, Faculty of Engineering, Mining Engineering Department, İzmir, Turkiye

(Received 10 May, revised 4 June, accepted 6 October 2024)

Abstract: This study aimed to extract copper from waste printed circuit boards (WPCBs) through a sequential process involving physical pre-concentration via a shaking table, followed by acid leaching. A shredder and hammer mill were utilized to fragment the various components of the PCB into particles smaller than 1 mm. The shaking table pre-concentration tests revealed that the heavy fraction exhibited a copper grade of 56.4 % with a yield of 89.6 %. Subsequent leaching of the copper concentrate, using a solution containing 1 M H_2SO_4 and 4 vol. % H_2O_2 at 50 °C for two hours, resulted in a copper extraction efficiency exceeding 95 % with a solid ratio of 2 wt. %/*V*.

Keywords: printed circuit board; copper; leaching; recovery; shaking table.

INTRODUCTION

The rapid pace of development in today's world has led to a significant accumulation of waste electrical and electronic equipment (WEEE), commonly referred to as E-waste due to the short lifespan of these products. In recent years, the growing global concern over environmental issues has prompted researchers to implement various recycling strategies for extracting metals from E-waste. The main driving force behind the deve lopment of these recycling strategies is the increasingly stringent policies and regulations governing industries and landfill areas. Improper management of WEEE can lead to environmental issues due to the presence of hazardous inorganic substances like mercury (Hg) and lead (Pb), as noted in the literature.[1–3]

WEEE is a valuable source of base metals like copper, as well as precious metals such as gold, silver, platinum and palladium, which are comparable in content to those found in ores and concentrates. As such, recycling WEEE is crucial for both environmental preservation and economic gain, as noted in litera-

* Corresponding author. E-mail: ozge.solak@deu.edu.tr
https://doi.org/10.2298/JSC240510086G

ture.[4–6] Additionally, recycling WEEE has been highlighted as an important measure for both environmental and economic benefits.[7–9]

Printed circuit boards (PCBs), computers, and other forms of electronic waste (E-waste) contain a high concentration of base metals, particularly copper. In fact, the weight percentage of copper obtained from PCBs can range from 16––30 %, which is significantly higher than any other metal found in E-waste. By comparison, copper found in ores typically only ranges from 0.5–1 %.[10]

Various researchers have proposed physical,[11–15] pyrometallurgical,[16–18] hydrometallurgical,[19–23] and biometallurgical[24,25] methods based on conventional techniques for recovering metals from E-waste. While physical and pyrometallurgical processes are widely used in industrial applications of E-waste recycling, recent attention on metal recovery has shifted towards hydrometallurgical processing. In general, pre-treatment steps, such as separating different parts of electronic and electrical products, are necessary for metal recovery from E-waste through size reduction and hydrometallurgical processes. In industrial processes, e-waste is typically fed into chemical process for metal recovery immediately after physical separation and pyrometallurgical process.[3,26]

Furthermore, various leaching studies have also been conducted using many different reagents.[27,28] According to Montero *et al.*[29] during column leaching of waste printed circuit boards, using cyanide solutions, copper was found to dissolve simultaneously at a rate of 77 %. However, direct cyanidation led to increased cyanide consumption and decreased recovery of precious metals. To address this issue, pre-leaching is recommended to dissolve or remove copper and other base metals before extracting precious metals using cyanide, thiosulfate, thiourea, or chloride media. Quinet *et al.*,[21] Oh *et al.*[20] and Kamberović *et al.*[30] have suggested an acidic sulfate leaching with an appropriate oxidant prior to extracting precious metals.

The investigation on various inorganic acids and oxidants used for metal recovery revealed that the highest Cu recovery was obtained with nitrate and chloride solutions.[22] Mecucci and Scott[19] reported > 95 % dissolution of Cu from circuit boards using HNO_3. Kinoshita *et al.*[31] found similar results with Cu recovery of > 90 %. The use of nitric acid can be costly due to its oxidative nature; sulfuric acid with additives such as H_2O_2, O_2 and Fe^{3+} can be a more affordable and favorable option over other processes.

In the literature, leaching methods with two chemicals were reported to extract both base and precious metals from waste printed circuit boards (WPCBs). They utilized sulfuric acid with hydrogen peroxide for the first group of metals, while they used thiourea with the ferric ion in sulfuric acid medium for the second group of metals.[32] The optimal conditions for copper extraction were found to be 2M H_2SO_4 (98 %), 5 % H_2O_2, 85 °C temperature, 1/10 solid-to-

-liquid ratio and 200 rpm. Many investigators[33–37] have utilized distinct oxidizing agents, including H_2O_2, O_2 and Fe^{3+}, for leaching copper in H_2SO_4.

Sulfuric acid and hydrogen peroxide have both a role of oxidizing and reducing agent in metal component dissolution, and their standard-state free energy ($\Delta G°$) can be expressed as follows:[6]

$$Cu + H_2SO_4 + H_2O_2 \rightarrow CuSO_4 + 2H_2O,\ \Delta G° = -326.105\ \text{kJ mol}^{-1} \quad (1)$$

The second reaction represents the decomposition of H_2O_2 into H_2O and O_2, and it can be accelerated using catalysts such as MnO_2 or KI:

$$2H_2O_2 \rightarrow 2H_2O + O_2 \quad (2)$$

Sulfuric acid forms peroxysulfuric acid (Caro's acid, H_2SO_5) on reaction with hydrogen peroxide (Eqs. (2) and (3)). This is a strong oxidizer for copper and assists in the dissolution of other metals. Copper dissolution with H_2SO_5 at the controlled-experimental conditions is shown in Eq. (4):[38]

$$H_2SO_4 + H_2O_2 \rightarrow H_2SO_5 + H_2O \quad (3)$$

$$Cu + H_2SO_5 \rightarrow Cu^{2+} + SO_4^{2-} + H_2O \quad (4)$$

It can be prepared from concentrated hydrogen peroxide and concentrated sulfuric acid. However, it is generated and consumed immediately at the point of use because of its exothermic nature. Therefore, with the use of diluted sulfuric acid and hydrogen peroxide solutions at higher temperatures than 10 °C, the primary oxidation mechanism with hydrogen peroxide involves electron transfer, stemming from the weak H–O bond dissociation, resulting in oxygen serving as an electron acceptor.

The focus of this study is on the chemical recovery of copper, concentrated from a physical treatment process, specifically gravity concentration of PCBs. A shaking table was chosen for the physical separation step, while acidic leaching was preferred for the hydrometallurgical process.

MATERIAL AND METHOD

In this study, chemical leaching methods were conducted on the concentrate gained by the shaking table method. Similar gravimetric enrichment method of waste PCBs after removal of electronic components (resistor, capacitor, diode, transistor, *etc*.) was explained in the study of Gok and Sen.[39]

The essential purpose of the crushing process in WPCB recycling is to separate metals from non-metals, that is playing a vital role in the recovery of metals from WPCBs. This process is closely tied to the subsequent selective recovery of metals.[40] Pre-concentration methodology includes comminution and gravimetric concentration using shaking table. Employing a two-step crushing approach prior to the pre-concentration step (shaking table) has proven to be effective in dismantling WPCBs. A single shaft shredder knife crusher was used to break down WPCB plates into smaller particles (~10 mm). Subsequently, these smaller particles undergo further crushing in a hammer grinder for WPCBs, featuring 1 mm diameter screen

holes. Closed circuit pulse-jet bag filters collected and recycled the dust throughout the comminution. Particle classification and size control was conducted using a vibratory sieve.

The graphical flowsheet of process steps is illustrated in Fig. 1.

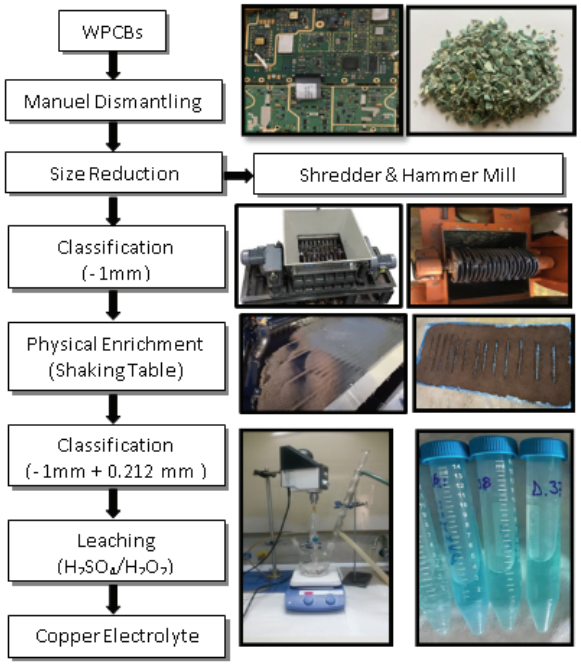

Fig.1. Gravimetric enrichment flowsheet of the waste PCBs.

Pre-concentration of copper particles was carried out using a Wilfley shaking table to recover the copper particles, presenting a promising technique to mitigate dust-related issues. This technique involves the separation of materials based on particle density on inclined planes with smoothed or grooved surfaces, achieved through the back-and-forth vibration of the pulp material while wash water flows. The underlying principle relies on segregating rapidly moving coarse light particles from slowly moving small dense particles within the flowing water film through longitudinal vibration. The optimal settings of concentration with shaking table are presented in Table I.

TABLE I. Optimal operating parameters and results of shaking table enrichment

Particle size, mm	~1
Wash water flowrate, L/min	12
Deck angle, °	2
Motion frequency, Hz	60
Cu grade, %	56.40
Cu yield, %	89.56

Chemical dissolution of the sample in aqua regia and spectroscopic analyses of the electrolytes on Analytik Jena NovaA 300 AAS indicated that major component was copper.

Table II presents the chemical components of PCB feed material (~1 mm) and concentrate for four size fractions. Apart from the metal fraction indicated for the samples, it was observed that the remaining parts consisted of polymer and ceramic. Sieve analyses and fractioning were conducted using a vibratory laboratory sieve shaker for 20 min. Three different fractions of the concentrate samples were used at leaching tests: -1000+500 μm; -500 + 300 μm; and -300+212 μm (Table I). -212 μm fraction consisted of higher metallic content such as Fe, Zn, Pb, Ni, Mn than larger size fractions. Thus, this smallest size fraction was not included in leaching experiments.

TABLE II. Chemical analysis of PCB feed and concentrate samples

Sample	Weight, %	Component $d_{particle}$, μm	Cu	Ni	Pb	Zn	Fe	Mn
Feed	100	-1000	16.78	1.13	1.40	0.59	0.10	0.15
Concentrate	30.95	-1000+500	67.42	1.69	2.85	0.96	2.35	0.27
	30.60	-500+300	63.13	1.33	1.91	1.18	2.40	0.22
	25.62	-300+212	47.38	1.19	1.78	1.51	3.32	0.44
	12.83	-212	20.43	3.35	5.56	5.07	14.83	2.21

Rigaku Miniflex II diffractometer with CuKα radiation was used for X-ray diffraction analyses of samples. XRD analysis of PCB concentrate revealed the presence of polymer, ceramic, solder and copper as major components. The microscope analysis given in Fig. 2. also supported XRD analysis. The microscopic analysis of PCB concentrate revealed the presence of liberated copper particles smaller than 1 mm, as well as particles containing traces of Fe, Ni and Pb. Additionally, black-colored solder particles, yellow-colored glass fibers, and green--colored resin particles smaller than 1 mm were observed.

Fig. 2. Optical microscope pictures of the shaking table concentrate at ×8 magnification.

The main purpose of the research was to investigate optimal parameters of the acid leaching of copper from pre-concentrated PCBs. A 5 g of PCBs concentrate were immersed in leaching reagent saturated with an oxidant. Leaching tests were performed in a 0.50-L four--necked glass reactor equipped with a condenser. The temperature was controlled within ±2 °C using a glass-coated temperature sensor in conjunction with a hot plate. Typically, the vessel was charged with an electrolyte containing H_2SO_4 (0.5–1.5 M) and H_2O_2 (2–8 vol. %) and sample at three particle size fractions (1000–500 μm, 500–300 μm, 300–212 μm) with 1––8 wt. %/*V* solid/volume ratio. The initial temperatures of the solution were selected as 30, 50 and 70 °C, and the reaction was sustained for 2 h. The solution was mixed with a mechanical

stirring rate of 10 rounds/s by a magnetically driven twin impeller. 5 ml of pregnant solutions were withdrawn to determine copper concentration using Analytik Jena NovaA 300 AAS.

RESULTS AND DISCUSSION

The dissolution efficiency of copper from PCB concentrate was established in the presence of an oxidant with various pulp ratios, particle sizes, temperatures and acid concentrations. Except for the experiments designed to determine the effect of solid ratio, all tests were conducted with an optimum solid ratio of 2 wt. %/*V*.

Effect of particle size

Experiments conducted with three different particle size fractions (1000–500 μm, 500–300 μm, 300–212 μm) in 1 M H_2SO_4 and 4 % H_2O_2 solution at 30 °C to determine leaching time have revealed no significant difference in leaching efficiency after 90 min (Fig. 3). In the particle size range of 300–212 μm, the finest particle size interval, a leaching efficiency of over 90 % copper has been achieved in one hour. The results indicate that after two hours, the recovery is around 85 % for the 1000–500 μm fraction, and 90 % for the 500–300 μm fraction. After 2 h of leaching, a 15 % difference in copper recovery was observed between the largest and smallest sizes of PCB samples. In the fine particle size fraction, the reaction rate increases due to the higher percentage of liberated copper particles. This leaching method represents a classic heterogeneous reaction system, and therefore it is obvious that the larger surface area due to the smaller particle size has a beneficial effect. It is evident that grinding to finer sizes incurs additional costs. However, as seen from the graph, the copper recovery achieved within 1 h at the 300–212 μm size was attained only after 2 h for the 1000–500 μm particle size.

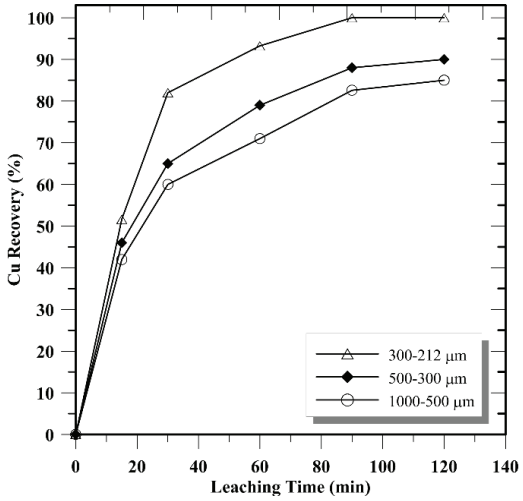

Fig. 3. Effect of the particle size on copper recovery. Initial electrolyte conditions: $C_{H_2SO_4}$ = 1M, $y_{H_2O_2}$ = 4 vol. %, t = = 30 °C.

Effect of acid concentration

The influence of the acid concentrations of the copper recovery was investigated with various particle size fractions (1000–500 μm, 500–300 μm, 300–212 μm) using electrolyte containing 4 vol. % H_2O_2 at 50 °C. The values in Fig. 4 reveal that high levels of copper extraction, typically around 90 %, were achieved with 1.5 M H_2SO_4 and 300–212 μm fraction at 50 °C. The leaching experiments conducted with 1.5 M H_2SO_4 demonstrated that the coarser particle size fractions resulted in lower recovery rates. Specifically, the recovery for the 1000–500 μm fraction was approximately 65 %, while the recovery for the 500–300 μm fraction was around 80 %. Although copper recovery improved with increasing concentration, the rate of improvement diminished for smaller size fractions at concentrations exceeding 1 M H_2SO_4. The solvent effect of H_2SO_4 has been observed to be less pronounced in larger particle sizes compared to finer sizes. Researchers explained that this type of decrease in efficiency usually was indicative of a reaction controlled by diffusional effects. Hence, as the particle size increases, the leaching kinetics decrease.

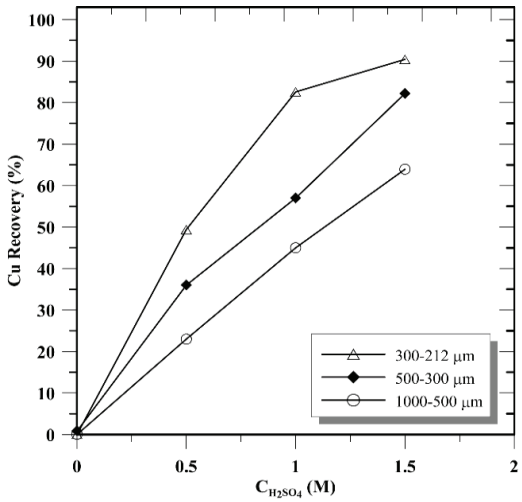

Fig. 4. Effect of the acid concentration on copper recovery. Initial electrolyte conditions: $y_{H_2O_2}$ = 4 vol. %, t = 50 °C.

Effect of oxidant concentration

The effect of H_2O_2 concentration (2–8 vol. %) on the copper leaching was elucidated with three size fractions (1000–500 μm, 500–300 μm, 300–212 μm) using in the solutions containing 1 M H_2SO_4 at 50 °C. The contribution of an oxidant is revealed in Fig. 5. The oxidizing effect created at a concentration of 6 % H_2O_2 has been observed to facilitate the leaching of all copper with the smallest size fraction. With this amount of hydrogen peroxide used, the copper recovery for the finest size fraction was found to be 25 % higher than that obtained for the coarsest size fraction. The results obtained with 8 % H_2O_2

revealed a recovery rate of 85 % for the 1000–500 μm particle size fraction, while the recovery for the 500–300 μm fraction exceeded 90 %. At higher concentrations of H_2O_2, there is a reduced requirement for fine particle size. The decomposition rate of hydrogen peroxide is quite high. Therefore, it is thought that the oxidation of copper by peroxide in coarser samples, such as those in the 1000–500 μm range, occurs more slowly due to the lower diffusion rate.

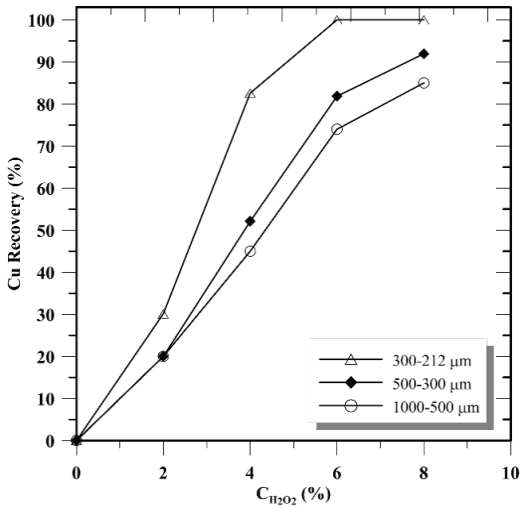

Fig. 5. Effect of the oxidant concentration on copper recovery. Initial electrolyte conditions: 1 M H_2SO_4, t = 50 °C.

Effect of the temperature

The temperature effect on the results of copper extraction in the electrolyte containing 4 vol. % H_2O_2 and 1 M H_2SO_4 at various temperatures (30, 50 and 70 °C) are shown in Fig. 6. The leaching tests indicated that with 300–212 μm size fractions copper recovery at 30 °C was completed within 90 min. In comparison, the recovery rate reached approximately 90 % at 50 °C and exceeded 80 % at 70 °C. It has been observed that within the fine particle range, a 20 % increase in leaching efficiency occurs as the reaction temperature decreases. Thus, temperature increase had adverse effect. It was noted that temperature increase led to the rapid decomposition of H_2O_2, which caused a decrease in the oxidant behavior. Temperatures above 50 °C do not significantly affect leaching efficiency.

Effect of solid ratio

A solid ratio of 2 % and low acid/oxidant concentration (1 M H_2SO_4, 4 vol. % H_2O_2) have yielded efficiencies exceeding 95 % with 300–212 μm fraction at 50 °C. Effect of the solid ratio on copper recovery is shown in Fig. 7. Experiments conducted with an 8 % solid-to-liquid ratio resulted in copper recoveries of approximately 80 % for the 300–212 μm size fraction, 70 % for the 500–300 μm fraction, and around 60 % for the 1000–500 μm fraction. The observed variation

in the curvature trend in fine particle sizes is interpreted as the diffusion becoming more challenging with an increase in pulp ratio in larger particle sizes.

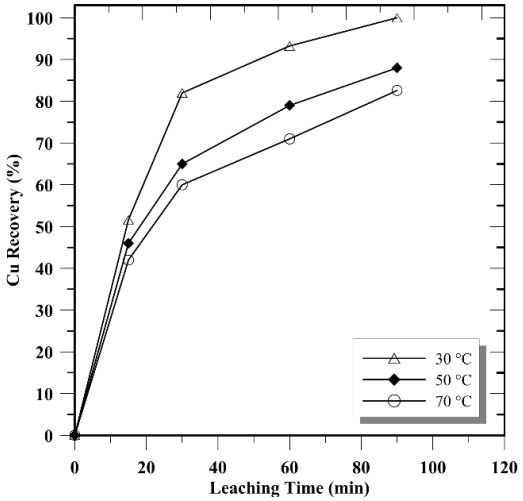

Fig. 6. Effect of the temperature on copper recovery. Initial electrolyte conditions: 1 M H_2SO_4, $y_{H_2O_2}$ = 4 vol. %, d_p 300–212 μm.

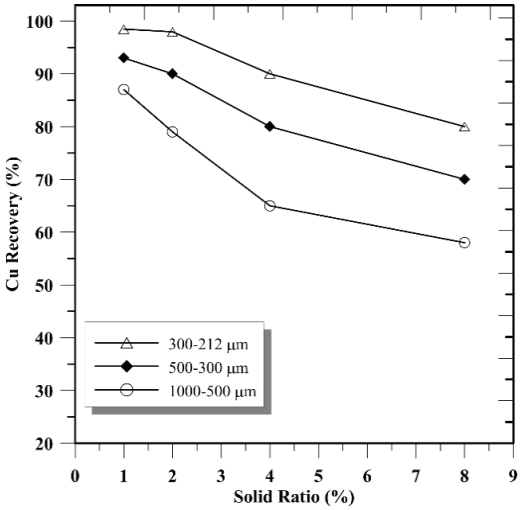

Fig. 7. Effect of the solid ratio on copper recovery. Initial electrolyte conditions: 1 M H_2SO_4, $y_{H_2O_2}$ = 4 vol. %, t = 50 °C.

The copper recovery results obtained in this research was found similar with the studies in the literature[6,20,34,41,42] on the copper leaching from PCBs with higher H_2SO_4 + H_2O_2 concentrations. It was thought that this was due to the pre-concentration step in which plastic part, preventing the dissolution, is eliminated.

Kinetic analysis

The primary consideration in understanding a leaching system is its mechanism, with an in-depth knowledge of the kinetics of the rate-controlling pro-

cesses and the solid reaction products being essential for a thorough comprehension of the system. Kinetic analysis was conducted to elucidate the reaction mechanism of a non-catalytic heterogeneous reaction. The kinetic parameters and activation energy of the copper dissolution in oxidized sulfuric acid electrolytes was evaluated. The reaction between solid particles and solution may have its rate-controlling step attributed to one of the following factors: external diffusion of the reactant through the boundary layer of the fluid enveloping the particle (film diffusion controlled), surface reaction between the fluid reactant and the solid (chemical reaction controlled) or internal diffusion of the reactant through the reaction products on the particle (ash diffusion controlled):[43,44]

– Film diffusion control dense constant size small particles – all geometries:

$$X = K_c \tau \quad (5)$$

– Chemical reaction control dense constant size or shrinking spheres:

$$1 - (1 - X)^{1/3} = K_c \tau \quad (6)$$

– Ash diffusion control dense constant size-spherical particles:

$$1 - 3(1 - X)^{2/3} + 2(1 - X) = K_c \tau \quad (7)$$

where reaction rate constant is K_c / min^{-1}, time, τ / min and fraction of copper reacted, X / %.

The data obtained from the kinetic analysis at different temperatures were tested by the equations of the shrinking core models (Eqs. (5)–(7)). As seen in Table III and Fig. 8, the regression coefficient in the chemically reaction-controlled kinetic model was found to be closer to 1 only for 30 °C. For higher temperatures, the values appear to be less-linearized. The result data fitted with the ash diffusion controlled shrinking spheres model, *i.e.*, Eq. (7). This model indicated the highest value of regression coefficient R^2 and the constant value of K_c was obtained. The reaction rate constant at 30 °C was determined to be 0.0111 min^{-1}, and the reaction rate decreased as the temperature increased. Although the PCB solid samples were concentrated by shaking table method, a polymeric matrix was still present during leaching. This may have caused the diffusion of the electrolyte in the leaching process to become the rate-determining step. Since the chemical reaction-controlled model does not exhibit a linear trend at high temperatures, the ash-controlled reaction model was preferred for activation energy cal-

TABLE III. Apparent rate constants and correlation coefficients for shrinking core models

T / K	Chemical reaction controlled $1 - (1 - X)^{1/3}$		Ash diffusion controlled $1 - 3(1 - X)^{2/3} - 2(1 - X)$	
	K_c / min^{-1}	R^2	K_c / min^{-1}	R^2
303	0.0111	0.9447	0.0111	0.9954
323	0.0064	0.9194	0.0059	0.9965
343	0.0055	0.9108	0.0046	0.9961

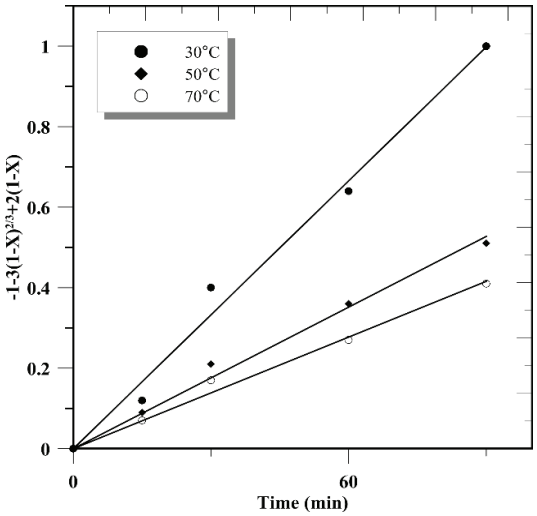

Fig. 8. Plot of the ash diffusion controlled shrinking core model for the effect of temperature on the copper recovery reaction rate.

culations. As shown in Fig. 8, the reaction rate constant values tend to decrease with increasing temperature. This is attributed to the rapid decomposition of hydrogen peroxide and the subsequent loss of the oxidant, which prevents the copper leaching rate from reaching sufficiently high reaction rates.

The activation energy, $E_a = -19.17$ kJ mol^{-1}, was determined from the slope of straight line plotted between ln k and $10^3/T$ as seen on Fig. 9. Thus, the determined activation energy indicates that the copper leaching from PCBs, using H_2SO_4–H_2O_2 in the range of 303–343 K, occurs in constant zone.

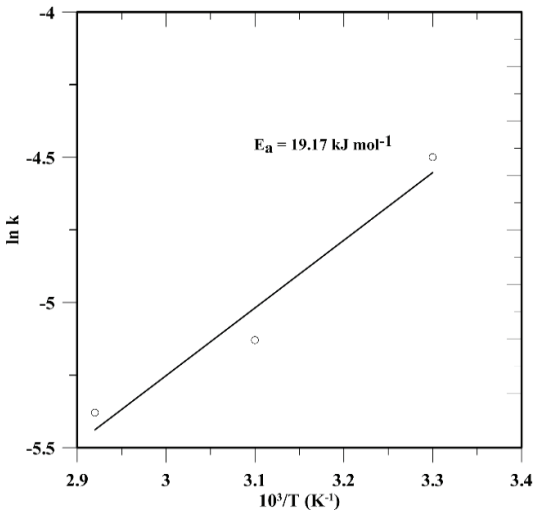

Fig. 9. Plot of parabolic leaching rate constants *vs*. inverse of temperature (Arrhenius plot).

CONCLUSION

• The investigation involved the dissolution of copper in an oxidized acidic electrolyte (H_2SO_4–H_2O_2) under varying conditions such as particle size, solid ratios, temperatures, and oxidant concentrations to elucidate the leaching kinetics of copper in waste printed circuit boards (WPCBs).

• The chemical, X-ray diffraction (XRD), and optical analyses collectively suggested that the disassembly of electronic components in WPCBs, coupled with a two-step comminution process and physical pre-concentration, facilitates the copper dissolution process.

• Copper pre-enrichment was achieved through a shaking table, reducing particle size to under 1 mm, with a wash water flow rate of 12 L/min, a 2° deck angle, and a motion frequency of 60 Hz. The resulting copper concentrate exhibited a grade and yield of 56.40 and 89.56 %, respectively.

• A 90 % copper recovery rate was achieved within 60 min at 30 °C in a 1 M sulfuric acid solution containing 4 vol. % hydrogen peroxide. The incorporation of oxidant and size reduction promoted the disproportionate dissolution of copper in plastic under all experimental conditions, with temperature variations showing reverse impact on copper recovery.

• Copper leaching from silicate-rich WPCBs was determined to be governed by ash diffusion. The dissolution rate constant was calculated as 0.0111 min^{-1} at 30 °C, with a regression constant of 0.9954. The activation energy (E_a) for the process was estimated to be 19.17 kJ mol^{-1}.

• The proposed process flowsheet, outlined in this study, can be readily adapted for industrial plant applications. Despite the apparent economic impracticality of using oxidant in large-scale operations due to its high cost, this method holds promise as an alternative to existing pyrometallurgical and hydrometallurgical applications, including those involving aggressive reactant.

ИЗВОД

ЕКСТРАКЦИЈА БАКРА ИЗ ПРЕД-КОНЦЕНТРИСАНИХ ШТАМПАНИХ ПЛОЧА (PCB) ПУТЕМ КАТАЛИЗОВАНОГ КИСЕЛИНСКОГ ИЗЛУЖИВАЊА

ÖZGE GÖK

Dokuz Eylul University, Faculty of Engineering, Mining Engineering Department, İzmir, Turkiye

Ова студија је за циљ имала издвајање бакра из отпадних штампаних плоча (WPCB) секвенцијалним процесом који укључује физичку пред-концентрацију на тресећем столу, а затим киселинско излуживање. За фрагментацију различитих компоненти штампаних плоча на честице мање од 1 mm коришћени су дробилица и чекићни млин. Тестови пред-концентрације помоћу тресећег стола су показали да тешка фракција има садржај бакра од 56,4 % са приносом од 89,6 %. Након тога је излуживање бакра из концентрата извршено третирањем раствором који садржи 1 M H_2SO_4 and 4 запр. % H_2O_2 на 50 °C током два сата, што је резултирало ефикасношћу екстракције бакра већом од 95 % са односом чврсте материје од 2 мас. %/*V*.

(Примљено 10. маја, ревидирано 4. јуна, прихваћено 8. октобра 2024)

REFERENCES

1. X. L. Xu, J. Y. Li, *J. Qingdao Univ.* **26** (2011) 69
2. Y. Lu, Z. Xu, *Resour. Conserv. Recycl.* **113** (2016) 28 (https://doi.org/10.1016/j.resconrec.2016.05.007)
3. A. Akcil, C. Erust, C. S. Gahan, M. Ozgun, M. Sahin, A. Tuncuk, *Waste Manage.* **45** (2015) 258 (https://doi.org/10.1016/j.wasman.2015.01.017)
4. T. Havlik, D. Orac, M. Petranikova, A. Miskufovla, *Waste Manage.* **31** (2011) 1542 (https://doi.org/10.1016/j.wasman.2011.02.012)
5. A. Tuncuk, V. Atazi, A. Akcil, E. Y. Yazici, H. Deveci, *Miner. Eng.* **25** (2012) 28 (https://doi.org/10.1016/j.mineng.2011.09.019)
6. I. Birloaga, I. De Michelis, F. Ferella, M. Buzatu, F. Vegliò, *Waste Manage.* **33** (2013) 935 (http://doi.org/10.1016/j.wasman.2013.01.003)
7. R. Wildmer, H. Oswald-Krapf, D. Sinha-Khetriwal, M. Schnellmann, H. Böni, *Environ. Impact Assess. Rev.* **25** (2005) 436 (https://doi.org/10.1016/j.eiar.2005.04.001)
8. B. H. Robinson, *Sci. Total Environ.* **408** (2009) 183 (https://doi.org/10.1016/j.scitotenv.2009.09.044)
9. E. Y. Yazici, H. Deveci, *Hydrometal.* **139** (2013) 30 (https://doi.org/10.1016/j.hydromet.2013.06.018)
10. L. H. Yamane, V. T. Moraes, D. C. R. Espinosa, J. A. S. Tenorio, *Waste Manage.* **31** (2011) 2553 (https://doi.org/10.1016/j.wasman.2011.07.006)
11. M. Peng, W. Layiding, X. Dong, G. Jiangang, D. Guanghong, *IEEE International Symposium on Electronics and the Environment,* 2004. *Conference Record* (2004) Scottsdale, AZ, pp. 237–242 (https://doi.org/10.1109/ISEE.2004.1299722)
12. Y. Zhao, X. Wen, B. Li, *Min. Metall. Expl.* **21** (2004) 99 (https://doi.org/10.1007/BF03403310)
13. X. Wen, Y. Zhao, C. Duan, X. Zhou, H. Jiao, S. Song, in *Proceedings of the 2005 IEEE International Symposium on Electronics and the Environment*, 2005, New Orleans, LA, 2005, pp. 121–128 (https://doi.org/10.1109/ISEE.2005.1437005)
14. J. Li, H. Lu, J. Guo, Z. Xu, Y. Zhou, *Environ. Sci. Technol.* **41** (2007) 1995 (https://doi.org/10.1021/es0618245)
15. J. Li, Z. Xu, Y. Zhou, *J. Electrostat.* **65** (2007b) 233 (https://doi.org/10.1016/j.elstat.2006.08.004)
16. C. Hagelüken, *Acta Metall. Slovaca* **12** (2006) 111 (https://www.researchgate.net/publication/284043293_Recycling_of_Electronic_Scrap_at_Umicore_Precious_Metals_Refining, accessed 13 March 2024)
17. B. S. Kim, J. Lee, S. P. Seo, Y. K. Park, H. Sohn, *J. Miner. Met. Mater. Soc.* **56** (2004) 55 (https://doi.org/10.1007/s11837-004-0237-9)
18. W. J. Hall, P. T. Williams, *Resour. Conversat. Recycl.* **51** (2007) 691 (https://doi.org/10.1016/j.resconrec.2006.11.010)
19. A. Mecucci, K. Scott, *J. Chem. Technol. Biotechnol*. **77** (2002) 449 (https://doi.org/10.1002/jctb.575)
20. C. J. Oh, D. O. Lee, H. S. Yang, T. J. Ha, M. J. Kim, *J. Air Waste Manage. Assoc.* **53** (2003) 897 (https://doi.org/10.1080/10473289.2003.10466230)
21. P. Quinet, J. Proost, A. Van Lierde, *Miner. Metall. Process.* **22** (2005) 17 (https://doi.org/10.1007/BF03403191)
22. H. Madenoglu, *MSc. Thesis*, Ege University, Institute of Science, Izmir, 2005

23. E. Kim, M. Kim, J. Lee, J. Jeong, B.D. Pandey, *J. Hazard. Mater.* **198** (2011) 206 (https://doi.org/10.1016/j.jhazmat.2011.10.034)
24. M. Jaiswal, S. Srivastava, *J. Hazard. Mat.Adv.* **14** (2024) 100435 (https://doi.org/10.1016/j.hazadv.2024.100435)
25. M. Arshadi, F. Pourhossein, S.M. Mousavi, S. Yaghmaei, *Sep. Purif. Tech.* **272** (2021) 118701 (https://doi.org/10.1016/j.seppur.2021.118701)
26. H. Deveci, E. Y. Yazici, A. D. Bas, in *Proceedings of IMPC 2016: XXVIII International Mineral Processing Congress Proceedings,* ISBN 9781510859388, 2016, p. 5434
27. C, Vallejos-Michea, Y. Barrueto, Y. P. Jimenez, *J. Clean. Prod.* **348** (2022) 131357 (https://doi.org/10.1016/j.jclepro.2022.131357)
28. C.G. Perea, O.J. Restrepo Baena, C.F. Ihle, H. Estay, *Clean. Energy and Tech.* **5** (2021) 100312 (https://doi.org/10.1016/j.clet.2021.100312)
29. R. Montero, A. Guevara, E. De la Torre, in *Proceedings of XXVI International Mineral Processing Congress IMPC 2012*, ISBN: 81-901714-3-7, New Delhi, India, 2012, pp. 3513–3519 (https://www.impc-council.com/IMPC_2012_Proceedings_INDIA.pdf)
30. Ž. Kamberović, M. Korać, D. Ivšić, M. Ranitović, *Metall. J. Metall.* **17** (2011) 139 (https://doi.org/10.30544/382)
31. T. Kinoshita, S. Akita, N. Kobayashi, S. Nii, F. Kawaizumi, K. Takahashi, *Hydrometal.* **69** (2003) 73 (https://doi.org/10.1016/S0304-386X(03)00031-8)
32. I. Birloaga, V. Coman, B. Kopacek, F. Veglio, *Waste Manage.* **34** (2014) 2581 (https://doi.org/10.1016/j.wasman.2014.08.028)
33. H. Deveci, E.Y. Yazıcı, U. Aydın, R. Yazıcı, A.U. Akcil, in *Proceedings of Going Green – Care Innovation conference*, Vienna, Austria, 2010, p. 45
34. J. Ficeriová, P. Baláž, E. Gock, *Acta Montan. Slovaca* **16** (2011) 128 (https://actamont.tuke.sk/pdf/2011/n2/2ficeriova.pdf)
35. M. Kumar, J.-C. Lee, M.-S. Kim, J. Jeong, K. Yoo, *Environ. Eng. Manage. J.* **13** (2014) 2601 (http://www.eemj.icpm.tuiasi.ro/pdfs/vol13/no10/Full/20_601_Kumar_11.pdf)
36. F. P. C. Silvas, M. M. J. Correa, M. P. K. Caldes, V. T. Moraes, D. C. R. Espinosa, J. A. S. Tenorio *Waste Manage*. **46** (2015) 503 (https://doi.org/10.1016/j.wasman.2015.08.030)
37. K.E.H.K. Ishak, S. Ismail, M.I.B.A. Razak, *Mater. Today: Proc.* **66** (2022) 3077 (https://doi.org/10.1016/j.matpr.2022.07.395)
38. S. Anwer, A. Panghal, I. Majid, S. Mallick, *Inter. J. Env. Sci. Tech.* **19** (2022) 9731 (https://doi.org/10.1007/s13762-021-03662-y)
39. Ö. Gök, G. Şen Akar, *J. Serb. Chem. Soc.* **88** (2023) 1039 (https://doi.org/10.2298/JSC230316056G)
40. Y. Huang, S. L. Chou, S. L. Lo, *Sust. Env. Res.* **32** (2022) 6 (https://doi.org/10.1186/s42834-022-00118-x).
41. C. O. Calgaro, D. F. Schlemmer, M. D. C. R. da Silva, E. V. Maziero, E. H. Tanabe, D. A. Bertuol, *Waste Manage.* **46** (2015) 289 (https://doi.org/10.1016/j.wasman.2015.05.017)
42. A. Behnamfard, M. M. Salarirad, F. Veglio, *Waste Manage.* **33** (2013) 2354 (http://doi.org/10.1016/j.wasman.2013.07.017)
43. O. Levenspiel, *Chemical Reaction Engineering*, Wiley, New York, 1972, pp. 357–400
44. N. Mazet, *Int. Chem. Eng.* **32** (1992) 271.

Journal of the Serbian Chemical Society
JSCS-info@shd.org.rs • www.shd.org.rs/JSCS
J. Serb. Chem. Soc. *90* (3) 339–350 (2025)
JSCS–5391
Original scientific paper
Published 24 March, 2025

Coating technology on mortar surface for extending service life of on-site building construction

NIDCHAMON JUMRUS[1,2], MONWIPA THAPINTA[2], PATCHARAPORN CHAIWONG[2], ARISARA PANTAWAN[1,2], TEWASIN KUMPIKA[2], WINAI THONGPAN[3], NIWAT JHUNTAMA[4], EKKAPONG KANTARAK[2], WATTIKON SROILA[2], RATTIYAKORN RIANYOI[2], PISITH SINGJAI[2] and WIRADEJ THONGSUWAN[2]*

[1]Office of Research Administration, Chiang Mai University, Chiang Mai 50200, Thailand, [2]Department of Physics and Materials Science, Faculty of Science, Chiang Mai University, Chiang Mai, 50200, Thailand, [3]Department of Physics, Faculty of Science and Technology, Thammasat University, Lampang, 52190, Thailand and [4]Faculty of Science and Agricultural Technology, Rajamangala University of Technology Lanna, Chiang Mai 50300, Thailand

(Received 17 April, revised 24 May, accepted 25 August 2024)

Abstract: The superhydrophobic, self-cleaning and anti-corrosion surface was successfully coated on mortar using an effective one-step spray coating technique. A coating solution was prepared by mixing methyltrichlorosilane-modified SiO_2/TiO_2 nanoparticles at different ratios to enhance the superhydrophobicity and reduce water absorption of the mortar. The sample prepared using a SiO_2/TiO_2 with the ratio of 75/25 was found to be optimal, exhibiting a high water contact angle and low sliding angle, which resulted in a reduction of water absorption by more than 97.5 % and chloride ion penetration depth. Furthermore, the robustness of the superhydrophobic coating was analyzed against various tests including water drop impact, sand abrasion impact, tape peeling and sandpaper abrasion tests, each test was conducted with over 10000 drops, 300 g, 60 cycles and 5 cycles, respectively. Notably, the coating showed excellent water absorption reduction of 82.6 % after sandpaper abrasion for a length of 200 cm (20 cycles), even though the water contact angle was reduced to 118°. Thus, the fabrication of superhydrophobic mortar surface offers a novel, alternative approach that is simple, efficient, cost-effective and provides multifunction protection surface to increase the service life of on-site building construction with enhanced mechanical durability and anti-corrosion properties.

Keywords: superhydrophobic; methyltrichlorosilane; self-cleaning; mechanical durability; anti-corrosion.

* Corresponding author. E-mail: wiradej.t@cmu.ac.th
https://doi.org/10.2298/JSC240417080J

INTRODUCTION

Mortars are widely used in the construction industry due to their versatility and cost-effectiveness.[1] However, their susceptibility to water and corrosive ions such as Cl^-, SO_4^{2-}, *etc*., leads to the physical and chemical degradation processes.[2] The concrete structure may crack, spall and delaminate and steel bars in the buildings can be affected by chloride corrosion, leading to the strength reduction. Therefore, it is essential to limit water penetration and enhance anti-corrosion properties to improve durability and prolong the service life of building structures.[3]

Surface superhydrophobicity is one of the methods for creating new functional materials with complete waterproof,[4] self-cleaning[5] and anti-corrosion properties.[6] It is well known that a surface is considered superhydrophobic when it exhibits a water contact angle (WCA) greater than 150° and a sliding angle (SA) less than 10°. Artificial superhydrophobic coatings can be achieved by creating hierarchical surface morphology and modifying it with low surface energy materials.[7] Recently, SiO_2 and TiO_2 nanoparticles (NPs) along with various alkyl silanes have been used to create superhydrophobic coatings such as butyltrichlorosilane (BTS), octadecyltrichlorosilane (ODTS) and methyltrichlorosilane (MTCS).[8,9] MTCS is one of the alkyltrichlorosilanes (trichlorosilane head group with a hydrocarbon tail group of variable length) that has the shortest chain lengths and higher reactivity than others. It can facilitate the polycondensation reactions at room temperature.[9,10] In recent years, many researchers have studied bulk composite superhydrophobic cement mortar to extend the service life in construction.[1–3] However, the composites high-cost is due to a lot of starting materials, which may impact the mechanical properties (compressive strength and flexural strength).

This study aims to replace bulk composites with a simple spray coating technique using MTCS-modified SiO_2/TiO_2 NPs on mortar surface. The coating offers the advantage of easy application on-site building construction unaffecting the structure, resulting in time and cost savings. Additionally, it effectively prevents water and corrosive ions from penetrating into the inner spaces of buildings as well as bulk composites. The ratio SiO_2/TiO_2 NPs was optimized to increase surface roughness, reduce surface energy, and enhance water permeability resistance. Furthermore, the superhydrophobic mortar demonstrates excellent self-cleaning, mechanical durability and anti-corrosion properties. This work presents a novel alternative coating methodology for creating durable superhydrophobic on mortar surfaces, instead of the composites superhydrophobic cement mortar.

EXPERIMENTAL

Preparation of superhydrophobic mortar

First, Portland cement (The Siam Public Company Ltd.) was mixed with water at a ratio of 5:1. Then, the mixed mortar was placed into oiled molds (2 cm diameter and 0.6 cm thick).

After that, the mortars were removed from the molds and cured for 7 days before testing. To prepare the superhydrophobic coating, a solution was created by adding 0.8 % of fumed silica (SiO_2, 7 nm, Sigma–Aldrich Pte. Ltd.) and titanium dioxide (TiO_2, 21 nm, Ajax Finechem) with ratios of 0/100, 25/75, 50/50, 75/25 and 100/0 to methyltrichlorosilane (MTCS, 99.5 % purity, Sigma–Aldrich Pte. Ltd.) dissolved in toluene (99.5 % purity, RCI Labscan Ltd.) at a concentration of 2.5 vol. %. The mixture solution was stirred for 1 h and then sprayed onto the mortar surface using a spray coating technique for 15 times. The spray gun was held perpendicular to the surface at a distance of 10 cm under ambient air and atmospheric pressure.

Characterizations

The surface morphology and porosity of samples were analyzed using scanning electron microscopy (SEM, Hitachi TM4000Plus) and ImageJ software. The chemical bonding was analyzed using Fourier-transform infrared spectrometry (FTIR, BurkerTENSOR 27) and X-ray diffraction (XRD, Rigaku Smartlab) on the surface of uncoated and coated samples with the size of 2 cm in diameter and 0.6 cm thick. Water contact angles (WCA) and sliding angles (*SA*) were measured using a pendant drop tensiometer with 3 μL of deionized water. The permeability of water was evaluated by measuring the rate of water absorption by dry specimen mortar in 1 h.

Mechanical durability tests

The mechanical durability of the coating surface was evaluated through water drop impact test, sand abrasion impact test, tape peeling test and sandpaper abrasion test. For the water drop impact test, water droplet of 40 μL was dropped onto the superhydrophobic mortar surface from a height of 10 cm and a tilt angle of 45°. The sand abrasion impact test involved impacting grains of sizes 100–500 μm on the surfaces at a height 40 cm and a tilt angle of 45° with a flow rate of 2.8 m s^{-1}. The tape peeling test was carried out using the method reported in ASTM D3359-09.[11] The coating mortar surface was pressed with 3M tape under a pressure of 3 kPa to ensure good contact between the surface and the 3M tape. Then, the tape was peeled off from the surface and the above process was repeated. The sandpaper abrasion test was performed on the superhydrophobic mortar surface using sandpaper grit No. 600 as the abrasion surface. The sample was moved in one direction for 10 cm at a speed of 5 mm s^{-1} with a load of 100 g. The WCAs after mechanical durability tests were then investigated.

Chloride permeability test

The mortar samples were covered by epoxy resin (World Chemical Far East Company Ltd.) except for the diffusion surface. Then, the samples were soaked in a 7 wt. % NaCl (Labscan Asia Co., Ltd.) solution for 14 days. After that, a 0.1 mol/L silver nitrate ($AgNO_3$, RCI Labscan Ltd.) solution was sprayed on the cut surface.[3] The depth of chloride ion penetration was measured using the $AgNO_3$ color development test.

RESULTS AND DISCUSSION

Morphology analysis

The morphology of ordinary mortar (OM) and mortars coated with MTCS-modified SiO_2/TiO_2 nanoparticles (NPs) after 15 spraying times were analyzed in detail, using SEM. Fig. 1a shows the hydration products with rough and highly porous surface of the mortar (19.2 %). After spraying, the MTCS-modified SiO_2/TiO_2 coating covered the pore structure of the mortar, as shown in Fig. 1b–f.

From the figure, the porosity of the coated surface (which was measured using ImageJ)[12] decreased to 10.2, 8.5, 6.9, 8.6 and 6.1 %, respectively. The surface of the MTCS-modified TiO_2 (0/100) coating consisted of large, loose agglomerates of TiO_2 (Fig. 1b) while the MTCS-modified SiO_2 (100/0) coating surface was densely packed (Fig. 1f). The size of TiO_2 particles approximately three times larger than that of SiO_2 particles, resulting in a dense and low-porosity SiO_2 film. However, superhydrophobic surface requires a hierarchical surface with mono--scale roughness, which was observed in the SiO_2/TiO_2 ratios of 25/75 and 75/25 (Fig 1c and e).

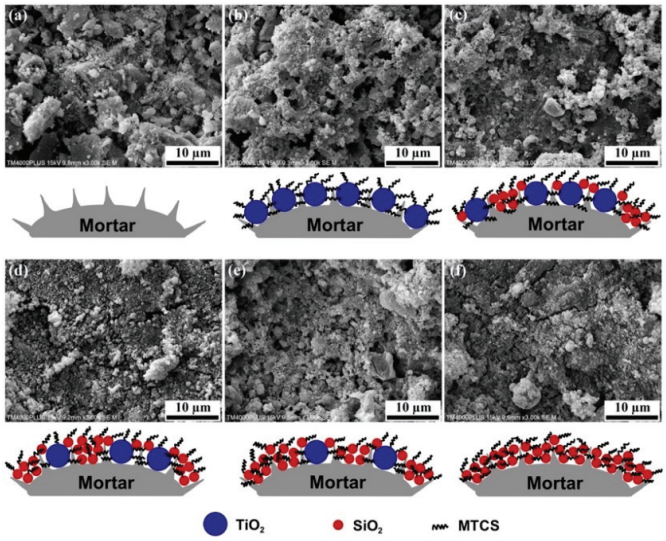

Fig. 1. Surface morphologies and schematic diagram of: a) ordinary mortar and the coated mortar by MTCS-modified SiO_2/TiO_2 NPs in ratios of b) 0/100, c) 25/75, d) 50/50, e) 75/25 and f) 100/0.

Wettability analysis

Fig. 2 shows water contact angle (WCA) of OM and coated mortar. The OM exhibited hydrophilicity with a WCA of 55.2°. After coating with MTCS-modified SiO_2/TiO_2 at different ratios using 15 spray applications, the mortar surfaces transformed into hydrophobic and superhydrophobic surfaces, with WCAs of 149.3, 145.6, 154.1, 154.7 and 145.7°, respectively. Interestingly, the samples coated at SiO_2/TiO_2 ratios of 50/50 and 75/25 displayed superhydrophobic mortar with WCA greater than 150° and SA less than 2°. Therefore, the hierarchical structure and low surface energy of the coated mortar surface contributed to the superhydrophobic behavior. This wetting behavior can be explained by the Cassie–Baxter equation:[13]

$$\cos\theta_\gamma = f_1\cos\theta - f_2 = f_1(\cos\theta + 1) - 1 \quad (1)$$

where θ_γ is the contact angle of the coated mortar surface, θ is the contact angle of the ordinary mortar surface (55.2°), f_1 is the solid fraction between the coated mortar and the droplet, f_2 is the air fraction between the coated mortar and the droplet. The solid fraction (f_1) and air fraction (f_2) of coated mortars are presented in Table I. The results imply that the ratio of SiO_2/TiO_2 increases air pockets in the rough structure, forming a solid-gas composition interface. Moreover, the smaller contact area between the droplet and coated mortar surface trends to increase the superhydrophobicity.

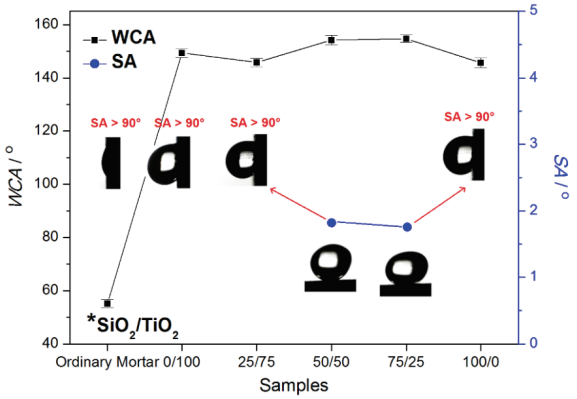

Fig. 2. Water contact angles and sliding angles of samples.

TABLE I. Solid fraction, air fraction and water permeability of ordinary and coated mortars

Sample	Solid fraction (f_1)	Air fraction (f_2)	Coefficient of water absorption, 10^{-9} cm^2 s^{-1}	Reduction in the coefficient of water absorption, %
OM	–	–	700	–
0/100	0.089	0.911	36.1	94.8
25/75	0.110	0.890	57.4	91.8
50/50	0.064	0.936	29.0	95.9
75/25 (SM)	0.061	0.939	17.7	97.5
100/0	0.111	0.889	74.5	89.4

Furthermore, water permeability property was measured by the coefficient of water absorption, as shown in Table I. The coefficient of water absorption value was calculated by the equation:[14]

$$K_a = (\frac{Q}{A})\frac{1}{t} \quad (2)$$

where K_a is the coefficient of water absorption, cm^2 s^{-1}; Q is the quantity of water absorbed by the sample, cm^3, in time, t / s and A is the total surface area of the sample, cm^2. For the OM, the coefficient of water absorption was measured

to be 700×10^{-9} cm^2 s^{-1}. After spraying, the coefficient of water absorption of all samples decreases by over 88 % compared to OM, indicating that the coating layer prevented water absorption into the pore structure of the mortar. Interestingly, the samples coated with MTCS-modified SiO_2/TiO_2 at a ratio of 75/25 exhibited the highest water resistance with a 97.5 % which reduced the coefficient of water absorption. This is because the appropriate combination between SiO_2 and TiO_2 increase the nano-scale roughness on the surfaces (see Fig. 1e) as well as the highest air fraction (see Table I). Air pockets between the water drops and surface prevent water absorption into the mortar surface, following the Cassie–Baxter model.[4] Therefore, MTCS-modified SiO_2/TiO_2 in a ratio of 75/25 is considered to have sufficient potential for practical applications due to hierarchical surface, high WCA and low water resistance, representing an optimum superhydrophobic mortar (SM) in this study. This result indicates that the coating of MTCS-modified SiO_2/TiO_2 NPs created a protective barrier on the mortar surface which improved the superhydrophobicity and effectively prevented the infiltration of water entering the mortar and causing damage. Therefore, this property is closely connected to the durability of mortar in outdoor environments, suggesting that the superhydrophobic coating can improve the service life and performance of the mortar in practical applications.

Chemical composition analysis

Fig. 3a displays the FTIR transmission spectra of ordinary mortar (OM) and superhydrophobic mortar (SM) with wavenumbers ranging from 4000 to 400 cm^{-1}. The absorption bands of OM at 435 cm^{-1} correspond to Si–O.[5] Peaks at 1400, 872 and 710 cm^{-1} are attributed to the C–O bond due to the presence of calcite in mortar.[15,16] The peaks at 1800–2300 cm^{-1} were observed in mortar.[17] The peak at 3643 cm^{-1} corresponds to the O–H vibration of portlandite ($Ca(OH)_2$).[5] After modification, the absorption band at 2970 cm^{-1} was attributed to the C–H bond in the $–CH_3$ group. Additionally, the peak 1271 cm^{-1} corresponded to the bending vibration of $Si–CH_3$, indicating successful MTCS modification and surface energy reduction.[18] In addition, the peaks at 1026 and 767 cm^{-1} belong to Si–O–Si,[5] which are consistent with the functional groups in the MTCS structure, forming a self-assembled film. TiO_2 NPs are approximately three times larger in diameter compared to SiO_2 nanoparticles while the specific surface area is less than SiO_2 NPs. Thus, the appropriate combination between SiO_2 and TiO_2 can increase specific surface area, leading to increase –OH groups. The superhydrophobic modification mechanism involved MTCS reacting with the –OH groups of SiO_2 and TiO_2 NPs through hydrolysis and condensation reactions, leading to the grafting of alkoxy groups of MTCS on the SiO_2 and TiO_2 surfaces.[4] Then, MTCS-modified SiO_2/TiO_2 NPs absorbed onto the mortar surface and filled lager pores of hydration products. Thus, the SiO_2/TiO_2 NPs reacted with MTCS

to reduce the surface energy and improve the surface roughness on mortar. The peaks at 1800–2300 cm^{-1} in SM were of very low intensity, indicating that the mortar surface is covered with a low surface energy coating. In Fig. 3b, the XRD pattern of OM and SM is presented. The main components of mortar are the same, namely calcite, quartz, portlandite, calcium silicate hydrate, alite and belite.[19] After coating, the SM shows lower intensity peaks of mortar, while significant peaks of SiO_2 and TiO_2 appeared.[20,21]

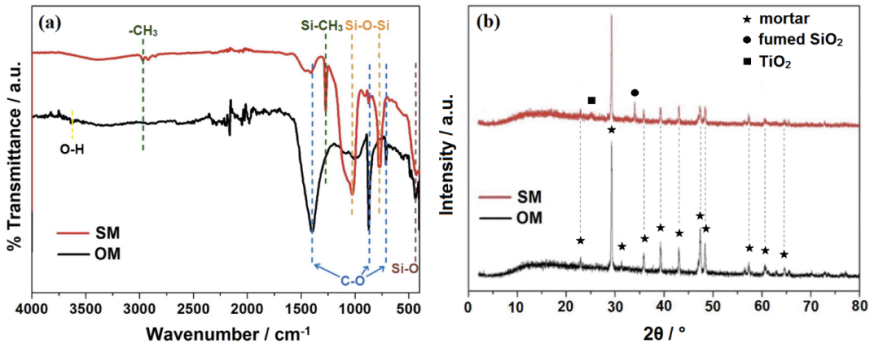

Fig. 3. a) The FTIR spectra and b) X-ray diffraction patterns of ordinary mortar (OM) and superhydrophobic mortar (SM).

Self-cleaning and mechanical durability properties

It is well known that outdoor mortar is easy to face with dust particles over time. The cumulation of pollutants for a long time will have a negative impact on the performance of mortars. The self-cleaning property of the OM and SM was tested using sand as a contaminator, as shown in Fig. 4a and b. In the SM, water droplets bead up into spheres and leave no residual droplets on the surface. This result indicated that the MTCS-modified SiO_2/TiO_2 NPs form a film on the mortar, exhibiting negligible water adhesion. Fig. 4c shows the mechanism of self-cleaning of the SM. While the water drop is rolling, it collects dust particles, demonstrating excellent self-cleaning property. In the Cassie–Baxter state, the droplet rests on top of the surface features, suspended by air pockets between the liquid droplet and the MTCS-modified SiO_2/TiO_2 NPs surfaces. These air pockets reduce the contract area, generating a greater net force and prevent the droplet from penetrating into the mortar surface.[22]

While the self-cleaning property of SM is promising, one of the major problems of superhydrophobic coatings is their poor mechanical durability. Therefore, the mechanical durability of SM was evaluated using water drop impact test, sand abrasion impact test, tape peeling test and sandpaper abrasion test, as shown in Fig. 5a–d and Table II. In the water drop impact test, the WCA of SM decreased to less than 150° after impinging of 10000 water droplets. Additionally,

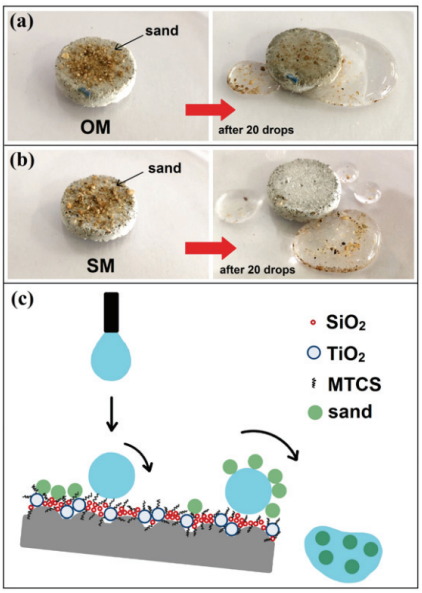

Fig. 4. The self-cleaning test of: a) ordinary mortar, b) superhydrophobic mortar and c) mechanism diagram of self-cleaning.

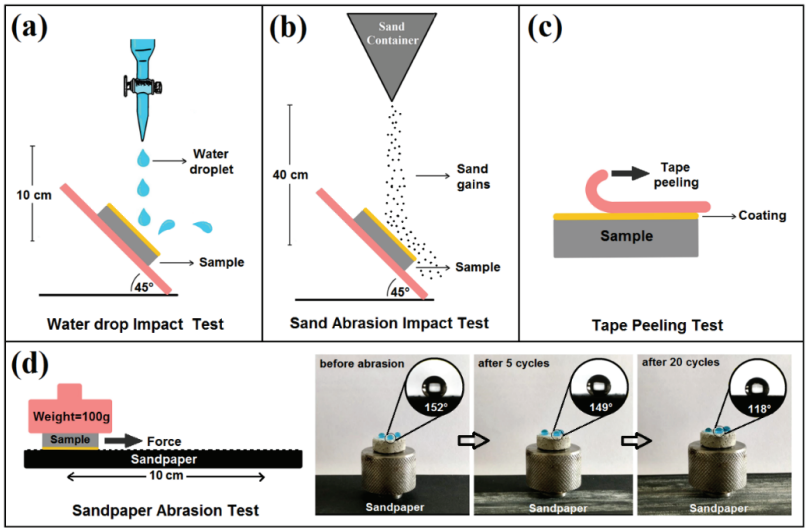

Fig. 5. Schematic of mechanical durability tests: a) water drop impact test, b) sand abrasion impact test, c) tape peeling test and d) sandpaper abrasion test on superhydrophobic mortar.

the sand abrasion impact test was also performed to investigate the durability of the superhydrophobic coating to simulate the impact of dust particles. The SM lost its superhydrophobicity after impingement with 300 g of sand gains. Moreover, the superhydrophobicity of the SM surface was retained even after 60

cycles in the tape peeling test. Fig. 5d shows the sandpaper abrasion test on the SM. Before abrasion, water drops were placed on the SM surface with a WCA of ~152°. After 5 cycles of abrasion, the superhydrophobicity of SM was only slightly reduced. The superhydrophobic coating was robust after dragging nearly 50 cm on the sandpaper, which shows high durability compared to the same experiment set up in the other research.[8] However, the coating surface was severely abraded after 20 cycles (200 cm in length) of abrasion, resulting in a dramatic decrease in WCA to ~118°. Interestingly, the abraded mortar exhibited a significant reduction in water absorption, approximately 82.6 %, compared to OM. These results confirmed the robust superhydrophobic mortar despite the coating being applied only on the surface, which allowed the coating to be used in practical applications on a large-scale.

TABLE II. Mechanical durability tests of superhydrophobic mortar

Water drop impact test		Sand abrasion impact test		Tape peeling test		Sandpaper abrasion test	
Number of drops	WCA / °	Sand gain g	*WCA* / °	Number of cycles	*WCA* / °	Number of cycles	*WCA* / °
0	154±1	0	154±1	0	154±1	0	154±1
10000	149±2	100	151±2	30	150±2	5	149±3
20000	145±1	200	150±3	60	149±2	10	135±4
30000	123±2	300	149±3	90	141±4	15	131±6
40000	115±2	400	140±4	120	131±4	20	118±5

Anti-corrosion analysis

Fig. 6 shows the depth of chloride ion penetration in OM and SM after immersion in NaCl solution for 14 days and subsequent spraying with $AgNO_3$ solution. In the $AgNO_3$ color development test, chloride permeated regions turn violet due to AgCl precipitation, while regions without chloride penetration turn brown due to the formation of Ag_2O.[3,23] The chemical reactions of the $AgNO_3$ color development test are shown in Eqs. (3) and (4):[3]

$$AgNO_3 + NaCl \rightarrow AgCl + NaNO_3 \quad (3)$$

$$2AgNO_3 + 2NaOH \rightarrow Ag_2O + 2NaNO_3 + H_2O \quad (4)$$

The violet regions are affected by the concentration of $AgNO_3$ solution, pH, types of cement and the chloride content of cement.[24] The SM exhibited excellent corrosion resistance, with an average depth of chloride ion penetration of about 1.6 mm (Fig. 6b), while chloride ions were able to penetrate most of the OM (Fig. 6a). Thus, the superhydrophobic coating demonstrated as a good barrier for corrosion and prevents external chloride ions, which are confirmed by the EDS results. The anti-corrosion mortar effectively blocks the diffusion of chloride ions inside the building and might prevent it from reaching the steel inside

the building in chloride salt environments. It was found that the coating method improves the anti-corrosion property of mortar, acting as a protective barrier with effective performance in outdoor and marine environments. The superhydrophobic and anti-corrosion properties prevent water or corrosive ions from entering the mortar, slowing down the corrosion of steel inside the structures and enhancing the durability and service life of construction buildings. Therefore, the fabrication of superhydrophobic mortar can facilitate its durable application in outdoor and marine environments and has the potential as a superhydrophobic coating for various substrates.

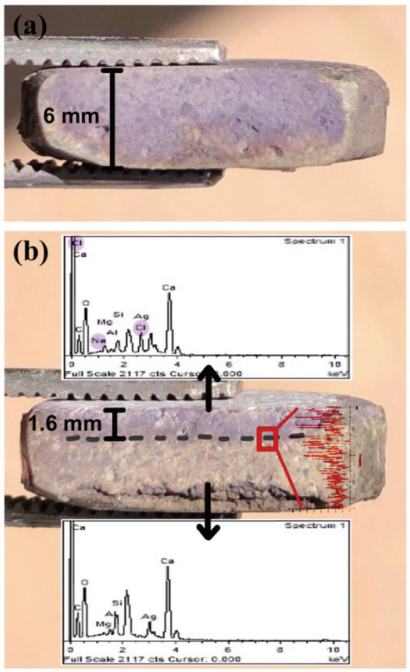

Fig. 6. The chloride ions diffusion of: a) ordinary mortar and b) superhydrophobic mortar obtained by silver nitrate color experiment.

CONCLUSION

In conclusion, the MTCS-modified SiO_2/TiO_2 nanoparticle-coated mortar demonstrates a superhydrophobic surface using a simple spray coating method. A sample coated with a SiO_2/TiO_2 ratio of 75/25 with 15 spraying times exhibits the highest water contact angle and the lowest water absorption with a hierarchical structure. Furthermore, the water absorption of the superhydrophobic mortar was reduced by 97.5 %, indicating excellent waterproofing ability, despite the coating being applied only to the surface. The coated mortars maintained their unique wettability after being impacted with water drop, sand, tape peeling and abraded with sandpaper, demonstrating excellent robustness due to their good mechanical durability properties. Even after being abraded with sandpaper for 20

cycles, the water absorption was reduced by 86.2 %. Moreover, the fabricated superhydrophobic mortar exhibited excellent self-cleaning and anti-corrosion property, effectively reducing chloride ion penetration. Therefore, the simple, cost-effective coating process is suitable for various applications in on-site building construction. In the future, the superhydrophobic coating can be applied to other material surfaces such as wood, metal and plastic to extend their service life.

Acknowledgements. This work was supported by postdoctoral fellowship from the Office of Research Administration, Chiang Mai University, Chiang Mai and The Science Achievement Scholarship of Thailand.

ИЗВОД

ТЕХНОЛОГИЈА НАНОШЕЊА ПРЕВЛАКА НА ПОВРШИНУ МАЛТЕРА ЗА ПРОДУЖЕЊЕ РАДНОГ ВЕКА ГРАЂЕВИНСКИХ КОНСТРУКЦИЈА

NIDCHAMON JUMRUS[1,2], MONWIPA THAPINTA[2], PATCHARAPORN CHAIWONG[2], ARISARA PANTAWAN[1,2], TEWASIN KUMPIKA[2], WINAI THONGPAN[3], NIWAT JHUNTAMA[4], EKKAPONG KANTARAK[2], WATTIKON SROILA[2], RATTIYAKORN RIANYOI[2], PISITH SINGJAI[2] и WIRADEJ THONGSUWAN[2]

[1]Office of Research Administration, Chiang Mai University, Chiang Mai 50200, Thailand, [2]Department of Physics and Materials Science, Faculty of Science, Chiang Mai University, Chiang Mai, 50200, Thailand, [3]Department of Physics, Faculty of Science and Technology, Thammasat University, Lampang, 52190, Thailand и [4]Faculty of Science and Agricultural Technology, Rajamangala University of Technology Lanna, Chiang Mai 50300, Thailand

Суперхидрофобна, самочистећа и антикорозиона превлака је успешно нанета на малтер коришћењем технике једностепеног распршивања. У раствор за распршивање су додате, у различитим односима, наночестице SiO_2 и TiO_2 модификоване метилтрихлоросиланом да би се повећала суперхидрофобност малтера и смањила апсорпција воде. Узорак припремљен при масеном односу SiO_2/TiO_2 = 75/25 је показао највећи контактни угао и најмањи угао клизања, што је обезбедило смањење апсорпције воде веће од 97,5 % и смањење дубине продирања хлоридних јона. Постојаност превлаке је анаизирана различитим тестовима, укључујући утицај падајућих капи воде (10000 капи), абразију песком (300 g), одлепљивање помоћу траке (60 циклуса) и абразију шмиргл папиром (5 циклуса). Превлака је показала одлично смањење апсорпције воде и после теста абразије шмиргл папиром током 20 циклуса (82,6 %), иако је контактни угао смањен на 118°. Приказани резултати указују да формирање суперхидрофобне превлаке на малтеру представља алтернативни приступ, који је једноставан, ефикасан и економичан, за обезбеђење мултифункционалне заштите површине малтера на лицу места у циљу продужења радног века конструкција са побољшаним механичким и антикорозионим својствима.

(Примљено 17. април, ревидирано 24. маја, прихваћено 25. августа 2024)

REFERENCES

1. W. Wang, S. Wang, D. Yao, X. Wang, X. Yu, Y. Zhang, *Constr. Build. Mater*. **238** (2020) 117626 (https://doi.org/10.1016/j.conbuildmat.2019.117626)
2. T. Xiang, J. Liu, Z. Lv, F. Wei, Q. Liu, Y. Zhang, H. Ren, S. Zhou, D. Chen, *Constr. Build. Mater*. **313** (2021) 125482 (https://doi.org/10.1016/j.conbuildmat.2021.125482)
3. L. Qu, Q. Wang, J. Mao, S. Xu, H. Zhang, Z. Shi, X. Li, *Constr. Build. Mater*. **313** (2021) 125540 (https://doi.org/10.1016/j.conbuildmat.2021.125540)

4. N. Jumrus, T. Chaisen, A. Sriboonruang, A. Panthawan, T. Kumpika, E. Kantarak, P. Singjai, W. Thongsuwan, *Mater. Lett.* **264** (2020) 127347 (https://doi.org/10.1016/j.matlet.2020.127347)
5. N. Jumrus, J. Jompaeng, A. Panthawan, T. Kumpika, O. Wiranwetchayan, P. Sanmuangmoon, W. Sroila, E. Kantarak, P. Singjai, W. Thongsuwan, *Mater. Lett*. **304** (2021) 130618 (https://doi.org/10.1016/j.matlet.2021.130618)
6. F. Jiang, T. Zhu, Y. Kuang, H. Wu, S. Li, *Chem. Phys. Lett*. **811** (2023) 140197 (https://doi.org/10.1016/j.cplett.2022.140197)
7. N. Jumrus, N. Suttanon, W. Sroila, P. Tippo, A. Panthawan, W. Thongpan, T. Kumpika, W. Sroila, R. Rianyoi, P. Singjai, W. Thongsuwan, *Mater. Lett*. **330** (2023) 133342 (https://doi.org/10.1016/j.matlet.2022.133342)
8. R. S. Sutar, S. D. Manadeshi, S. S. Latthe, S. R. Kulal, G. D. Salunkhe, K. K. Rangar, R. A. Lavate, S. B. Raut, A. C. Sapkal, A. K. Bhosale, K. K. Sadasivuni, S. Liu, R. Xing, *Macromol. Symp. Spec. Issue:Adv. Mat. Sc. — ICAMS 2020 (Part II)* **393** (2020) 2000033 (http://dx.doi.org/10.1002/masy.202000033)
9. A. Sriboonrung, T. Kumpika, E. Kantarak, W. Sroila, P. Singjai, N. Lawan, S. Muangpil, W. Thongsuwan, *Chiang Mai J. Sci*. **47** (2020) 823-828 (https://epg.science.cmu.ac.th/ejournal/journal-detail.php?id=11108)
10. E. G. Atici, E. Kasapgil, I. Anac, H. Y. Erbil, *Thin Solid Films* **616** (2016) 101 (https://doi.org/10.1016/j.tsf.2016.07.041)
11. K. Pacaphol, D. Aht-Ong, *Surf. Coat. Technol*. **320** (2017) 70 (https://doi.org/10.1016/j.surfcoat.2017.01.111)
12. A. Yu, K.L. Yick, S.P. Ng, J. Yip, Y.F. Chan, *Burns* **46** (2020) 1548 (https://doi.org/10.1016/j.burns.2020.04.014)
13. Z. Yin, M. Xue, Y. Ji, Z. Hong, C. Xie, *Chem. Phys. Lett*. **754** (2020) 137694 (https://doi.org/10.1016/j.cplett.2020.137694)
14. K. Ganesan, K. Rajagopal, K. Thangavel, *Cem. Concr. Compos*. **29** (2007) 515 (https://doi.org/10.1016/j.cemconcomp.2007.03.001)
15. H. Kang, S. Kang, B. Lee, *Materials* **14** (2021) 5407 (https://doi.org/10.3390/ma14185407)
16. C. Yao, A. Xie, Y. Shen, J. Zhu, T. Li, *J. Chil. Chem. Soc*. **58** (2013) 2235 (http://dx.doi.org/10.4067/S0717-97072013000400072)
17. G. Richhariya, D. T. K. Dora, K. R. Parmar, K. K. Pant, N. Singhal, K. Lal, P. P. Kundu, *Materials* **13** (2020) 2921 (https://doi.org/10.3390/ma13132921)
18. J. Wan, L.H. Xu, H. Pan, L.M. Wang, Y. Shen, *J. Porous Mater*. **28** (2021) 1501 (http://dx.doi.org/10.1007/s10934-021-01089-x)
19. G. Semugaza, T. Mielke, M. E. Castillo, A. Gierth, J. X. Tam, S. Nawrath, D. Lupascu, *Mater. Struct.* **56** (2023) 48 (http://dx.doi.org/10.1617/s11527-023-02133-9)
20. R. G. Toro, M. Diab, T. Caro, M. Al-Shemy, A. Adel, D. Caschera, *Materials* **13** (2020) 1326 (https://doi.org/10.3390/ma13061326)
21. J. Li, X. L. Wu, D. S. Hu, Y. M. Yang, T. Qiu, J. C . Shen, *Solid State Commun*. **131** (2004) 21–25 (https://doi.org/10.1016/j.ssc.2004.04.026)
22. Y. Wu, K. Yan, G. Xu, C. Yang, D. Wang, *Prog. Org. Coat.* **159** (2021) 106411 (https://doi.org/10.1016/j.porgcoat.2021.106411)
23. A. R. A. Javier, N. E. Lopez, J. B. P. Juanzon, *Procedia Eng*. **171** (2017) 543 (http://dx.doi.org/10.1016/j.proeng.2017.01.369)
24. L. V. Real, D. R. B. Oliveira, T. Soares, M. H. F. de Medeiros, *Revista ALCONPAT* **5** (2015) 141 (https://dx.doi.org/10.21041/ra.v5i2.84).

Journal of the Serbian Chemical Society
JSCS-info@shd.org.rs • www.shd.org.rs/JSCS
J. Serb. Chem. Soc. *90* (3) 351–367 (2025)
JSCS–5392
Original scientific paper
Published 24 March, 2025

Corrosion studies, parameter effects, and surface morphology of AA5052-AA6101T6 friction stir welded joints

SATHISH RENGARAJAN[1], G. KASIRAJAN[2]* and R. ASHOK KUMAR[3]

[1]Department of Mechanical Engineering, St. Joseph's College of Engineering, Semmancheri, Chennai, Tamil Nadu-600119, India, [2]Research Scholar, Department of Mechanical Engineering, St. Joseph's College of Engineering, Semmancheri, Chennai, Tamil Nadu--600119, India and [3]Department of Mechanical Engineering, SRM Madurai College for Engineering and Technology, Nedungulam Main Rd, Pottapalayam, Tamil Nadu-630611, India

(Received 17 April, revised 19 May, accepted 24 August 2024)

Abstract: Traditional fusion welding is unsuitable for welding aluminum alloys because secondary brittle phases, porosity, and cracks are likely to form as the alloy solidifies. Friction stir welding (FRSTW), a new solid-state welding method, can join similar or dissimilar aluminium (ALU) alloys. In this study friction stir welded AA5052-AA6101T6 alloy samples were tested for corrosion characteristics. The microstructure and mechanical behavior of FRSW--welded AA5052-AA6101T6 ALU alloy joints were examined relative to input parameters. Microstructure reveals that welding speed and rotation-speed affect the weld microstructure analyzed sample welded areas. Twenty-nine samples were corrosion tested in 3.5 % NaCl, household water (880 ppm – SPM), 1 M H_2SO_4, 1 M NaOH and natural seawater for 72 h. Domestic salt water and acid medium showed better resistance to corrosion than alkaline and salt media. Impedance studies demonstrated slight anodic and cathodic potential changes after friction stir welding.

Keywords: microstructure; aluminum alloys; impedance study; weight loss method.

INTRODUCTION

Aluminum (ALU) alloys are more thermally stable than steel and can withstand temperatures between 480–660 °C before melting. Aluminum has corrosion resistance properties high strength-to-weight ratios, and excellent thermal and electric conductivity in maritime conditions. Also, it provides good characteristics such as lightweight, machinability, non-magnetic, formability and ductility are some of the qualities of this material.[1] Fabrication of weldments can be done by using either pressure or non-pressure welding techniques, depending on the

* Corresponding author. E-mail: gurukasirajan@gmail.com
https://doi.org/10.2298/JSC240417078R

technology employed. Generally, ALU alloys provide a protective oxide layer during the joining process due to this protection these alloys were used in several applications like vehicles, marine applications and overhead transmission lines.[2] One of the solid-state joining processes called friction stir welding (FRSTW) was developed quite a while ago. Subsequently, it has been demonstrated as a successful technique for joining chemically dissimilar aluminum alloys compositional compatibility is not an issue, unlike in fusion welding and any aluminum alloy can be welded.[3–7] At low energy, FRSTW exhibited numerous mechanical benefits, including superior dimensional stability, repeatability, absence of alloying loss and fine microstructure at the joints.[8] Dynamic recrystallization produces a fine grain structure in the weld region's center, which affects the joint strength. Corrosion resistance is an inherent property of aluminum; nevertheless, the thickness can vary due to internal and external factors. When compared to the various metal welding techniques, aluminum welding is used to make a longer design because aluminum is more resistant to corrosion than steel. The breakdown of materials, most often metals, caused by chemical reactions with the environment, leading to a component’s functional failure, is known as corrosion. Environmental concentration, stress, erosion and temperature are the four variables that determine corrosion, a form of reverse extractive metallurgy. Huge yearly economic losses from 1 to 5 % of GNP are caused by it for all nations. Hence, the materials and their corrosion behaviour in different atmospheres are receiving research interest.[38] Also, the corrosion studies on FRSTW aluminium samples have stated the importance of corrosion studies on the welded samples for mechanical applications.[9–13] The reported work stated that the polarization resistance and potential voltage were both low when the CR of the base material welded zones of the metals such as AA5083 and AA7023 were immersed in an artificial NaCl solution. The disparity in volta potential readings led to a higher current density in the AA7023 base material and a strongly attacked border between the two materials.[14] Most of the researchers have reported the FRSTW parameters and the procedures of five, six and seven series of ALU alloys with its characterization.[39] In addition to the weight reductions already mentioned, the corrosion resistances offered by the passive aluminum oxide layer are still another major perk of switching from steel to aluminum components. This research identified the research gap of the distinct alloys such as AA5052 and AA6101-T6 stir welded joints tensile strength and corrosion behavior in a different corrosive medium such as acid, alkali, 1 M salt solution, domestic water, and natural seawater to know the mechanical suitability. Present work also investigated the parameters effect of FRST welded test samples between AA5052 and AA6101-T6 using microstructure analysis. Followed by the sample’s tensile strength, corrosion resistivity in different environments is analyzed for the mechanical applications purpose.

EXPERIMENTAL

Materials and methods

The samples AA5052 and AA6101-T6, which were friction stir welded, were made according to the methods described in earlier research.[15] Friction stir butt welding was performed on AA5052 and AA6101-T6, 6 mm thick using an FRSTW machine depicted in Fig. 1a–c. The shoulder pin length is 5.7 mm with a hexagonal shape of 2.5 mm on 6 six sides the geometrical dimension and welded samples are shown in Fig. 1d and e. Twenty-nine experiments were carried out based on Four process parameters with three levels using response surface methodology.

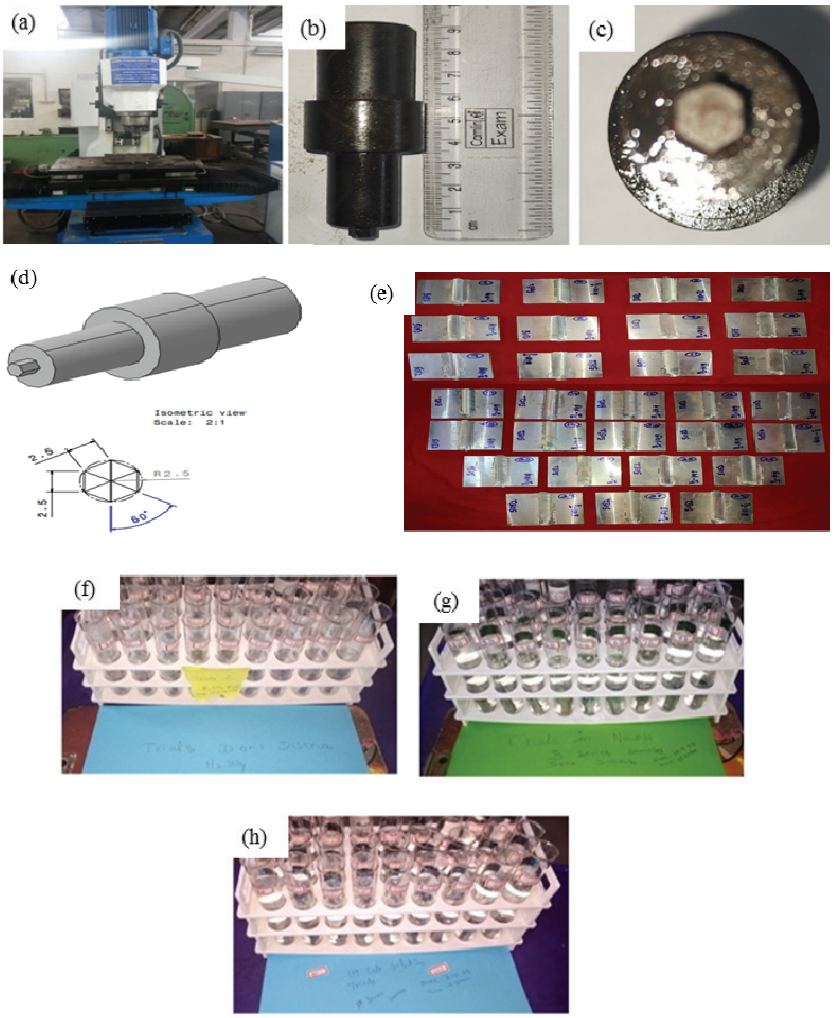

Fig. 1. a) Welding machine, b) spindle tool dimension, c) ALU spinner of FRSTW process, d) pin profile dimension, e) welded samples prepared FRSTW test samples in: f) 1 M H_2SO_4, g) 1M NaOH and h) 1 M salt solution for weight loss investigation.

The dissimilar plates are clamped on two sides, the rotating tool is made to contact till its shoulder, now the tool traverse takes place the materials reach its localized heating, a plastic deformation takes place at the interface of the material, and mechanical pressure is applied to make the weld joint. The tensile test was taken in UTM with 5-ton capacity with Fuel Instruments and engineers with a digital encoder. For microstructural studies metallurgical microscope is an inverted trinocular metallurgical microscope with 50–80× magnification, with paired eye pieces which have 12 V with a polarizer prism. The microscope is attached to a 5 MP camera. The selected test samples welded joints nature is investigated by XRD technique.[16,17] XRD patterns between 2θ 10–80.48 were recorded under continuous scan mode in Bruker-binary V4 (RAW) model at 25 °C with Cu as anode material and the fixed generator settings of 30 mA, 40 kV, respectively. X-Ray diffraction (XRD) test was conducted at 3 kW power with a focus size of 0.4 mm×12 mm Cu anode; the system should also be able to work with other X-ray sources like Mo, Co, Fe or Cr.

The natural salt corrosive medium seawater was collected near the Chennai port, Tamil Nadu, India, and used as such for the corrosion studies. Similarly, domestic fresh water collected from Karasangal, Kancheepuram District, Chennai, Tamil Nadu, India. Both natural mediums were used for the corrosion test in boiling tube.

The welding plate samples were degreased in acetone before being alkaline imprinted in 7.5 wt. % NaOH at 55–60 °C for 5 min. Following this, they were rinsed with distilled water in preparation for corrosion testing. The samples were then subjected to acidification in different prepared corrosion solutions such as 1 M of sodium hydroxide solution (40 g in 1000 mL of distilled water), 1 M H_2SO_4 (28 mL of 37.5 % in 1 L), 1 M commercial sodium chloride crystals solution, domestic hard water (*SPM* = 880 ppm) and marine water.[18,19] The cleaned test specimens were immersed in prepared and collected corrosive medium for 72 h (3 days). After that the welded samples were dried in sunlight and hot air drier for 5 min. Then, the samples were weighed in digital weighing balance. The trials conducted in various corrosive medium are presented in Fig. 1f. From the weight loss data**,** average weight loss was calculated and used for the corrosion rate measurement.

The observed weight losses were recorded and the average weight loss in each corrosive medium was calculated. Using average weight loss corrosion rate was calculated using the following formula (1):

$$R = \frac{534 \times WL}{\rho A t} \tag{1}$$

where R is corrosion rate in mpy, WL is weight loss in g, ρ is density of the metal, g/cm^3, A is surface area in in^2, and t is time in h.

The design surface area is calculated using the formula 2*lb*:

$$\text{Total surface area} = 2(1\times3 + 1.5\times0.5) + 0.5\times3 = 2(3+0.75) + 1.5 = 9 \text{ cm}^2 \tag{2}$$

Potentiometric study

FRSTW test samples were evaluated using a conventional calomel electrode to detect anodic behavior and its impact. This study also tested a galvanic cell with the same calomel electrode in a corrosive artificial 3.5 % salt solution and found higher weight loss. The EIS describes electrolyte resistance, adsorption, diffusion, charge transfer resistance, double-layer capacitance and unique phase processes and features. After surface improvement with emery papers, the trial samples' corrosion behavior was examined using the well-known EIS method. A working electrode (WE) was submerged in a corrosive salt medium after washing the sur-

face in a polar solvent mixture of water and acetone. A saturated calomel electrode (SCE) recorded anodic and corrosion behavior. The corrosion rate was tested in hydrochloric acid. After setting the surface area to 1 cm^2, density to 2.71 g/cm^3, open circuit potential to –0.72839 V, and reference potential to 0.241 V at 25 °C, potentiodynamic data were recorded. The Tafel plot was plotted and the corrosion rate was calculated using the I_{corr} value.

RESULTS AND DISCUSSION

Tensile test

The welded samples were polished well and designed for tensile tests like the dog bone model based on ASTM standards. The specimen (Fig. 2a and b) was tested using forces up to the model breakage. The outcomes of the test samples revealed low to higher tensile strength values. Out of 29 samples, sample 13 showed lower tensile strength of 92 MPa. Likely, sample 26 exposed higher tensile strength (137 MPa). From Table I, a moderate value of 112 MPa was observed for sample 4. The tensile strength results were analyzed along with welded parameters. The selected specimen number 9 (1200 rpm and 7 kN) exposed somehow better strength for a single pass. At the same time, the tensile strength increased with increasing traverse speed and axial load which exhibited the tensile strength of 94 MPa. The applied parameters and their outcomes are presented in Table I. Sample 13 exposed low tensile strength due to higher rpm with a single pass. The results showed that the number of passes affect the material mechanical property which includes tensile strength but the remaining parameters must be optimized for the future design. Next, this work analyzed the rpm with tensile strength. A higher rpm of 1400 with the axial load 7 kN exhibited a tensile strength of 124 MPa. When compared with the 8 kN double pass sample, the triple pass showed good tensile strength. The tensile strength of the sample's rpm has followed the increasing order as follows: sample 7 (80, 7, 1400, 3, 124) > sample 8 (80, 7, 1000, 3, 130) > sample 26 (80, 6, 1200, 3, 137). From the results, this work observed that the optimized rpm is 1200, force, 6–7 kN,

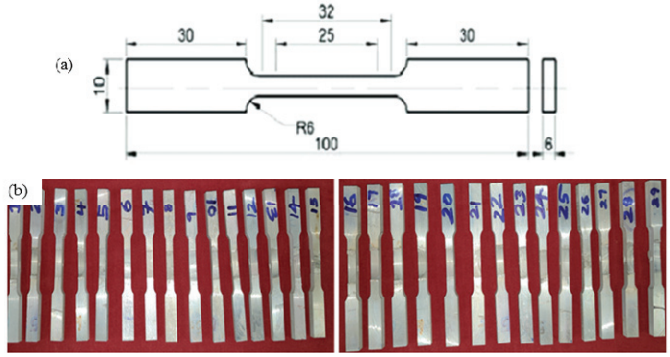

Fig. 2. Tensile strength; a) test specimen dimension; b) dog bone test specimens.

traverse speed = 80 mm/min with triple pass. The modification without changing the rpm showed good improvement in tensile strength which coincides.[20] After the tensile strength test, similar dimensions of welded zones are carried out for the corrosion test by weight loss method.

TABLE I. Tensile strength results of the prepared FRSTW test specimens

SampleNo.	Tensile stress MPa	Sample No.	Tensile stress MPa	Sample No.	Tensile stress MPa
1	114	11	97	21	94
2	109	12	115	22	108
3	104	13	92	23	105
4	112	14	117	24	93
5	126	15	107	25	115
6	123	16	118	26	137
7	124	17	121	27	116
8	130	18	113	28	110
9	99	19	106	29	129
10	111	20	103		

Characterization

The butt weld of the aluminum alloy (AA5052 and AA6101-T6) joint's surface grains nature was analyzed by morphological method. To measure the welded joints nature, this work selected sample numbers such as 1, 4, 8, 9, 13 and 26 for microstructure analysis. Fig. 3 exposed surface morphology of the selected samples such as 90 mm/min, 8 kN×1200 rpm×2 pass, 80 mm/min×7 kN×1200 rpm×2 pass, 80 mm/min×7 kN×1000 rpm×3 pass, 90 mm/min×7 kN×1200 rpm×1 pass, 80 mm/min×7 kN×1400 rpm×1 pass, and 80 mm/min×6kN×1200 rpm×3 pass specimens surface grain nature.

Fig. 3a revealed the pancakes like grains due to higher speed and force. This image revealed that the higher load and processing heat energy may be the reason for these slight cracks. The grains are of almost uniform size which may cause good durability at high temperatures. Similar size hair cracks are found in sample number 8 and 9 (Fig. 3c and d). Fig. 4f shows the lower grain size and micro-level hair cracks. Triple passes at lower RPM and lower passes with higher RPM cause uneven pancakes or hair cracks. The parameters such as higher strain, heat, and exciting strains cause distinct microstructures in FRSTW aluminum alloys. Tool-induced plastic deformation and frictional heat between plates extend grain structure before welding refines it at the junction. Due to material interaction with the shoulder, tool pin, and process factors, the "nugget", was formed on the surface. The welded zones have shown pricklier stretched microstructure in which the grains are oriented alongside the progressing direction (Fig. 3e). The microstructure has etched pits and grains slightly smaller than AA6101 aluminum alloy. Gwyddion processed image is shown in Fig. 3g.

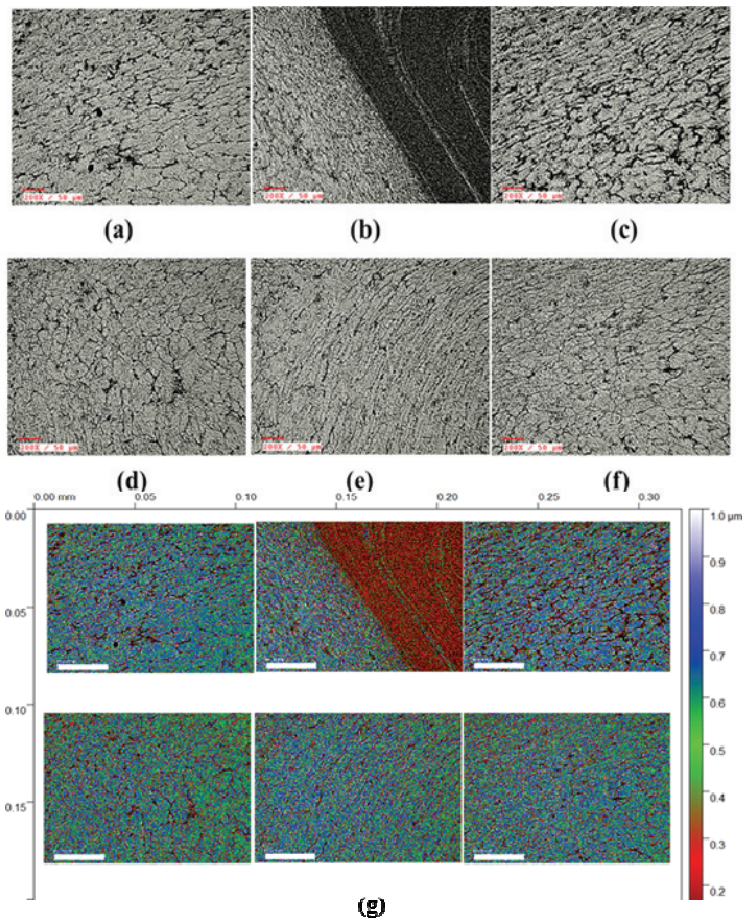

Fig. 3. Microstructure images of FRST welded test samples: a) 1, b) 4, c) 8, d) 9, e) 13, f) 26 and g) 5 Gwyddion processed microstructure images of FRST welded test samples.

Welded samples 4, 13 and 16 were XRD analyzed after microstructure characterization. The identification of alloy combinations was done using the 2θ *versus* intensity relationship. The XRD patterns of trials 4, 13 and 26 showed the composition of metals and aluminum in combination, accordingly. The XRD patterns show up at 2θ 38.66, 44.89, 65.21 and 78.33 in Fig. 4. These 2θ values validate the Al_3M molecular formula of the remaining metal elements. They verified that the welded zones of corrosion-resistant aluminum alloys were tightly bound. The results showed that the welding was stable. α-Al metallic solution phases, $MgZn_2$ and $CuAl_2$ intermetallic compounds (*hkl*) values were observed in all processed XRD patterns. The observed values from Match-3 software are presented in Table II. The values are almost coincidental with the aluminum alloys welded zone reports as shown.[21–26]

TABLE II. XRD analysis outcomes of FRSTW welded samples

Sample No.	*hkl*	2θ / °	*D* / nm
4	111	38.66	2.33
	200	44.89	2.02
	202	65.21	1.43
13	111	38.66	2.33
	200	44.89	2.02
	202	65.21	1.43
	311	78.33	1.22
26	111	38.66	2.33
	200	44.89	1.99
	202	65.21	1.41
	311	78.33	1.20

Samples were carried out for the energy dispersive analysis to identify the alloy metals present in the anodic and cathodic metals of FRSTW specimens. The energy values are compared with MA table element energy. All welded specimens have shown similar energy level peaks. The boundary region EDAX exposed the peaks at 0.02–0.073(noise), 0.64–0.73 (O K), 1.23–1.25 (Mg K), 1.46–1.51 (Al K), 1.82–1.85 (Si K), 4.9–4.99 (V or Cr), 6.31–6.4 (Fe/Mn K) and 7.1–7.2 (Fe Kβ1) keV. The obtained values are coincidental with the reported data and confirm the elements of the selected base metals compositions.[27–30] The intermetallic region exposed the Al_3Mg_2 and metal oxides of higher-composition metals. These results revealed and supported the butt-welded zone deformation with grains structure. Also, results revealed the similarities in welded zones. In addition, α-Al (FeMn) Si may be the reason for the different coarse sizes observed in the microstructure of FRSTW specimens. The deformed boundary was observed from the microstructure and confirmed by EDAX shown in Fig. 4.

Corrosion studies

The selected sample's surface area was measured and carried for the weight loss investigations by immersion technique.[40] Different corrosive mediums were selected as per the experimental discussion and the weight loss for all the samples individually. Weight loss was studied in various corrosive media. Base metals AA5052 and AA6101-T6 with other corrosion-tested aluminum welded joints after 72 h. As the sample dries, a black corrosion film covers the whole surface, and white, shiny products are created, indicating that the parent metal has low corrosion resistance. There is a great deal of variance, however, in the corrosion regions of the welding joints when subjected to various process settings. The recorded outcomes are presented in Tables III and IV. Sample 1 showed the lowest weight loss in the acid medium and sample 15 exposed higher loss in the same medium. From the observed weight loss of the 29 samples, this work calculated the average weight loss of 215 mg. Likely, this work observed the

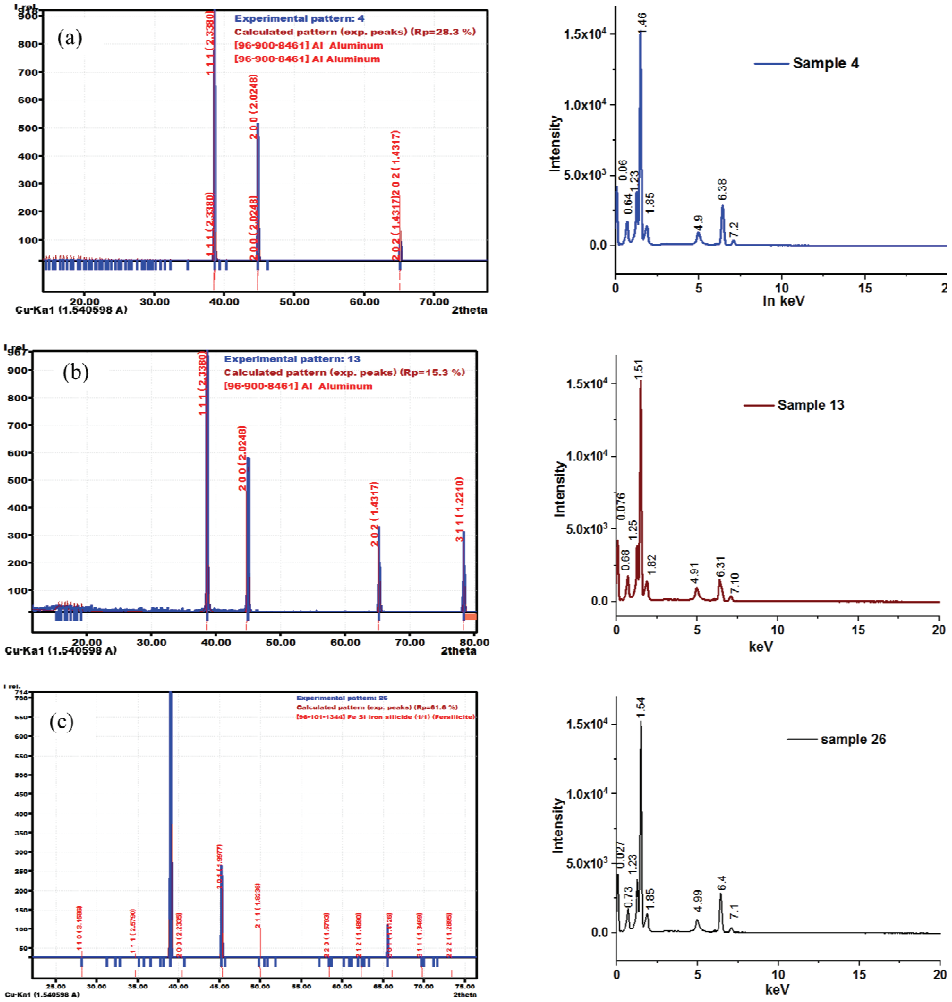

Fig. 4. XRD and EDAX images for samples: a) 4, b) 13 and c) 26.

average weight losses of the samples in the order of basic medium (S.N-27 = 397 mg; low, S.N-15 = 787 mg; high), domestic water (S.N-1 = 40 mg; low, S.N-19 = = 51 mg; high), 3.5% salt solution (S.N-27 = 597 mg; low, S.N-25 = 986 mg; high) and seawater (S.N-4 = 596 mg; low, S.N-20 = 959 mg; high). The welded joints' corrosion resistance outshines that of the underlying metal, it follows. More dislocation flaws occur during rolling because the base metal's grain size is not uniform. In contrast, the dynamic recrystallization of grain size is made possible by the strong mechanical and thermal impacts of stirring processing, which results in uniformly sized grains that are reconciled in the welding joints and, as a result, fewer defects. The corrosion resistance of the welding joints is greatly

TABLE III. Initial mass, thickness and mass loss (g) in different corrosion medium

Sample No.	Mass loss in 0.1 M acid			Mass loss in 0.1 M base			Mass loss in domestic water (SPM = 880 ppm)		
	Initial mass	Final mass	Mass loss	Initial mass	Final mass	Mass loss	Initial mass	Final mass	Mass loss
AA5052	6.213	5.987	0.226	5.231	4.479	0.752	5.890	5.677	0.213
AA6101-T6	5.468	5.186	0.282	6.475	5.648	0.827	4.996	4.878	0.118
1	6.620	6.518	0.102	6.885	6.129	0.756	6.675	6.635	0.040
2	6.680	6.499	0.181	6.910	6.194	0.716	6.700	6.686	0.014
3	6.640	6.422	0.218	6.669	6.196	0.473	6.459	6.441	0.018
4	7.060	6.865	0.195	7.057	6.483	0.574	6.847	6.824	0.023
5	6.750	6.566	0.184	6.702	6.113	0.589	6.492	6.470	0.022
6	6.690	6.496	0.194	6.857	6.071	0.786	6.647	6.632	0.015
7	5.750	5.596	0.154	6.804	6.162	0.642	6.348	6.320	0.028
8	6.600	6.323	0.277	6.949	6.263	0.686	6.493	6.463	0.030
9	6.520	6.322	0.198	6.631	5.933	0.698	6.175	6.159	0.016
10	5.800	5.593	0.207	6.951	6.164	0.787	6.495	6.465	0.030
11	6.670	6.420	0.250	5.808	5.198	0.610	5.352	5.316	0.036
12	6.690	6.392	0.298	6.531	5.989	0.542	5.212	5.186	0.026
13	6.560	6.299	0.261	6.933	6.453	0.480	6.477	6.446	0.031
14	6.820	6.621	0.199	6.534	6.017	0.517	6.078	6.045	0.033
15	6.810	6.493	0.317	5.623	5.129	0.494	5.401	5.367	0.034
16	6.720	6.439	0.281	6.733	6.245	0.488	6.511	6.473	0.038
17	6.670	6.449	0.221	6.836	6.212	0.624	6.614	6.572	0.042
18	6.550	6.365	0.185	5.980	5.485	0.495	5.674	5.628	0.046
19	6.900	6.628	0.272	6.588	5.942	0.646	6.366	6.320	0.046
20	6.870	6.736	0.134	6.721	6.240	0.481	6.499	6.449	0.050
21	6.900	6.711	0.189	6.746	5.999	0.747	6.524	6.485	0.039
22	6.430	6.180	0.250	6.851	6.224	0.627	6.173	6.129	0.044
23	6.990	6.728	0.262	6.450	6.003	0.447	6.233	6.184	0.049
24	6.590	6.466	0.124	6.086	5.669	0.417	5.869	5.819	0.050
25	6.610	6.322	0.288	5.995	5.598	0.397	5.778	5.739	0.039
26	6.330	6.120	0.210	5.993	5.446	0.547	5.899	5.858	0.041
27	5.950	5.705	0.245	7.325	6.588	0.737	7.437	7.386	0.051
28	6.550	6.392	0.158	6.918	6.148	0.770	7.030	6.985	0.045
29	6.860	6.672	0.188	6.692	6.015	0.677	6.804	6.757	0.047
Average loss	0.215			0.602					0.035

enhanced as a result of this. This work observed the average weight loss of all 29 samples such as 0.602 g (basic medium), 0.035 g (domestic water), 0.766 g (3.5% salt solution) and 0.727 g (sea water). The average weight loss of the specimens in selected corrosive mediums was lowered when compared with the source metal weight loss. Also, both salt atmospheres are showing almost similar weight loss. Corrosion of metal may and will occur in saltwater. Aluminum boats still have their uses on land, but they will require some extra care when out on

the water. Galvanic corrosion is the mechanism by which salt corrodes aluminum. When compared with the reported results, three times of weight loss was observed in salt water. Also, the difference in weight loss revealed the effect of welding parameters on surface degradation. RPM and many passes in friction stir welding are the major effects on corrosion resistivity. When comparing the mediums, the order of surface deterioration exists as follows salty domestic water < acid < alkali < sea water < artificial salt water.

TABLE IV. Initial mass, thickness and mass loss in different corrosion medium

Sample No.	Weight loss in 3.5 % salt solution			Weight loss in marine water		
	Initial mass	Final mass	Mass loss	Initial mass	Final mass	Mass loss
AA5052	4.984	4.038	0.946	6.235	5.324	0.911
AA6101-T6	6.214	5.229	0.985	6.184	5.312	0.872
1	6.745	5.919	0.826	6.241	5.468	0.773
2	7.087	6.298	0.789	6.621	5.872	0.749
3	6.760	6.087	0.673	6.323	5.673	0.650
4	6.712	5.938	0.774	6.925	6.314	0.611
5	6.820	5.961	0.859	6.585	5.769	0.816
6	6.911	6.025	0.886	6.877	6.189	0.688
7	6.762	5.920	0.842	5.853	5.257	0.596
8	6.668	5.682	0.986	6.195	5.396	0.799
9	6.964	6.126	0.838	5.868	5.055	0.813
10	7.106	6.409	0.697	5.82	5.045	0.775
11	6.275	5.414	0.861	5.928	4.969	0.959
12	6.649	5.907	0.742	6.019	5.253	0.766
13	6.715	5.767	0.948	6.471	5.629	0.842
14	6.636	5.819	0.817	6.377	5.681	0.696
15	6.532	5.738	0.794	6.673	5.935	0.738
16	6.668	5.860	0.808	6.815	6.198	0.617
17	6.456	5.747	0.709	5.984	5.273	0.711
18	6.869	6.176	0.693	6.358	5.557	0.801
19	6.156	5.310	0.846	6.401	5.659	0.742
20	6.782	6.001	0.781	6.322	5.675	0.647
21	6.281	5.556	0.725	6.218	5.594	0.624
22	6.372	5.785	0.587	6.354	5.716	0.638
23	6.667	6.050	0.617	6.142	5.423	0.719
24	6.592	5.875	0.717	6.555	5.832	0.723
25	6.559	6.022	0.537	5.931	5.25	0.681
26	6.817	6.134	0.683	6.557	5.83	0.727
27	6.459	5.834	0.625	6.056	5.3	0.756
28	6.423	5.676	0.747	6.147	5.32	0.827
29	6.959	6.157	0.802	6.442	5.839	0.603
Average loss		0.766			0.727	

Using the weight loss data, this work calculated corrosion rate in terms of miles per year (Tables V) using the above-mentioned formula (1). Observation shows the same order of the specimen's corrosion rate in selected corrosive mediums.

TABLE V. Corrosion rate of FRSTW samples from weight loss

Average mass loss, g	Medium	*M* Surface area×Eq.wt×Total h	*CR* in mpy 534×mass loss/*M*
0.215	0.1 M acid	9×2.7×72	0.066
0.602	0.1 M alkali	9×2.7×72	0.184
0.035	Domestic water	9×2.7×72	0.011
0.766	3.5 % NaCl	9×2.7×72	0.234
0.727	Sea water	9×2.7×72	0.222

From the reports, this work observed that the welded materials corrosion rates are decreased in respective medium. This work observed the similar observations when compared with base metals. This research selected the magnesium and chromium containing aluminum alloys for this novel study. When compared with the reported results for the other Al alloys, our welded samples exposed good result.

A higher corrosion rate of 0.234 miles per year was shown by the artificial salt medium when compared to the other corrosive mediums. Therefore, this study expanded to include a potentiodynamic analysis of 4, 13 and 26 specimens chosen based on their tensile strength. The potentiodynamic output data opened through corrosion view software and Tafel plots are plotted (Fig. 5). The graphical outcomes are presented in Table VI. From the table, sample 13 showed higher corrosion rate when compared with other selected samples. Even sample 4 showed lower tensile strength, it showed the corrosion rate of 3.156 mpy. This is due to the deformed welded joint of FRSTW sample. The Tafel outcome data also revealed the almost equal corrosion potential from –0.87 to –0.91 V. But, the corrosion current differed in the order of sample 26 < sample 4 < sample 13. Our sample showed 0.15 V difference with FRSTW AA6082.[31] When compared with the reported potential of aluminum (Al/Al^{3+}, –1.70 V), welded samples exposed the lowered potential.[32] The movement to more positive values indicates that the corrosion resistance of the friction stir-welded samples was improved. The lowest corrosion current density, which means the highest corrosion resistance, was observed on selected specimens. I_{corr} values exist between 781.78 and 0.52 μA. The lowest value of sample 26 showed the improvement of the corrosion resistance due to the FRSTW process as per reported values.[33] When compared with the reported results, our samples have shown slightly higher corrosion potential.[34–37] Sample 26 exhibited a lower rate due to the grain nature and cathodisation with the remaining base metal compositions. This work observed the corros-

ion resistivity in the order of sample 13 > sample 4 > sample 26. When compared the other reported corrosion researches, Table VII, this work selected AA5052 and AA6101-T6 aluminium alloys joints for future submarine-based construction and water-based designs.

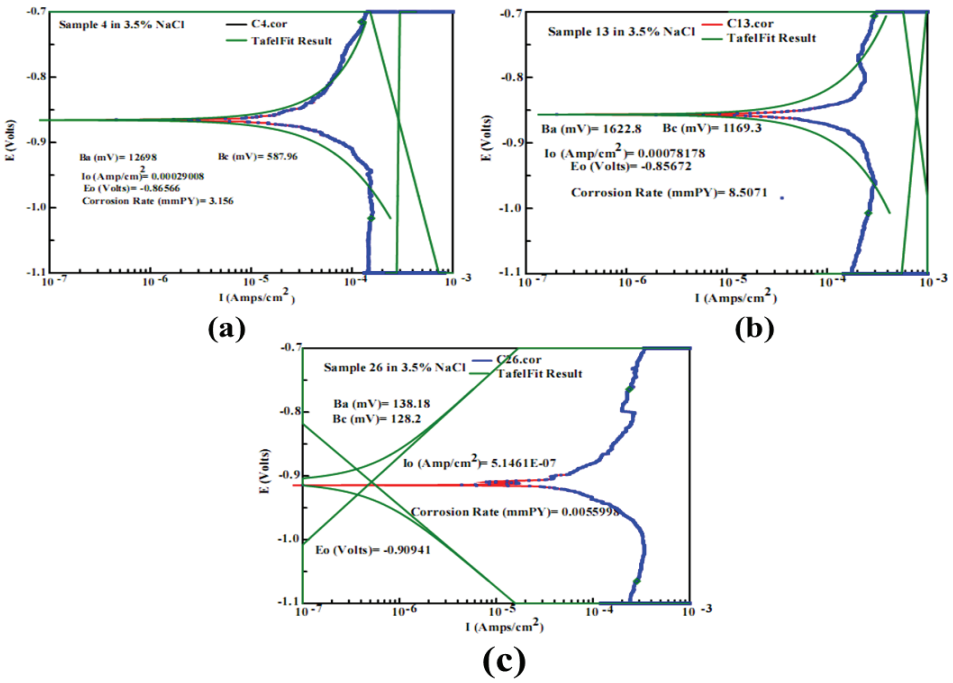

Fig. 5. Tafel plots for the test samples: a) 4 b) 13 and c) 26.

TABLE VI. Corrosion rate of FRSTW samples from potentiodynamic graph

Sample No.	Tafel data				Corrosion rate mpy
	I_{corr} / A cm^{-2}	E_{corr} / V	β_a / mV	β_c / mV	
4	0.00029008	–0.87	12698	587.96	3.156
13	0.00078178	–0.86	1622.8	1169.3	8.5071
26	0.00000052	–0.91	138.18	128.2	0.006

TABLE VII. Weight loss results of some reported aluminum alloys

Aluminum alloy	Welding	Medium	Weight loss g	Duration h	Corr. rate mpy	Ref.
AA6061 and AA8011	FRSTW	Sea water	0.204	672	0.201	2
	FRSTW	HCl	1.644	672	1.618	
	FRSTW	H_2SO_4	1.464	672	1.441	
AA5052-H32 - AA6061-T6	FRSTW	Salt spray	3.77	72	25.486	41

TABLE VII. Continued

Aluminum alloy	Welding	Medium	Weight loss g	Duration h	Corr. rate mpy	Ref.
Al 2024	Raw sample	3.5 % Salt water	–	–	1.200	42
Similar 2219	FRSTW	Salt fog	–	48	0.090	43
Similar 5083	FRSTW	Salt fog	–	48	0.009	43
5083-2219	FRSTW	Salt fog	–	48	0.030	43

CONCLUSIONS

The microstructure, tensile strength, and electrochemical characteristics of friction stir-welded AA5052 and AA6101-T6 were examined in the aforementioned investigations. Three distinct traverse speeds 70, 80 and 90 mm/min, and three distinct rotational speeds 1000, 1200 and 1400 rpm are required for this task. In addition to these three different passes. The nugget zone grain size is exaggerated by process parameters such as tool traverse speed, tool passes and tool traverse speed. Microstructure images have confirmed the solid solution formed between the selected aluminum alloys. The FRSTW tool parameters were modified and successfully this work prepared 29 samples. The sample weight loss results showed that the welding is effectively protecting the metal surfaces in all corrosive medium except salt and alkali medium. In a salt medium, aluminum underwent galvanic corrosion and more weight loss was observed. Likely, in an alkali medium aluminium hydroxide formed, and moderate weight loss was observed. According to potentio-dynamic experiments, AA5052 and AA6101-T6 FRST butt-welds in 3.5 % NaCl solution exhibits improved corrosion control characteristics. The results of the experiments showed that the corrosion current density can be improved by modifying the welding parameters. This work concluded that the 80mm/min–6 kN–1200 RPM–3 passes may be a good parameter for welding and the alloy joint may have higher tensile strength with corrosion resistivity. An evaluation of mechanical properties and electrochemical corrosion performances revealed that the fine and uniform weld microstructure at 1200 rpm outperformed FRSTW joints at 80mm/min in terms of potential, corrosion current density, and tensile strength. The future course study includes the corrosion resistive coating materials according to sacrificial anodic, cathodization and inhibition studies.

Acknowledgment. The authors express their gratefulness to Dr. R. Jayaprakash, Associate Professor, School of Arts and Science, AVIT campus, VMRF, Paiyanoor, Chennai, for his guidance and for providing Vasan R&D lab facility for the corrosion and inhibition studies.

ИЗВОД

ПРОУЧАВАЊЕ КОРОЗИЈЕ, ЕФЕКТИ ПАРАМЕТАРА И ПОВРШИНСКА МОРФОЛОГИЈА AA5052-AA6101T6 ЗАВАРЕНИХ СПОЈЕВА ТРЕЊЕМ И МЕШАЊЕМ

SATHISH RENGARAJAN[1] G. KASIRAJAN[2] и R. ASHOKKUMAR[3]

[1]Department of Mechanical Engineering, St. Joseph's College of Engineering, Semmancheri, Chennai, Tamil Nadu-600119, India, [2]Research Scholar, Department of Mechanical Engineering, St. Joseph's College of Engineering, Semmancheri, Chennai, Tamil Nadu-600119, India и [3]Department of Mechanical Engineering, SRM Madurai College for Engineering and Technology, Nedungulam Main Rd, Pottapalayam, Tamil Nadu-630611, India

Традиционално заваривање фузијом није погодно за заваривање легура алуминијума јер се формирају секундарне крте фазе, а како легура очвршћава јавља се порозност и пукотине. Заваривање трењем, је нова метода заваривања у чврстом стању, којом се могу спојити сличне или различите легуре алуминијума. У овом раду узорци легура AA5052-AA6101T6 који су заварени трењем и мешањем, тестирани су на карактеристике корозије. Микроструктура и механичко понашање заварених спојева алуминијумске легуре AA5052-AA6101T6 испитани су у односу на улазне параметре. Микроструктура открива да брзина заваривања и брзина ротације утичу на микроструктуру шава анализираних узорака заварених површина. Двадесет девет узорака је тестирано на корозију у 3,5 % NaCl, води за домаћинство (880 ppm – SPM), 1 M H_2SO_4, 1 M NaOH и природној морској води током 72 сата. Домаћа слана вода и кисели медијум показали су бољу отпорност на корозију од алкалних и сланих медија. Проучавање отпора показало је благе промене анодног и катодног потенцијала након заваривања трењем.

(Примљено 17. априла, ревидирано 19. маја, прихваћено 24. августа 2024)

REFERENCES

1. Y. Chen, H. Wang, H. Li, X. Wang, H. Ding, J. Zhao, F. Zhang, *Metals* **9** (2019) 718 (https://doi.org/10.3390/met9070718)
2. R. Alfattani, M. Yunus, A. F. Mohamed, T. Alamro, M. K. Hassan, *Materials* **15** (2022) 260 (https://doi.org/10.3390/ma15010260)
3. R. S. Mishra, Z. Y. Ma, *Mater. Sci. Eng. Rep.* **50** (2005) 1 (https://doi.org/10.1016/j.mser.2005.07.001)
4. R. Sathish, A. Sathish Kumar, R. Ashok Kumar, *Bull. Chem. Soc. Ethiop.* **38** (2024) 811 https://dx.doi.org/10.4314/bcse.v38i3.20)
5. J. K. Paik, *Int. J. Nav. Archit. Ocean. Eng.* **1** (2009) 39 (https://doi.org/10.2478/IJNAOE-2013-0005)
6. E. T. Akinlabi, A. Andrews, S. A. Akinlabi, *Trans. Nonferrous Met. Soc. China* **24** (2014) 1323 (https://doi.org/10.1016/S1003-6326(14)63195-2)
7. P. V. Kumar, G. M. Reddy, K. S. Rao, *Def. Technol.* **11** (2015) 362 (https://doi.org/10.1016/j.dt.2015.04.003)
8. V. N. Nguyen, Q. M. Nguyen, H. T. D. Thi, S. C. Huang, *Sādhanā* **43** (2018) 160 (https://doi.org/10.1007/s12046-018-0930-y)
9. R. Pruthviraj, M. Rashmi, *J. Mater. Sci. Eng.* **5** (2016) 1000221 (https://doi.org/10.4172/2169-0022.1000221)
10. B. Ratna Sunil, G. Pradeep Kumar Reddy, Duc Pham, *Cogent Eng.* **3** (2016) 1145565 (https://doi.org/10.1080/23311916.2016.1145565)
11. R. P. Mahto, S. Anishetty, A. Sarkar, O. Mypati, S. K. Pal, J. D. Majumdar, *Met. Mater. Int.* **25** (2019) 752 (https://doi.org/10.1007/s12540-018-00222-x)

12. F. Gharavi, K. A. Matori, R. Yunus, N. K. Othman, F. Fadaeifard, *J. Mater. Res. Tech*. **4** (2015) 314 (https://doi.org/10.1016/j.jmrt.2015.01.007)
13. K. Amini, F. Gharavi, *J. Cent. South Univ.* **23** (2016) 1301 (https://doi.org/10.1007/s11771-016-3180-3)
14. A. Davoodi, Z. Esfahani, M. Sarvghad, *Corros. Sci.* **107** (2016) 133 (https://doi.org/10.1016/j.corsci.2016.02.027)
15. Y. Feng, F. Yang, Y. Bi, *Int. J. Electrochem. Sci.* **17** (2022) 221039 (https://doi.org/10.20964/2022.10.40)
16. S. Khorsand, Y. Huang, in: *Light Metals 2017. The Minerals, Metals & Materials Series*, A. Ratvik, Ed., Springer, Cham, 2017 (https://doi.org/10.1007/978-3-319-51541-0_32)
17. M. Krol, P. Snopinski, B. Tomiczek, T. Tanski, W. Pakiela, W. Sitek, *P. Est. Acad. Sci.* **65** (2016) 107 (https://doi.org/10.3176/proc.2016.2.07)
18. D. A. Wadeson, X. Zhou, G. E. Thompson, P. Skeldon, L. D. Oosterkamp, G. Scamans, *Corros. Sci.* **48** (2006) 887 (https://doi.org/10.1016/j.corsci.2005.02.020)
19. H. Longgang, J. Jiajia, Z. Di, Z. Linzhong, Z. Li, J. Jishan, *Rare. Metal. Mat. Eng.* **46** (2017) 2437 (https://doi.org/10.1016/S1875-5372(17)30212-6)
20. C. Elanchezhian, B. V. Ramnath, P. Venkatesan, S. Sathish, T. Vignesh, R. V. Siddharth, K. Gopinath, *Procedia Eng.* **97** (2014) 775 (https://doi.org/10.1016/j.proeng.2014.12.308)
21. O.M. Khalil, I. Mingareev, T. Bonhoff, A. F. El-Sherif, M. C. Richardson, M. A. Harith, *Opt. Eng.* **53** (2014) 014106 (https://doi.org/10.1117/1.OE.53.1.014106)
22. J. Martin, A. Nominé, V. Ntomprougkidis, S. Migot, S. Bruyère, F. Soldera, G. Henrion, *Mater. Des.* **180** (2019) 107977 (https://doi.org/10.1016/j.matdes.2019.107977)
23. R. H. U. Khan, A. Yerokhin, X. Li, H. Dong, A. Matthews, *Surf. Coat. Tech.* **205** (2010) 1679 (https://doi.org/10.1016/j.surfcoat.2010.04.052)
24. G. Gautam, N. Kumar, A. Mohan, R.K. Gautam, S. Mohan, *J. Mater. Sci.* **51** (2016) 8055 (https://doi.org/10.1007/s10853-016-0076-4)
25. M. Jin, B. Lee, J. Yoo, Y. Jo, S. Lee, *Met. Mater. Int.* (2024) (https://doi.org/10.1007/s12540-023-01594-5)
26. C. Rathinasuriyan, V. S. Kumar, *J. Mech. Sci. Technol.* **31** (2017) 3925 (https://doi.org/10.1007/s12206-017-0738-4)
27. Z. F. Syed, T. R. Tamilarasan, M. S. Dennison, *Aus. J. Mech. Eng.* **21** (2023) 844 (https://doi.org/10.1080/14484846.2021.1914891)
28. K. Chandra, V. Kain, *Eng. Fail. Anal.* **34** (2013) 387 (https://doi.org/10.1016/j.engfailanal.2013.09.007)
29. F. Gharavi, K. A. Matori, R. Yunus, N. K. Othman, F. Fadaeifard, *Trans. Nonferrous Met. Soc. China* **26** (2016) 684 (https://doi.org/10.1016/S1003-6326(16)64159-6)
30. D. E. Newbury, N. W. Ritchie, *Microsc. Microanal.* **21** (2015) 1327 (https://doi.org/10.1017/S1431927615014993)
31. A. Laska, M. Szkodo, D. Koszelow, P. Cavaliere, *Metals* **12** (2022) 192 (https://doi.org/10.3390/met12020192)
32. L. Veleva, *Corrosion Tests and Standards: Application and Interpretation*, R. Baboian, Ed., ASTM International, West Conshohocken, PN (ISBN: 0-8031-2058-3 (2005), pp. 387-404)
33. H. L. Qin, H. Zhang, D. T. Sun, Q. Y. Zhuang, *Int. J. Miner. Metall. Mater.* **22** (2015) 627 (https://doi.org/10.1007/s12613-015-1116-9)
34. F. T. Owoeye, O. R. Adetunji, A. Omotosho, A. P. Azodo, P. O. Aiyedun, *Eng. Rep.* **2** (2020) 12103 (https://doi.org/10.1002/eng2.12103)

35. N. R. Ramesh, V. S. Kumar, *Appl. Ocean Res.* **98** (2020) 102121 (https://doi.org/10.1016/j.apor.2020.102121)
36. E. Aldanondo, J. Vivas, P. Alvarez, I. Hurtado, *Metals* **10** (2020) 872 (https://doi.org/10.3390/met10070872)
37. H. F. Wang, J. L. Wang, W. W. Song, D. W. Zuo, D. L. Shao, *Int. J. Electrochem. Sci.* **11** (2016) 6933 ((https://doi.org/10.20964/2016.08.09)
38. B. I. Attah, R. O. Medupin, T .D. Ipilakyaa, U. G. Okoro, O. Adedipe, G. Sule, O. M. Ikumapayi, K. C. Bala, E. T. Akinlabi, S. A. Lawal, A. S. Abdulrahman, *Manuf. Rev*. **11** (2024) 7 (https://doi.org/10.1051/mfreview/2024003)
39. Y. Wang, H. Jiang, X. Wu, Q. Meng, *Crystals* **13** (2023) 582 (https://doi.org/10.3390/cryst13040582)
40. R. Saravanakumar, T. Rajasekaran, C. Pandey, *J. Mater. Eng. Perform.* **32** (2023) 10175 (https://doi.org/10.1007/s11665-023-07836-2)
41. S. Balamurugan, K. Jayakumar, A. S. Banu, K. Ragupathi, *Eng. Proc.* **61** (2024) 12 (https://doi.org/10.3390/engproc2024061012)
42. M. Starostin, G. E. Shter, G. S. Grader, *Mater. Corros.* **67** (2016) 387 (https://doi.org/10.1002/maco.201508552)
43. M. Koilraj, A. Sathesh Kumar, D. L. Belgin Paul, S. R. Koteswara Rao, *Appl. Mech. Mater* **813**–**814** (2015) 203 (https://doi.org/10.4028/www.scientific.net/AMM.813-814.203).

Journal of the Serbian Chemical Society
JSCS-info@shd.org.rs • www.shd.org.rs/JSCS
J. Serb. Chem. Soc. *90* (3) 369–382 (2025)
JSCS–5393
Original scientific paper
Published 10 November, 2024

Waste corn silk for eco-friendly silver nanoparticles: Green synthesis, characterization and determination of enzyme inhibition properties

MERVE KESKIN*

Vocational School of Health Services, Bilecik Şeyh Edebali University, Bilecik, Türkiye

(Received 22 May, revised 11 June, accepted 27 September 2024)

Abstract: Due to the increasing population and consumption rate, the sustainable use of resources is very important. Corn is one of the most produced grains in the world. However, many parts of it, such as corn silk, roots and corn husk are disposed of as agricultural waste. Within the sustainability, it is possible to bring waste into the field of technology and develop new products with green synthesis. In this study, the waste corn silk was dried, extracted and used as a precursor in synthesis of silver nanoparticles (CS–AgNPs). The CS–AgNPs were characterized using ultraviolet spectrophotometry, infrared spectrophotometry and scanning transmission electron microscope. Moreover, the inhibition effects of CS–AgNPs on enzymes such as α-amylase, α-glycosidase, urease, acetyl cholinesterase and xanthine oxidase which are important for the treatment of some diseases were determined. The obtained nanoparticles gave the maximum absorbance at 470 nm and the average size of the nanoparticles was found as 65 nm. It was determined that CS–AgNPs showed very good antioxidant activity and inhibitory effects on α-amylase (52.27 %), α-glycosidase (43.51 %), urease (80.33 %), acetyl cholinesterase (66.17 %) and xanthine oxidase (73.67 %). The obtained results show that the nanoparticles synthesized using the green synthesis technique could be used in medicine and pharmaceuticals.

Keywords: eco-friendly; diabetes mellitus; antioxidant activity; inhibition; waste management; sustainability.

INTRODUCTION

In recent years, the whole world is facing various challenges due to the unsustainable use of natural resources and the increasing population. For this reason, European Union countries have planned the European growth strategy for 2020 and set the goal of transitioning from a linear production and consumption model to a recyclable production and consumption model.[1] The amount and content of solid waste produced are affected by different factors, such as the socio-

* Corresponding author. E-mail: merveozdemirkeskin@gmail.com
https://doi.org/10.2298/JSC240522085K

economic characteristics of the community or societies, nutritional habits, traditions, geography, professions and climate.[2] It is estimated that the world population, which will be 7.9 billion by 2022, will reach 9.8 billion in 2050. On the other hand, it is known that the food production rate is higher than the human population growth rate and today the food production is sufficient to feed 10 billion people.[3] Agricultural wastes are wastes and residues resulting from the production and processing of plant and animal products. Food waste could be defined as the food lost at every stage of the food supply chain, from farm to table, originating from producers, processors, retailers and consumers.[4] However, every year approximately 30 % of production appears as waste in the food supply chain.[5] The random abandonment and non-use of agricultural, food and domestic waste, which increases day by day, causes air pollution, soil pollution, *etc*. For this reason, the issue of evaluation and management of agricultural wastes has gained great importance in recent years.

Nanotechnology is a popular scientific area that allows to the processing, measurement, design, modelling and editing of materials at sizes of 1–100 nm. It provides technologically advanced or completely new physical, chemical, and biological properties to matter at the atomic and molecule level.[6] Because of their unique properties, nanoparticles could be used in many areas such as food, cosmetic, energy, agricultural and medical industries, which makes the nanoparticles very popular.[6]

Nanoparticles such as gold, nickel, zinc, silver, platinum and copper are synthesized in two ways: top-down or top-up.[6] Different methods such as biological (green), physical and chemical methods are used in the synthesis of nanoparticles. Synthesis with biological resources has attracted more attention than other methods because the synthesis process does not contain toxic chemicals or products, it is fast and provides cheaper synthesis.[7] Various parts of plants are used in synthesis with the biological method.[8] However, especially the use of waste parts of plants is very important in terms of environment and sustainability.[9]

Corn (*Zea mays* L.) is a plant of high commercial importance grown almost all over the world. While world corn production exceeded 1 billion tons, it reached 361 million tons only in America.[10] The corn plant consists of various parts such as stalk, leaves, cobs, husk, silk and roots, each playing a crucial role in its growth and reproduction. But, the majority of the silks found on the cob of produced corn are thrown away as garbage and in general it is not used in industrial processes.[10] Corn silk refers to the fine, thread-like strands that form the outer part of a cob of corn.[10] It’s the long, silky, shiny fibres that are found beneath the green husks and surround the kernels. While they might seem like mere packaging, corn silk actually plays a role in the growth and development of the corn plant. When harvesting corn, the silk is usually removed along with the husk, as it's not typically consumed.[10] The corn silk could be considered a source of antioxidants and may have

potential health benefits.[10] As the waste part of the plant, it contains 70.26 % carbohydrates, 11.06 % ash, 10.10 % oil and 6.26 % protein in average.[10] Additionally, corn silk is rich in valuable biochemical substances such as essential oils, lipids, phenolic compounds and flavonoids.[10] However, the nutritional value of corn silk isn't well-studied compared to other parts of the corn plant and it is destroyed as waste. However, the corn silk has potential in green synthesis of silver nanoparticles with its bioactive compounds.

The silver nanoparticles (AgNPs) are important metallic nanoparticles which are listed in the Organisation for Economic Co-operation and Development (OECD).[11] They have many application areas such as electronic, medical appliances, tableware, clothing, cosmetics, *etc*.[18] Many studies have investigated the microbial activity of AgNPs;[12–14] however, much less is known about the enzyme inhibition properties with nanoparticles. The enzyme inhibition studies are important to develop new drugs for many diseases. For example; the inhibitions of alpha amylase and alpha glycosidase are important for treatment of *Diabetes mellitus*;[15] inhibition of xanthine oxidase is important for the treatment of gout;[16] the inhibition of acetylcholine oxidase is important for Alzheimer's[17] and the inhibition of urease is important for treatment of stomach diseases such as ulcer and gastric.[18]

The synthesizing silver nanoparticles using plant sources is quite common.[6,9,12–14] However, many of the plants used in the synthesis process have nutritional value and are consumed by humans. In this study, the potential of plants that are not preferred to be consumed by humans, but are rich in phytochemicals for the synthesis of silver nanoparticles was determined. This study focused on the synthesis of silver nanoparticles with waste corn silk, and the inhibition properties of synthesized silver nanoparticles on enzymes which has key role in the treatment of diseases such as *Diabetes mellitus*, Alzheimer, gout and ulcer. The antioxidant activity of silver nanoparticles was also determined. As a result of the study, the potential of using nanoparticles as an enzyme inhibitor for the treatment of diseases was identified.

EXPERIMENTAL

Green synthesis of corn silk-based silver nanoparticles

The corn silk silver nanoparticles were synthesized according to the Keskin.[19] For this purpose, corn silk was harvested from a field located in Bilecik, Türkiye (39° and 40°31' north latitude and 29°43' and 30°41' east longitude) in 2023. The corn silk was washed to remove impurities, dried and ground and then the known amount of the corn silk was extracted by distilled water in ratio 1:100, using the maceration technique described previous by Keskin.[19] The prepared extract was filtered and mixed with 5 mM silver nitrate ($AgNO_3$, Sigma–Aldrich) solution in a dark flask at a 1:1 volume ratio for ~2 h at room temperature. The changes of colour and confirmation of nanoparticle synthesis was applied by UV absorption spectroscopy (Hach, DR/4000U) between 250 and 750 nm (Fig. 1). At the end of the synthesis, centrifugation was performed for 15 min at 9000 rpm with a high-speed centrifuge device to precipitate AgNPs

from the aqueous medium. The resulting AgNPs were washed with distilled water to wash off impurities and dried at 75 °C.

Fig. 1. Synthesis of CS–AgNPs.

The obtained silver nanoparticles were characterized using a UV spectrophotometer (Hach, DR/4000U) to detect the colour changes, Fourier transform infrared spectroscopy (FT--IR, Thermo Fisher) to determine the functional groups that were changed (reduced–oxidized), and a scanning electron microscope (SEM, ZEISS/Supra 40 VP) device to determine the sizes of the nanoparticles. The EDX analyses was performed to determine the elemental composition of nanoparticles as combined SEM-EDX.

Determination of optimum conditions for green synthesis of CS–AgNPs

To determine the effect of extract concentration on silver nanoparticle synthesis, 1.0, 2.0 and 3.0 % corn silk extracts were prepared at room conditions, silver nanoparticles synthesized and UV spectrophotometer absorbance values were compared.

To examine the effect of pH on silver nanoparticle synthesis, the corn silk extracts were prepared in different buffer solutions such as acetic acid sodium acetate buffer (pH 5.0 and 6.0) phosphate buffer (Na_2HPO_4/NaH_2PO_4, pH 8.0 and 7.0) and the glycine buffer solutions (pH 9.0). The nanoparticle synthesis was performed with each solution separately and the UV spectrophotometer absorbance values were compared.

To determine the temperature effect on silver nanoparticle synthesis, the silver nanoparticles were obtained at 20, 40 and 60 °C and also the UV spectrophotometer absorbance values were compared.[11]

Determination of total phenolic content of CS–AgNPs and corn silk extract

To determine the total phenolic content of both CS–AgNPs and corn silk extract the Folin method was used.[20,21] The phenolic compounds and Folin–Ciocâlteu reagent become a coloured complex and gave a maximum absorbance at 765 nm. Gallic acid (GA) was used as standard. The results were expressed in mg GAE/g dried weight (DW) sample. All the analyses were performed in triplicate.

2,2-Diphenyl-1-picrylhydrazyl (DPPH)·radical scavenging activity

DPPH$^{\bullet}$ is a radical which is used to determine antioxidant activity of various materials.[22] For this purpose, a stock methanol solution (100 μM) of this purchased radical was applied. The sample solutions at different concentrations were prepared by diluting the extracts of the samples with their own solvents. The equal volumes (750 μL) of DPPH$^{\bullet}$ solution and the sample solutions (at different concentrations) were mixed and left at room temperature for 50 min and then the absorbance was recorded at 517 nm.[22] By plotting these absorbance values against the concentrations, the SC_{50} values were calculated and expressed against the Trolox standard.[22] All analyses were performed in triplicate.

Iron reducing capacity (FRAP)

The FRAP method is based on reducing the iron (III) ion in the Fe(III)–TPTZ complex by natural products compounds.[23] Fe(III), which is reduced by the antioxidant substances in the solution, gives absorbance at 593 nm. The results were expressed in μM $FeSO_4 \cdot 7H_2O$ value. All analyses were performed in triplicate.

α-*Amylase enzyme inhibition*

To determine free α-amylase enzyme activity, an equal volume of enzyme solution was incubated with 300 μL of substrate for 30 min at a suitable temperature. At the end of the relevant period, an equal volume of DNS solution was added to the reaction mixture. The reaction mixtures were heated in a boiling water bath for 5–10 min. The colour formation was achieved by boiling. After the tubes cooled in an ice bath to room temperature, the absorbance against the blank was measured at 550 nm. For the inhibition study, increasing concentrations of inhibitor were added to the medium and activity was determined, the results were plotted and the IC_{50} value was calculated.[24] The prosedure was also performed for the corn silk extract. All analyses were performed in triplicate.

α-*Glucosidase enzyme inhibition*

The inhibition properties of *α*-glucosidase was determined according to Gholamhoseinian *et al.*[25] *p*-Nitrophenyl-*α*-D-glucopyranoside was used as substrate and the reaction was performed in 0.1 M pH 6.8 phosphate buffer solution. 5 μL of substrate, enzyme solution, 900 μL of phosphate buffer (50 mM) were mixed and 20 μL of silver nanoparticle solutions was added to the mixture. The mixture was incubated at 37 °C and the calculations were made by recording the absorbance values at 405 nm. The prosedure was also performed for the corn silk extract. All analyses were performed in triplicate.

Acetylcholinesterase inhibition

The acetylcholinesterase (ACT) inhibition was based on the coloration of thiocholine with DTNB.[26] The enzyme solution was prepared in 1% gelatin solution at 2.5 units mL^{-1}. 50 μL of enzyme solution and 50 μL of silver nanoparticle solutions and 3 mL of pH 8 phosphate buffer were mixed and incubated for 5 min at 25 °C. The reaction was started after the addition of 100 μL DTNB and 20 μL ACT. After 10 min, the absorbance was measured at 412 nm and the inhibition values were calculated. The positive control was performed using donepezil hydrochloride. The prosedure was also performed for the corn silk extract. All the analyses were performed in triplicate.

Urease inhibition

Urease is an enzyme that catalyzes the conversion of urea to amonium and carbon dioxide. The formation of urea was determined using the indophenol method.[27] Jack Bean urease (200 μL), 500 μL 0.01 M of phosphate buffer solution with 100 mM urea, 1 mM EDTA and 0.01 M LiCl at pH 8.2 and 100 μL silver nanoparticle solution was incubated for 20 min at room temperature. After the period, 550 μL of phenol solution (1 % phenol and 0.005 % sodium nitroprusside) and 650 μL of alkaline mixture (0.5 % sodium hydroxide and 0.1 vol. % NaOCl) were added to the tubes. The absorbances was recorded at 625 nm after 50 min. IC_{50} values were determined using standards from different concentrations. The prosedure was also performed for the corn silk extract. All the analyses were performed in triplicate.

Xanthine oxidase inhibition

The inhibition properties of xanthine oxidase enzyme were determined according to Baltaş *et al.*[27] The reaction mixture contains 500 µL silver nanoparticles, 770 µL pH 7.8 phosphate buffer and 70 µL xanthine oxidase enzyme. After preincubation for 15 min at 25 °C, 660 µL of substrate was added to the solution and incubated for 15 min at 25 °C. The reaction was stopped by adding 200 µL 0.5 M HCl, the absorbances were determined at 295 nm and IC_{50} values were calculated. The prosedure was also performed for the corn silk extract. All the analyses were performed in triplicate.

RESULTS AND DISCUSSION

The corn silk extracts contain various such as flavonoids, phenolics, terpenoids or enzymes that act as reducing agents.[10] These bioactive compounds interact with silver ions leading to the reduction of Ag^+ to Ag. The reduced silver ions start to aggregate and form nuclei in the solution due to the reducing agents present in the extract. The further reduction and aggregation of these nuclei lead to the growth of silver nanoparticles.[28] The concentration of the extract used in the green synthesis of silver nanoparticles (AgNPs) could significantly influence the synthesis process and the properties of the resulting nanoparticles. The nanoparticle formation and the colour changes to dark brown was monitored using a UV spectrophotometer and the nanoparticles gave a maximum absorbance at 470 nm. In general, because of the free electrons, AgNPs would display a surface plasmon resonance (SPR) band at 450–550,[29] 406,[20] 435,[31], 461.25[32] and 422 nm.[33] The obtained data in this study are similar to the previously reported AgNPs synthesis result.[20–40] The changes of UV-spectrum were recorded in order to determine the optimum extract concentration. The effect of the extract concentration on the synthesis of silver nanoparticle was presented in Fig. 2.

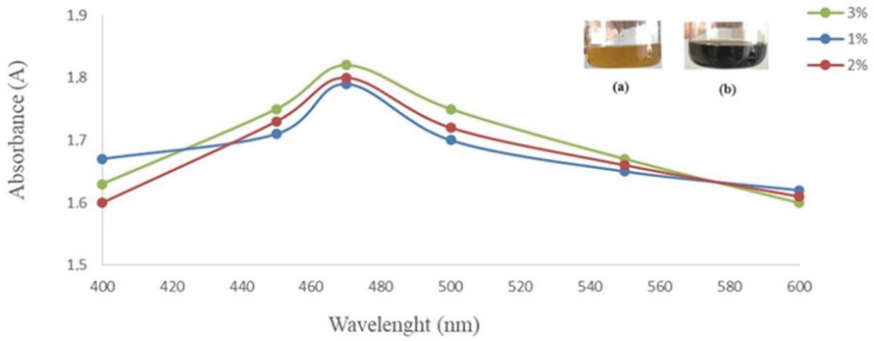

Fig. 2. Effect of extract concentration on synthesis of CS–AgNPs: a) corn silk extract and b) silver nanoparticle solution.

According to Fig. 2, the ratio 3.0 % had the maximum absorbance and it was chosen as optimum extract concentration for the further studies. The presence of large amounts of reductants in the reaction medium, such as the electron-rich

phytomolecules, is believed to cause the rapid reduction of Ag^+. This rapid reduction of Ag ions, in turn, promotes the further growth of nanoparticles. The pH is another important parameter for the green synthesis of silver nanoparticles and it can influence the interaction of the extract or bio-reducing agents with the nanoparticles. When the results of the UV-spectra were compared, it was determined that pH 7.0 is the optimum pH value for the green synthesis of silver nanoparticles (Fig. 3).

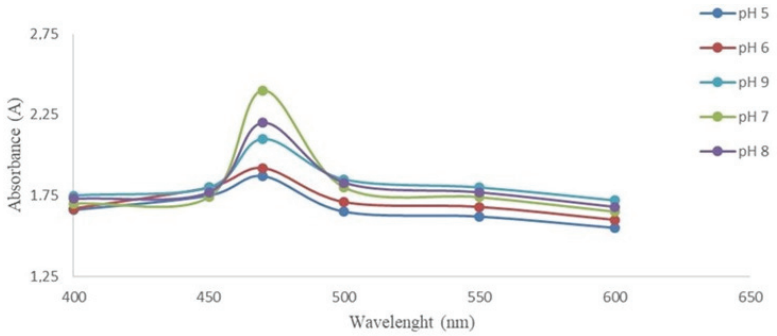

Fig. 3. Effect of pH on synthesis of CS–AgNPs.

Temperature is other crucial parameter for the green synthesis of silver nanoparticles. Elevated temperatures can speed up the reduction process, leading to quicker formation of nanoparticles. 60 °C was found the optimum temperature for the green synthesis of silver nanoparticles (Fig. 4), but synthesis was performed at room temperature to prevent or degradation of the bioactive components in the extract.

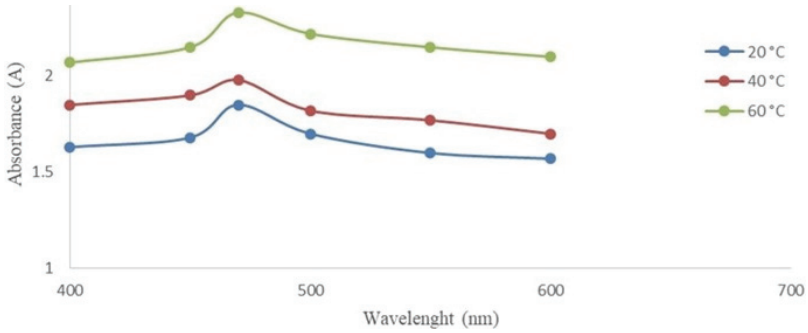

Fig. 4. Effect of temperature on synthesis of CS–AgNPs.

To determine the potential functional groups, FTIR was used. The FTIR peak of corn silk extract and supernatant of AgNPs were presented in Figs. 5 and 6, respectively. The wide peak of nearly 3275–3300 cm^{-1} indicates the presence of an O–H group in the spectrum. Although there are similarities at 2120, 1637.59

and 579 cm^{-1} peaks, there are differences at 2500, 2000–1900, 1300–1200 and 1000 cm^{-1}. These peaks are related with stretching vibrations of C=C, C=O, O–H, C–H, C–N and –COOH groups in alkane, ketone, alkene and nitro compounds.

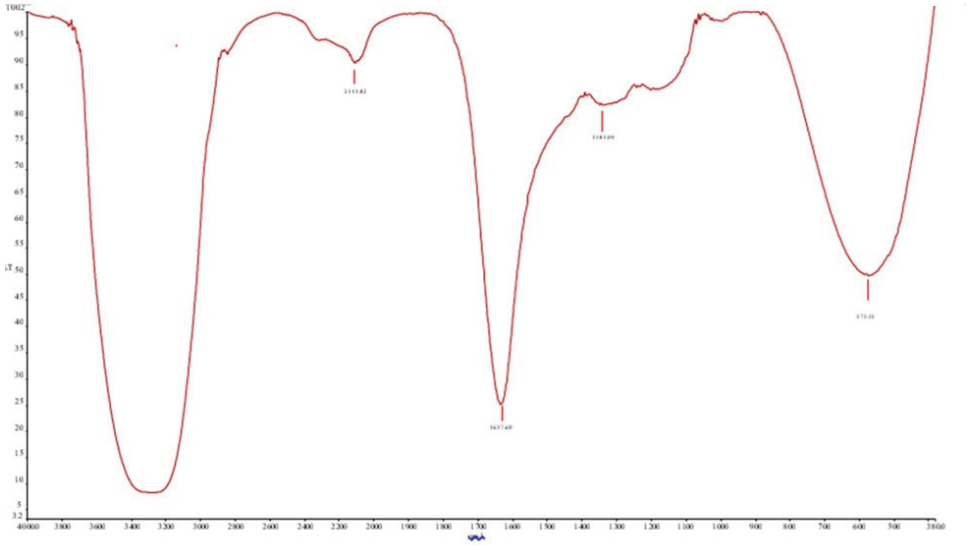

Fig. 5. FTIR spectrum of corn silk extract.

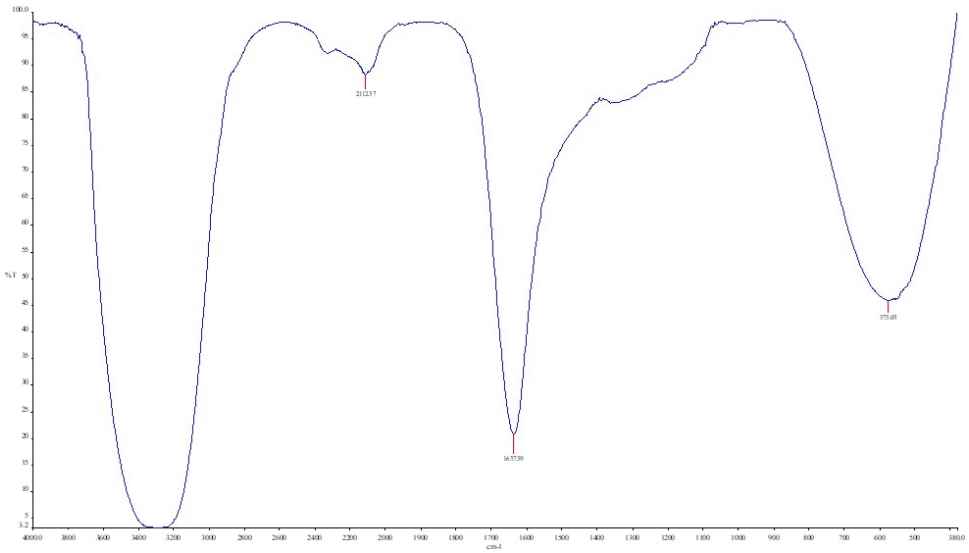

Fig. 6. FTIR spectrum of CS-AgNPs supernatant.

The particle size of the CS–AgNPs was found to be between 63 and 67 nm by the scanning electron microscope (Fig. 7). In literature, the AgNPs were obtained

in different sizes such as 4–10,[20] 65.92,[31] 12.63[32] and 46.26 nm.[33] It was clear that the particle size of AgNPs could change in a wide range.[28–38]

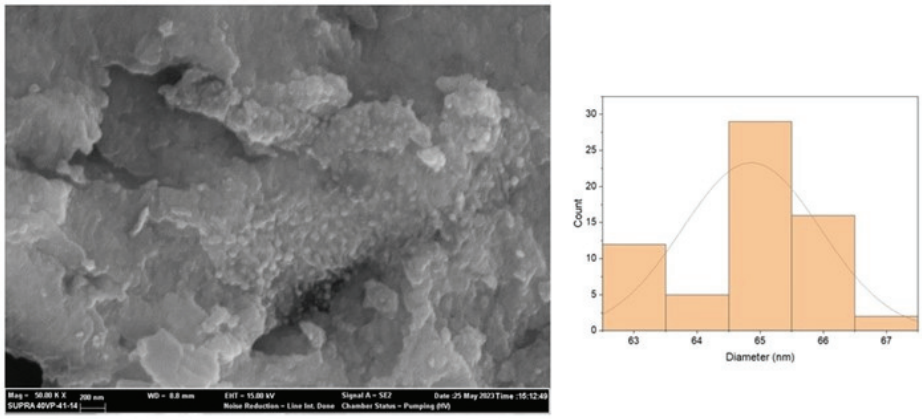

Fig. 7. SEM and histogram of CS–AgNPs.

The synthesized silver nanoparticles had a peak at 2.8 keV in EDX analyses which showed the presence of Ag (Fig. 8). EDX is applied to analyse the principal elemental components of NPs.

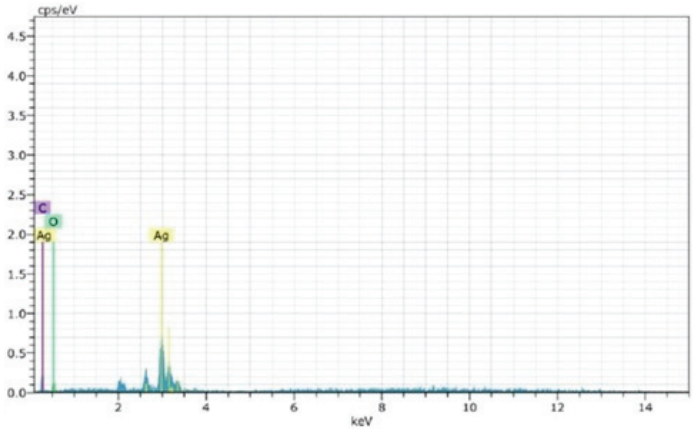

Fig. 8. EDX spectrum of CS–AgNPs.

It was determined that the CS–AgNPs were mainly composed of elemental silver (normalized atomic value 79.13 %), and the C and O contents were relatively lower (Table I).

The antioxidant activity of CS–AgNPs was determined 176.55±1.44 (FRAP) and 82.43±1.22 % μM TE g^{-1} (DPPH). The specific enzymes' inhibitions such as acetylcholinesterase, α-amylase, α-glucosidase urease and xanthine oxidase are

important for the treatment of illness like Alzheimer's disease, *Diabetes mellitus*, stomach infections and gout. The inhibition properties of CS–AgNPs (%) was found to be 52.27±1.09 (*α*-amylase), 43.51±0.98 (*α*-glucosidase), 80.33±1.21 (urease), 66.17±2.08 (acetylcholinesterase) and 73.67±1.70 (xanthine oxidase), respectively (Table II).

TABLE I. EDX results of CS–AgNPs

Element	Series	Unn. C (wt. %)	Norm. C (wt. %)	Atom. C (at. %)	Sigma (wt. %)
Ag	L	23.06	79.13	33.72	0.98
O	K	4.15	14.24	40.91	2.00
C	K	1.93	6.63	25.26	0.85
Total		29.14	100.00	100.00	

TABLE II. Biochemical properties of corn silk extract and CS–AgNPs; different letters represent significant differences at $p < 0.05$ probability level

Parameter	Corn silk extract	CS–AgNPs	Control	Control reagent
Total phenolic content (mg GAE g^{-1} DW sample)	20.16±0.21[a]	24.43±0.19[b]	–	–
FRAP (μM TE g^{-1})	100.18±1.27[a]	176.55±1.44[b]	–	–
DPPH (%)	70.69±1.18[a]	82.43±1.22[b]	–	–
α-Amylase inhibition (%)	48.15±1.11	52.27±1.09	46.84±1.05	Acarbose
α-Glucosidase inhibition (%)	32.21±1.23	43.51±0.98	30.19±1.24	Acarbose
Urease inhibition (%)	50.78±1.15	80.33±1.21	82.66±1.15	Thiourea
Acetylcholinesterase inhibition (%)	47.66±1.98	66.17±2.08	68.41±1.22	Donepezil hydrochloride
Xanthine oxidase inhibition (%)	68.70±1.76	73.67±1.70	76.18±1.18	Allopurinol

The synthesis of metallic nanoparticles using different biological resources has become very popular in recent years.[28,29] By determining the different biological properties of the resulting nanoparticles, their potential for use in areas such as health and environment could be determined. Some biological properties of silver nanoparticles synthesized using different biological sources are presented in Table III.

For example, Amin *et al.*[38] stated that silver nanoparticles based on *Solanum xanthocarpum* L. inhibited the urease enzyme by 64 %. Erenler *et al.*[33] synthesized silver nanoparticles based on *Tagetes erecta* L. in their study. They stated that the antioxidant activities of the nanoparticles they obtained had the IC_{50} values of 23.80 μg mL^{-1} and 2.79 μmol mg^{-1} sample corresponding to the DPPH and FRAP, respectively. Chinnasamy *et al.*[35] stated in their study that the silver nanoparticles they synthesized showed very high antioxidant activity (91±0.5 %, DPPH). Gul *et al.*[37] synthesized silver nanoparticles using different parts of the *Ricinus communis* plant in their study. They stated that the synthesized nanoparticles inhibited xanthine oxidase and urease enzymes by 83.6 and 94.2 %, respectively. Gopal *et al.*[38]

synthesized mushroom-based silver nanoparticles in their study and found that the obtained particles inhibited the α-amylase enzyme by 28 %. Thirumal and Sivakumar[39] synthesized silver nanoparticles based on *Cassia auriculata* and stated that the synthesized nanoparticles inhibited the α-glucosidase enzyme by 80 %. Abdelwahab *et al.*[40] synthesized silver nanoparticles based on *Aspergillus niger* in their study and stated that the nanoparticles they synthesized inhibited the acetylcholine esterase enzyme at a very high rate. The silver nanoparticles could inhibit enzymes by different ways. For example, they could interact with the AChE protein, inhibiting its activity, which demonstrates their affinity for cholinesterase. The lithophilicity of the nanoparticles and the hydrophobic environment of the ChE enzyme molecule facilitate this interaction.[41] As a result of this study, it was determined that the antioxidant properties and the enzyme inhibition properties of the synthesized silver nanoparticles were compatible with the literature.

TABLE III. Synthesis of AgNPs by using different sources

Biological source	UV absorbance, nm	Average size nm	Biomedical application	Reference
Solanum xanthocarpum L.	406	4–18	Antioxidant activity and enzyme inhibition properties	30
Glycosmis mauritiana	435	65.92	Antioxidant activity, antimicrobial activity and enzyme inhibition properties	31
Zea mays L.	461.25	12.63	Antimicrobial activity	32
Tagetes erecta L.	422	46.26	Antioxidant activity	33
Caesalpinia mimosoides	480	20–80	Antibacterial activity	34
Aristolochia bracteolata Lam	430	16.7	Antioxidant and antibacterial activities	35
Mikania cordata	451	26.8–46.0	Antioxidant and antibacterial activities	36
Waste corn silk	470	63–67	Antioxidant activity and enzyme inhibition properties	This study

CONCLUSION

The sustainable use and the protection of natural resources is very important. The natural waste, which increases due to the increasing population, needs to be recycled and used in areas such as technology, health, agriculture and environment. In this study, the environmentally friendly silver nanoparticles were synthesized from the waste corn silk using the green synthesis technique. The potential use of the synthesized nanoparticles in medicine applications was determined and the usability of waste corn silk in the field of health and nanotechnology was determined. As a result of this study, corn silks could be accumulated after the harvest time for recycling and used in the field of nanotechnology for different applications such as drug development, environment, *etc*.

ИЗВОД

ОТПАДНА КУКУРУЗНА СВИЛА ЗА ЕКОЛОШКИ ПРИХВАТЉИВЕ НАНОЧЕСТИЦЕ СРЕБРА: ЗЕЛЕНА СИНТЕЗА, КАРАКТЕРИЗАЦИЈА И ОДРЕЂИВАЊЕ СВОЈСТАВА ИНХИБИЦИЈЕ ЕНЗИМА

MERVE KESKIN

Vocational School of Health Services, Bilecik Şeyh Edebali University, Bilecik, Türkiye

Одрживо коришћење ресурса је веома важно због пораста броја становника и нивоа потрошње. Кукуруз је једна од најпродаванијих житарица на свету. Међутим, многи његови делови, као што су кукурузна свила, корење и кукурузна љуска, одлажу се као пољопривредни отпад. У оквиру одрживости могуће је увести овај отпад у област технологије и развити нове производе зеленом синтезом. У овој студији, отпадна кукурузна свила је сушена, екстрахована и коришћена као прекурсор у синтези сребрних наночестица (CS–AgNPs). CS–AgNPs су окарактерисане коришћењем ултраљубичасте спектрофотометрије, инфрацрвене спектрофотометрије и скенирајућег трансмисионог електронског микроскопа. Утврђени су инхибицијски ефекти CS–AgNPs на ензиме као што су α-амилаза, α-гликозидаза, уреаза, ацетил-холинестераза и ксантин-оксидаза, који су важни за лечење одређених болести. Добијене наночестице су показале максималну апсорбанцију на 470 nm, док је просечна величина наночестица 65 nm. Утврђено је да CS–AgNPs показују веома добру антиоксидативну активност и инхибиторне ефекте на α-амилазу (52,27 %), α-гликозидазу (43,51 %), уреазу (80,33%), ацетил-холинестеразу (66,17 %) и ксантин-оксидазу (73,67 %). Добијени резултати показују да се наночестице синтетизоване техником зелене синтезе могу користити у медицини и фармацији.

(Примљено 22. маја, ревидирано 11. јуна, прихваћено 27. септембра 2024)

REFERENCES

1. J. Nazarko, E. Chodakowska, Ł. Nazarko, *Energies* **15** (2022) 3924 (https://doi.org/10.3390/en15113924)
2. N. T. Abd'Razack. S. O. Medayese, S. I. Shaibu, B. M. Adeleye, *Sust. Cities Soc.* **28** (2017) 297 (https://doi.org/10.1016/j.scs.2016.10.004)
3. T. Daszkiewicz. *Agriculture* **12** (2022) 832 (https://doi.org/10.3390/agriculture12060832)
4. P. C. Nath, A. Ojha, S. Debnath, M. Sharma, P. K. Nayak, K. Sridhar, B. S. Inbaraj, *Animals* **13** (2023) 1366 (https://doi.org/10.3390/ani13081366)
5. C. Chauhan, A. Dhir, M. U. Akram, J. Salo, *J. Clean. Prod.* **295** (2021) 126438 (https://doi.org/10.1016/j.jclepro.2021.126438)
6. S. Bayda, M. Adeel, T. Tuccinardi, M. Cordani, F. Rizzolio, *Molecules* **25** (2019) 112 (https://doi.org/10.3390/molecules25010112)
7. C. Pandit, A. Roy, S. Ghotekar, A. Khusro, M. N. Islam, T. B Emran, S. E. Lam, M. U. Khandaker, D. A. Bradley, *J. King Saud Univer. – Sci.* **34** (2022) 101869 (https://doi.org/10.1016/j.jksus.2022.101869)
8. O. Erenstein, M. Jaleta, K. Sonder, K. Mottaleb, B. M. Prasanna, *Food Sec.* **14** (2022) 1295 (https://doi.org/10.1007/s12571-022-01288-7)
9. S. Ü. Pektaş, M. Keskin, O. C. Bodur, F. Arslan. *J. Food Com. Anal.* **129** (2024) 106133 (https://doi.org/10.1016/j.jfca.2024.106133)
10. N. Biradar, R. A. Shah, M. A. Ahmad, *Recent advances in agricultural sciences and technology*, Ariana Publishers & Distributors, New Delhi, 2023

11. *OECD*, OECD Publishing, Paris, 2010
12. T. M. Tolaymat, A. M. El Badawy, A. Genaidy, K. G. Scheckel, T. P. Luxton, M. Suidan, *Sci. Total Environ.* **408** (2010) 999 (https://doi.org/10.1016/j.scitotenv.2009.11.003)
13. E. Bae, H.-J. Park, J. Lee, Y. Kim, J. Yoon, K. Park, K. Choi, J. Yi, *Environ. Toxicol. Chem.* **29** (2010) 2154 (https://doi.org/10.1002/etc.278)
14. P. Gajjar, B. Pettee, D. Britt, W. Huang, W. Johnson, A. Anderson, *J. Biol. Eng.* **3** (2009) 9 (https://doi.org/10.1186/1754-1611-3-9)
15. M. Keskin, G. Kaya, S. Bayram, A. Kurek-Górecka, P. Olczyk, *Molecules* **28** (2023) 2762 (https://doi.org/10.3390/molecules28062762)
16. A. Tan, *J. Mol. Struct.* **1211** (2020) 128060 (https://doi.org/10.1016/j.molstruc.2020.128060)
17. D. R. Liston, J. A. Nielsen, A. Villalobos, D. Chapin, S. B. Jones, S. T. Hubbard, I.A. Shalaby, A. Ramirez, D. Nason,W. White, *Eur. J. Pharm.* **486** (2004) 9 (https://doi.org/10.1016/j.ejphar.2003.11.080)
18. A. Zia, A. Shahzad, N. Riaz, S. Khan, U. Farooq, S. M. Bukhari, A. Al-Harrasi, *Green Proc. Synt.* **13** (2024) 20230229 (https://doi.org/10.1515/gps-2023-0229)
19. M. Keskin, *El-Cezeri J. Sci. Eng.* **9** (2022) 266 (https://doi.org/10.31202/ecjse.963670)
20. V. L. Singleton, R. Orthofer, R. M. Lamuela-Raventós, *Meth. Enzymol*. **299** (1999) 152 (https://doi.org/10.1016/S0076-6879(99)99017-1)
21. V. L. Singleton, J. A. Rossi, *Am. J. Enol. Viticult.* **16** (1965) 144 (https://doi.org/10.5344/ajev.1965.16.3.144)
22. M. Cuendet, K. Hostettmann, O. Potterat, W. Dyatmiko, *Helv. Chim. Acta* **80** (1997) 1144 (https://doi.org/10.1002/hlca.19970800411)
23. I. F. Benzie, J. J. Strain, *Meth. Enzym*. **299** (1999) 15 (https://doi.org/10.1016/s0076-6879(99)99005-5)
24. Ş. Keskin, N. S. Ertunga, *Turkish J. Biochem.* **42** (2017) 633 (https://doi.org/10.1515/tjb-2016-0123)
25. A. Gholamhoseinian, H. Fallah, F. Sharifi-Far, M. Mirtajaddini, *Int. J. Pharmacol.* **4** (2008) 460 (https://doi.org/10.3923/ijp.2008.460.465)
26. Ş. Keskin, Y. Şirin, H. E. Çakir, M. Keskin, *S. Afr. J. Bot.* **120** (2019) 170 (https://doi.org/10.1016/j.sajb.2018.04.017)
27. N. Baltas, O. Yildiz, S. Kolayli, *J. Enzyme Inhib. Med. Chem*. **31** (2016) 52 (https://doi.org/10.3109/14756366.2016.1167049)
28. R. K. Das, V.L. Pachapur, L. Lonappan, M. Naghdi, R. Pulicharla, S. Maiti, M. Cledon, L. M. A. Dalila, S. J Sarma, S. K. Brar, *Nanotech. Environ. Eng.* **2** (2017) 18 (https://doi.org/10.1007/s41204-017-0029-4)
29. P. K. Dikshit, J. Kumar, A. K. Das, S. Sadhu, S. Sharma, S. Singh, P. K. Gupta, B. S. Kim, *Catalysts* **11** (2021) 902 (https://doi.org/10.3390/catal11080902)
30. M. Amin, F. Anwar, M. R. S. A. Janjua, M. A. Iqbal, U. Rashid. *Int. J. Mol. Sci.* **13** (2012) 9923 (https://doi.org/10.3390/ijms13089923)
31. M. Govindappa, H. Farheen, C. P. Chandrappa, R. V. Rai, V. B. Raghavendra, *Adv. Nat. Sci: Nanosci. Nanotech*. **7** (2016) 035014 (https://doi.org/10.1088/2043-6262/7/3/035014)
32. A. Eren, M. F. Baran, *App. Ecol. Env. Res.* **17** (2019) 4097 (https://doi.org/10.15666/aeer/1702_40974105)

33. R. Erenler, C. Temiz, I. Yildiz, Y. Yanar, C. Ozyigit, *J. Optoel. Adv. Mat.* **23** (2021) 503 (https://joam.inoe.ro/articles/green-synthesis-and-characterization-of-silver-nanoparticles-from-tagetes-erecta-flowers/)
34. S. Shankar, N. Tanomrod, S. Rawdkuen, J.W. Rhim, *In. J. Biol. Macromol.* **92** (2016) 842 (https://doi.org/10.1016/j.ijbiomac.2016.07.107)
35. R. Chinnasamy, K. Chinnaperumal, T. Cherian, K. Thamilchelvan, B. Govindasamy, C. Vetrivel, V. Perumal, P. Willie, P. Krutmuang, *Biomass Conv. Bioref.* (2023) 1 (https://doi.org/10.1007/s13399-023-03750-8)
36. M. Khatun, Z. Khatun, M. R. Karim, M. R. Habib, M. H. Rahman, M. A. Aziz, *Food Chem. Adv.* **3** (2023) 100386 (https://doi.org/10.1016/j.focha.2023.100386)
37. A. Gul, F.A. Shaheen, I. Ahmad, B. Khattak,M. Ahmad, R. Ullah, A. Bari, S. S. Ali, A. Alobaid, M. M. Asmari, H. M. Mahmood, *Biomolecules* **11** (2021) 206 (https://doi.org/10.3390/biom11020206)
38. G. Debnath, P. Das, A. K. Saha, *Proc. Natl. Acad. Sci. India, B* **90** (2019) 37 (https://doi.org/10.1007/s40011-019-01076-y)
39. S. Thirumal, T. Sivakumar, *Int. J. Botany Stud.* **6** (2021) 35 (https://www.botanyjournals.com/assets/archives/2021/vol6issue3/6-2-132-783.pdf)
40. G. M. Abdelwahab, A. Mira, Y. B. Cheng, T. A. Abdelaziz, M. F. I. Lahloub, A. T. Khalil, *Plos ONE* **16** (2021) e0257071. (https://doi.org/10.1371/journal.pone.0257071)
41. E. O. Mikhailova. *J. Funct. Biomater.* **11** (2020) 84 (https://doi.org/10.3390/jfb11040084).

Journal of the Serbian Chemical Society
JSCS@tmf.bg.ac.rs • www.shd.org.rs/JSCS
J. Serb. Chem. Soc. 90 (3) 383–392 (2025)
JSCS–5394
Original scientific paper
Published 24 March, 2025

A comparative study on ecological risk assessment of some potentially toxic elements accumulation in surface sediment of stagnant and running water ecosystems in Meriç delta wetland, Turkish Thrace

GAZEL BURCU AYDIN*

Trakya University, Faculty of Science, Department of Biology, 22100, Edirne, Turkey

(Received 16 January, revised 12 July, accepted 21 November 2024)

Abstract: This study determined arsenic, chromium, cadmium, copper, zinc, nickel and lead concentrations in the sediment of the lake and river and evaluated their ecological risk profile and compared the ecological risk profile of some potentially toxic elements accumulated in surface sediment of stagnant and running water ecosystems in the Meriç Delta Wetland, Turkish Thrace which is located in the European part of Turkey and have two important river systems, Meriç and Ergene, which provide freshwater resources for the region. Sediment samples were taken seasonally from three stations (one station from the river and two stations from the lake) in 2020. Ecological and biological risk analyses were calculated using the potential ecological risk index (*RI*), biological risk index ($mERM\text{-}Q_i$), contamination factor (*CF*), contamination degree (*CD*) and pollution load index (*PLI*). As a result, although *RI* stated that Cd was determined as the riskiest element and $mERM\text{-}Q_i$ stated that Zn was determined as the riskiest element, indicated that there were no high ecological risks besides the investigated elements in the area. Although it is expected that the sediment quality of running water systems is better than that of stagnant water systems, the results of risk indices in the present study showed that the station selected for running water was the riskiest station in terms of potentially toxic elements.

Keywords: ecological risk indices; toxic elements assessment; lagoon lake; Meriç River Delta.

INTRODUCTION

Increasing toxic element (TEs) pollution has become a global ecological concern for water, air, and soil ecosystems.[1] Supply to industry and agriculture due to the growth of the population increases the accumulation of TEs, especially

* Corresponding author. E-mail: gburcuaydin@trakya.edu.tr
https://doi.org/10.2298/JSC240116107A

in aquatic ecosystems.[2] Toxic pollution, which is discharged into aquatic ecosystems by precipitation and waste channels, accumulates in the sediment. The sediment plays a significant role in water quality and the health of aquatic organisms and the intense accumulation in the sediment causes the complicated biogeochemical exchanges.[3,4] Therefore, periodic investigation and monitoring of the sediment quality are essential for sustainability of the aquatic ecosystem.[3,5] Some indices that were developed for determining the ecological risk profile of potentially TEs in sediments are used and recommended for this purpose.[1,4,6–12] In the present study, the indices; potential ecological risk index (*PERI*), biological risk index (*BRI*), contamination factor (*CF*), contamination degree (*CD*) and pollution load index (*PLI*) were used because of their widely intended application. However, they also have some disadvantages and in despite of their disadvantages, they are very useful for saving and protecting a wetland.[11]

The Turkish Thrace Region is located in the European part of Turkey and have two important river systems, Meriç and Ergene. The rivers and their tributeaaries provide freshwater resources for the region. Due to the availability of arable lands and freshwater resources, the region is under intensive agricultural applications and pollution load.[2] The Meriç Delta located in Turkish Thrace Region lies in Turkey lands on about 35,000 ha area (about 10,000 ha part of the delta lies in Greece lands) and it is in A Class Wetland category.[13] The delta have different water bodies and the Dalyan Lagoon Lake is one of them. The Dalyan Lagoon Lake is located in the area where the Meriç River empties into the Aegean Sea, in Edirne province. The lagoon lake is formed by alluvial flows from the Meriç River. Due to its rich aquatic biodiversity, the lagoon lake is an important wetland for fish and especially for waterfowl.[14] The Enez District centre is located just north-east of the Dalyan Lagoon Lake and the lake is surrounded by agricultural lands. This situation causes significant urban and agricultural pressures on the lagoon lake.[14] There are many studies showing that wetlands in the Meriç Delta is exposed to pollution (Gala Lake, Sığırcı Lake, Ergene River, Meriç River and dam lakes).[2,4,13,15–17] In the present study, As, Cr, Cd, Cu, Zn, Ni, and Pb concentrations in the sediment of the Dalyan Lagoon Lake and the Meriç River connected with the Dalyan Lagoon Lake were determined seasonally and were detected by spectrometric method. According to the element concentration results, the ecological risk profile was evaluated and compared by using the indices; *PERI*, *BRI*, *CF*, *CD* and *PLI*. Although, there are many studies about sediment quality of the wetlands in the Meriç Delta,[2,3,13,15,16] the Dalyan Lagoon Lake and the Meriç River segment connected with the Dalyan Lagoon Lake were investigated for the first time in the present study. Thus, data about the sediment quality and ecological risk profile of the area were obtained. In additional, with this study, sediment structures and deposition of stagnant and running water ecosystems were compared in terms of flow dynamics.

EXPERIMENTAL

Study area and sediment sampling

Details about the study area are given in the Supplementary material to this paper

Sediment sampling was conducted seasonally (spring, summer, autumn and winter) between May 2020 and December 2020 from 3 stations. Two stations (St.1 and St. 2) were selected from the Dalyan Lagoon Lake and one station (St. 3) were selected from the Meriç River (Fig. S-1 of the Supplementary material). Sediment samples were taken using Ekman Grab (sampling 15×15 cm^2 area) from the lake and the river. The upper to 5 cm sediment portion was collected with sampler in sterile glass bottles. Sediment sample belonging to each station was obtained by mixing sediments randomly collected three times.

Chemical analysis

To determinate the elements (As, Cr, Cu, Cd, Zn, Ni, Pb) in sediment samples, obtained material was dried for 3 h at 105 °C. One gram each of dry samples were dissolved in 3 mL of distilled water. The solution obtained by adding an acid mixture HNO_3, HCl, $HClO_4$, at the volume ratio of 5:2:1, was passed through filter paper and taken into polyethylene bottles.[18] The element concentrations in the sediment samples were detected using the "Agilent 7700 xx" branded inductively coupled plasma-mass spectrometer (ICP-MS) device at the Trakya University Technology Research and Development Application and Research Center (TÜTAGEM).[19] Concentration values (given in mg/L) of all examined elements (As, Cr, Cu, Pb, Zn, Cd, Ni) are presented in Fig. S-1.

Risk indices

*Potential ecological risk index (*RI*)*. *RI* is used to evaluate the ecological contamination risk and based on the sensitivity of the aquatic ecosystems productivity. The index is calculated by the following formula:[6]

$$RI = \sum E^i_r \quad (1)$$

$$E^i_r = T^i_r C^i_f \quad (2)$$

$$C^i_f = C^i_0 / C^i_n \quad (3)$$

where E^i_r = potential ecological risk index of an each element. The scale of E^i_r is given in Table I; T^i_r = toxic response factor;[6] C^i_f = The contamination factor; C^i_0 = The concentration of elements in the sediment; C^i_n = The preindustrial reference value for elements.[6]

*Biological risk index (*mERM-Q*)*. Biological risk index is used to evaluate the assessing the potential effects of multiple element contamination in sediment. The index is calculated by the following formula:[20]

$$mERM\text{-}Q = (\sum n_i = ERM\text{-}Q_i)/n \quad (4)$$

$$ERM\text{-}Q_i = C_i/ERM_i \quad (5)$$

where *mERM-Q* = the effect range median quotient of multiple element contaminations. The scale of *mERM-Q* is given in Table I; C_i = the concentration of an element in the sediment from the sampling stations; *ERMi* = the *ERM* value of a determined element;[6] n = the number of selected elements.

*Contamination factor (*CF*)*. This method is used to account for the contamination of single elements and is calculated by the following formula.[6] The scale of *CF* is given in Table II:

$$CF = C_{sample}/C_{background} \quad (6)$$

where C_{sample} = the concentration of an element in the sediment from the sampling stations; $C_{background}$ = the reference value for elements.[6,7]

*Contamination degree (*CD*)*. This method is defined sum of all *CF*s for given lake.[6] The scale of *CD* is given in Table II:

$$CD = \sum CF \quad (7)$$

*Pollution load index (*PLI*)*. This index is used to evaluate sediment contamination and is defined as the n^{th} root of the product of the *nCF*. The following formula is used to calculate the index.[21] The scale of *PLI* is given in Table II:

$$PLI = (CF1 \times CF2 \times CF3 \times \cdots \times CFn)/n \quad (8)$$

TABLE I. The scale for E^i_r, *RI*, *ERM-*Q_i and *mERM-*Q[20]

Potential ecological risk assessment				Biological risk assessment	
E^i_r	Monomial factor	*RI*	Multinomial factors	*ERM-*Q_i and *mERM-Q*	Monomial and multinomial factors
<40	Low ecological risk	<95	Low ecological risk	<0.1	Low priority side
40–80	Moderate ecological risk	95–190	Moderate ecological risk	0.1–0.5	Medium-low priority side
80–160	Considerable ecological risk	190–380	Considerable ecological risk	0.5–1.5	High-medium priority side
160–320	High ecological risk	>380	Very high ecological risk	>1.5	High priority side
>320	Very high ecological risk				

TABLE II. The scale for *CF*, CD and *PLI*;[6,21] *CF* – contamination factor; *CD* – contamination degree; *PLI* – pollution load index

CF	Contamination	*CD*	Contamination	*PLI*	Pollution state
< 1	Low	< 8	Low	< 1	Unpolluted
$1 \leq CF \leq 3$	Moderate	$8 \leq CD < 16$	Moderate	> 1	Polluted
$3 \leq CF \leq 6$	Considerable	$16 \leq CD < 32$	Considerable		
≥ 6	Very high	≥ 32	Very high		

RESULTS AND DISCUSSION

The results of measured element levels in the sediment are presented in Fig. S-1. According to this, for As concentration values vary between 0.11 and 1.56 mg/L; for Cr between 0.06 and 0.52 mg/L; for Cu between 0.23 and 3.57 mg/L; for Pb between 0.3 and 5.02 mg/L; for between Zn 0.33 and 39.9 mg/L; for Cd between 0.001 and 0.043 mg/L; for Ni between 0.001 and 6.3 mg/L. The results of E^i_r, multinomial *RI*, monomial *ERM-*Q_i and multinomial *mERM–Q* for each station and season were identified and given in Table S-I of the Supplementary material. In addition, the results belonging to the *CF*, *CD* and *PLI* were identified and given in Table III.

TABLE III. The toxic element risk index values (*CF*, *CD* and *PLI*) in sediments of the Dalyan Lagoon Lake (Ave: Average; St: Station)

St	*CF*							*CD*	*PLI*
	As	Cr	Cu	Pb	Zn	Cd	Ni		
Spring									
1	0.008	0.002	0.012	0.006	0.005	0.025	0.005	0.063	0
2	0.01	0.001	0.006	0.004	0.007	0.003	0.005	0.037	0
3	0.104	0.004	0.071	0.03	0.038	0.01	0.084	0.342	0
Ave	0.041	0.002	0.03	0.013	0.017	0.013	0.032		
Summer									
1	0.009	0.001	0.005	0.006	0.002	0.001	0.002	0.025	0
2	0.011	0.001	0.006	0.005	0.002	0.002	0.002	0.028	0
3	0.069	0.001	0.016	0.007	0.005	0.004	0.005	0.107	0
Ave	0.03	0.001	0.009	0.006	0.003	0.002	0.003		
Autumn									
1	0.017	0.003	0.022	0.028	0.228	0.01	0.011	0.319	0
2	0.046	0.004	0.028	0.048	0.032	0.02	0.008	0.186	0
3	0.03	0.004	0.028	0.072	0.119	0.01	0.012	0.275	0
Ave	0.031	0.003	0.026	0.049	0.127	0.013	0.01		
Winter									
1	0.007	0.002	0.008	0.007	0.008	0.014	0.00001	0.046	0
2	0.021	0.002	0.012	0.005	0.009	0.012	0.00001	0.061	0
3	0.033	0.006	0.019	0.025	0.012	0.043	0.00004	0.138	0
Ave	0.021	0.003	0.013	0.012	0.01	0.023	0.00003		
Average	0.03	0.002	0.02	0.05	0.04	0.01	0.01		

According to *PERI*, the results of monomial factor E^i_r and multinomial factor *RI* all the investigated stations and seasons exhibited “low ecological risk”. The monomial factor E^i_r belonging to *PERI*s indicated that the density of the investigated TEs can be followed as Cd > Pb > As > Cu > Zn > Ni > Cr (Fig. 2). The multinomial factor *RI* belonging to *PERI*s showed that the ecological risks of the investigated stations can be sorted as St. 3 (2.597) > St.1 (1.287) > St. 2 (1.165), Table S-I.

According to *BRI*, although the results of monomial factor *ERxM-*Q_i posed “low priority side” at all the investigated stations and seasons, nickel at St. 3 in spring season and zinc at St. 1 in autumn season posed “medium-low priority side”. The results of multinomial factors (*mERM–Q*) posed “low priority side” at all the investigated stations and seasons and the toxicity of the investigated elements can be sorted as Zn > Ni > Pb > As > Cu > Cr > Cd (Fig. 3). The multinomial factor *mERM-Q* of *BRI*s indicated that the biologically risk of contamination to sediments of the investigated stations can be sorted as St. 3 (0.015) > St. 1 (0.008) > St. 2 (0.004), Table S-I.

As a results of C*F* values for all the investigated elements showed “low contamination” and the risks of the investigated TEs in terms of *CF* can be sorted

as Pb > Zn > As > Cu > Cd = Ni > Cr (Table IV). As a results of *CD* values for all the investigated elements showed "low degree of contamination" and total contamination degree followed the order of stations St. 3 (0.21) > St. 1 (0.11) > St. 2 (0.08). Also, The *PLI*s indicated that all stations were unpolluted (Table III).

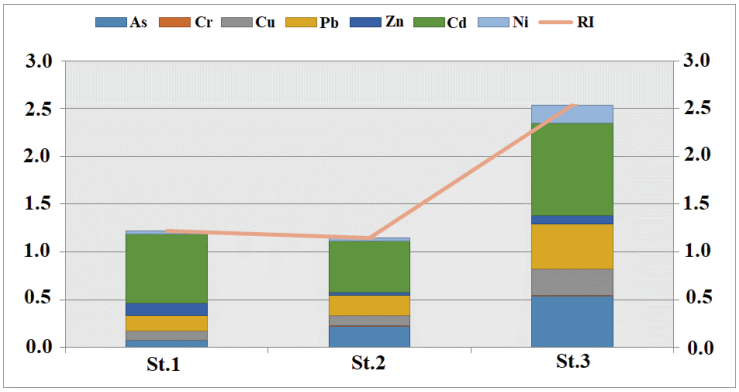

Fig. 2. Values of potential ecological risk index (*PERI*).

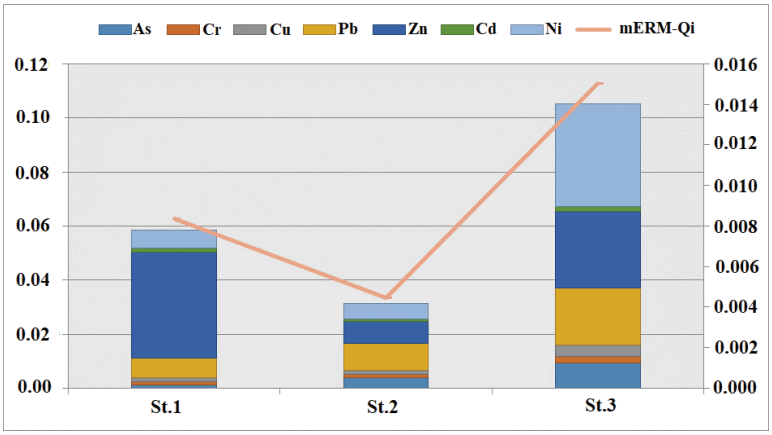

Fig. 3. Values of Biological Risk Index (*BRI*).

The present study was carried out to determine and compare the existence and risk profile of some potentially TEs in stagnant and running water ecosystems at Meriç Delta Wetland. According to result of *mERM-Q_i*, Zn was determined as the riskiest element, and as a result of *RI*, Cd was determined as the riskiest element for the sediments of the Dalyan Lagoon Lake. In previous studies performed in Meriç Delta, Cd was reported as the riskiest toxic element.[4,15] In the studies carried out in dam lakes in the Meriç Delta[4] and Gala Lake,[15] it was reported that cadmium was found to be the highest risk factor in terms of potential *RI*.[4,15] Cadmium is a toxic element in agriculture and it can be easily

spread to water by using phosphate fertilizers.[4,15] According to the study,[22] cadmium residues in fertilizers taken from different fertilizer factories were investigated and the results showed that the vales were over the limit values notified for fertilizers.[22] Because of intensive agricultural applications in Meriç--Ergene River Basin (especially rice production), excessive use of fertilizer can cause Cd accumulation.

Zinc is exceedingly related to organic matter.[23] Aquatic systems are inclined to have a higher deposition rate of organic matter.[24] So, the accumulation of Zn is widespread in sediment. In the present study, Zn was determined as the riskiest element and the monomial factor ($ERM\text{-}Q_i$) for Zn posed a "medium-low priority side" at St. 1 in the autumn season.

Nickel occurs naturally in the Earth's crust and enters natural resources, usually through anthropogenic activities.[9] In the study carried out in Gala Lake;[15] Ni was the riskiest element according to *BRI*.[15] In the present study, the results of the monomial factor ($ERM\text{-}Q_i$) for Ni posed a "medium-low priority side" at St. 3 in the spring season.

Since the water of the lake is connected with the water of the Meriç river, two stations were selected from the lake (St. 1 and 2) and one from the Meriç river (St. 3). The results of used risk indices in the present study indicated that St. 3 (selected from Meriç River) was the riskiest station in terms of investigated TEs. In the studies conducted on other water bodies in the Meriç Delta, there is a significant accumulation of TEs due to intensive agricultural and industrial applications.[2,4,15] For this reason, it is an expected result that the station (St. 3) selected from the Meriç River in this study is the riskiest. In addition, there are many studies investigating ecological risk analyzes in sediment in lagoon lakes in Turkey.[25–27] According to studies,[25,27] there were no pollution and no moderate or high ecological risk for Köyceğiz (Muğla) Lagoon System. According to the results of ecological risk assessment study of Çardak Lagoon Lake (Çanakkale), the toxic risk index ranged from 5.21 to 11.00, with a low mean value of 7.98.[26]

CONCLUSION

As a result of the study, it was concluded that toxic element pollution in the sediments of selected stations at the present study (Dalyan Lagoon Lake and Meriç River) is less than in other water bodies in the Meriç River Delta (Gala Lake, Sığırcı Lake, Ergene River, Meriç River and dam lakes in the Meriç River Delta). The presence of sea currents and channels in lagoon lakes is important in maintaining water quality and thus sediment quality. Although there is agricultural and industrial pollution in other water bodies in the delta, it can be said that Dalyan Lagoon Lake has improved the water and sediment quality by the sea connections. However, other biological and physicochemical studies that support these results are needed in the region. Water and sediment quality of stagnant and

running water ecosystems are different from each other due to their flow dynamics. It is expected that the sediment quality of running water systems is better than that of stagnant water systems. In this study, despite the flow dynamics of the Meriç River, there is a higher risk of TEs compared to the Dalyan Lagoon Lake due to intensive agricultural applications and the industrial pollution load of the Ergene River. Because, the Meriç River arises in Bulgaria and unites with the Arda River in Edirne. Then merging the Tunca River south of Edirne, it joins the Ergene River and flows into the Aegean Sea (Saros Gulf). So, the Ergene River increases the pollution load of the Meric River. The studies performed in the Ergene and Meriç rivers showed that agricultural and industrial pollution load were intensive. It is recommended that such studies must be carried out periodically and kept under control for the sustainability of the lagoon lake where fishing is carried out intensively.

SUPPLEMENTARY MATERIAL

Additional data and information are available electronically at the pages of journal website: https://www.shd-pub.org.rs/index.php/JSCS/article/view/12778, or from the corresponding author on request.

ИЗВОД

КОМПАРАТИВНА СТУДИЈА О ПРОЦЕНИ ЕКОЛОШКОГ РИЗИКА ОД АКУМУЛАЦИЈЕ НЕКИХ ПОТЕНЦИЈАЛНО ТОКСИЧНИХ ЕЛЕМЕНАТА У ПОВРШИНСКОМ СЕДИМЕНТУ ЕКОСИСТЕМА СТАЈАЋИХ И ТЕКУЋИХ ВОДА У МОЧВАРНОМ ПОДРУЧЈУ ДЕЛТЕ РЕКЕ МЕРИЧ, ТУРСКА ТРАКИЈА

GAZEL BURCU AYDIN

Trakya University, Faculty of Science, Department of Biology, 22100, Edirne, Turkey

Овом студијом утврђене су концентрације арсена, хрома, кадмијума, бакра, цинка, никла и олова у седименту језера и реке, процењен је профил њиховог еколошког ризика и упоређен профил ризика неких потенцијално токсичних елемената акумулираних у површинском седименту екосистема стајаћих и текућих вода у Мочварном подручју делте Мерича, Турска Тракија. Ова делта налази се у европском делу Турске и има два важна речна система, Мерич и Ергене, који обезбеђују слатководне ресурсе за регион. Узорци седимента су узимани сезонски са три станице (једна станица са реке и две станице са језера) у 2020. години. Анализа еколошког и биолошког ризика израчуната је коришћењем индекса потенцијалног еколошког ризика (*RI*), индекса биолошког ризика ($mERM\text{-}Q_i$), фактора контаминације (*CF*), степена контаминације (*CD*) и индекса оптерећења загађењем (*PLI*). Као резултат тога, иако је *RI* показао да је Cd најризичнији елемент, а $mERM\text{-}Q_i$ је указао на Zn као најризичнији елемент, ова студија показује да нема високих еколошких ризика у овој области. Иако се очекује да је квалитет седимента у системима за текућу воду бољи него у системима са стајаћим водама, резултати индекса ризика у овој студији су показали да је станица одабрана за текућу воду била најризичнија станица у погледу истраживања потенцијално токсичних елемената.

(Примљено 16. јануара, ревидирано 12. јула, прихваћено 21. новембра 2024)

REFERENCES

1. M. S. Islam, R. Proshad, S. Ahmed, *Hum. Ecol. Risk Assess.* **24** (2018) 699 (https://doi.org/10.1080/10807039.2017.1397499)
2. C. Tokatlı, *Environ. Monit. Assess.* **191** (2019) 706 (https://doi.org/10.1007/s10661-019-7885-2)
3. G. B. Yu, Y. Liu, S. Yua, S. C. Wuc, A. O. W. Leung, X. S. Luo, B. Xua, H. B. Li, M. H. Wong, *Chemosphere* **85** (2011) 1080 (https://doi.org/10.1016/j.chemosphere.2011.07.039)
4. C. Tokatlı, *Aquat. Sci. Eng.* **34** (2019) 90 (https://doi.org/10.26650/ASE2019545919)
5. F. Ustaoğlu, Md S. Islam, *Aqua. Ecol. Indic.* **113** (2020) 106237 (https://doi.org/10.1016/j.ecolind.2020.106237)
6. L. Håkanson, *Water Res.* **14** (1980) 975 (https://doi.org/10.1016/0043-1354(80)90143-8)
7. M. Varol, *J. Hazard. Mater.* **195** (2011) 355 (https://doi.org/10.1016/j.jhazmat.2011.08.051)
8. A. Çiçek, C. Tokatlı, E. Köse, *Pak. J. Zool.* **45** (2013) 1335 (https://www.zsp.com.pk/pdf45/1335-1341%20_21_%20PJZ-1403-13%2029-8-13%20CHECKED%20manuscript.pdf)
9. C. Tokatlı, A. Çiçek, E. Köse, *Iğdır Univ. J. Inst. Sci. Tech.* **7** (2017) 267 (https://www.igdir.edu.tr/Addons/Resmi/announc/5053/5053-article-file14.pdf-abstract-file.pdf)
10. M. Maanan, M. E. Barjy, N. Hassou, H. Zidane, B. Zourarah, M. Maanan, *Hum. Ecol. Risk Assess.* **24** (2018) 602 (https://doi.org/10.1080/10807039.2017.1394176)
11. Ş. Fikirdeşici-Ergen, *Commun. Fac. Sci. Univ. Ank., C* **29** (2020) 202 (https://dergipark.org.tr/en/download/article-file/1148564)
12. C. Tokatlı, A. Uğurlu, E. Köse, A. Çiçek, N. Arslan, H. Dayıoğlu, Ö. Emiroğlu, *Environ. Earth Sci.* **80** (2021) 17 (https://doi.org/10.1007/s12665-020-09333-4)
13. C. Tokatli, F. Ustaoğlu, *Environ. Earth Sci.* **79** (2020) 426 (https://doi.org/10.1007/s12665-020-09171-4)
14. O. Akyol, T. Ceyhan, *EgeJFAS* **27** (2010) 31 (http://www.egejfas.org/tr/download/article-file/57391)
15. C. Tokatlı, *Arch. Environ. Prot.* **43** (2017) 34 (https://doi.org/10.1515/aep-2017-0007)
16. C. Tokatlı, *Acta Aliment.* **47** (2018) 470 (https://doi.org/10.1556/066.2018.47.4.10)
17. G. B. Aydın, B. Çamur-Elipek, *Oceanol Hydrobiol Stud.* **51** (2022) 212 (https://doi.org/10.26881/oandhs-2022.2.09)
18. USEPA, *Method 3051a: Microwave Assisted Acid Dissolution of Sediments, Sludges, Soils, and Oils*, Revision 1, United States Environmental Protection Agency, Washington, DC, 2007 (https://www.epa.gov/sites/default/files/2015-12/documents/3051a.pdf)
19. J. T. Creed, C. A. Brockhoff, T. D. Martin, *Method 200.8, Determination of Trace Elements in Waters and Wastes by Inductively Coupled Plasma – Mass Spectrometry,* 1994 (https://www.epa.gov/sites/default/files/2015-06/documents/epa-200.8.pdf)
20. E. R. Long, C. G. Ingersoll, D. D. MacDonald, *Environ. Sci. Technol.* **40** (2005) 1726 (https://doi.org/10.1021/es058012d)
21. D. C. Tomlinson, J. G. Wilson, C. R. Harris, D. W. Jeffery, *Helgolander Meeresunters* **33** (1980) 566 (https://doi.org/10.1007/BF02414780)
22. N. Köleli, Ç. Kantar, *Ekoloji* **14** (2005) 55 (https://silo.tips/download/fosfat-kayasy-fosforik-asit-ve-fosforlu-gbrelerdeki-toksik-ayr-metal-cd-pb-ni-as)
23. Z. Elhaj Baddar, E. Peck, X. Xu, *PLOS One* **16** (2021) e0255527 (https://doi.org/10.1371/journal.pone.0255527)

24. K. R. Reddy, R. D. Delaune, *Biogeochemistry of Wetlands: Science and Applications,* CRC Press, Boca Raton, FL, 2008 (https://doi.org/10.1201/9780203491454)
25. T. O. Genç, F. Yılmaz, *J. Adv. Agric.* **6** (2016) 804 (https://doi.org/10.24297/jaa.v6i1.5386)
26. S. Kükrer, A. E. Erginal, Ş. Kılıç, Ö. Bay, T. Akarsu, E. Öztura, *Environ. Monit. Assess.* **192** (2020) 359 (https://doi.org/10.1007/s10661-020-08336-9)
27. M. Yabanlı, A. Yozukmaz, İ. Şener, H. Hasanhocaoğlu Yapıcı, E. Çetin Kasa, *Acta Aquat. Turc.* **18** (2022) 109 (https://doi.org/10.22392/actaquatr.993135).

Journal of the Serbian Chemical Society
JSCS@tmf.bg.ac.rs • www.shd.org.rs/JSCS
J. Serb. Chem. Soc. 90 (3) S95–S96 (2025) *Supplementary material*

SUPPLEMENTARY MATERIAL TO

A comparative study on ecological risk assessment of some potentially toxic elements accumulation in surface sediment of stagnant and running water ecosystems in Meriç delta wetland, Turkish Thrace

GAZEL BURCU AYDIN*

Trakya University, Faculty of Science, Department of Biology, 22100, Edirne, Turkey

J. Serb. Chem. Soc. 90 (3) (2025) 383–392

STUDY AREA

The study area is located between latitude 40° 42’ N and longitude 26° 04’ E (Fig. S-1). The Dalyan Lagoon Lake is formed by alluvial flows from Meriç River and is fed by water flows from Meriç River and Aegean Sea. It has an area of 3.7 km^2 and its length is 5 km. The Meriç River originates in Bulgaria and forms part of the Greece-Turkey border. The Meriç River with a catchment area of more than 56.000 km^2 (covers 14.600 km^2 in Turkey) is 480 km long. It merges with the Ergene River in the İpsala district and flows into the Aegean Sea near Enez.

* Corresponding author. E-mail: gburcuaydin@trakya.edu.tr

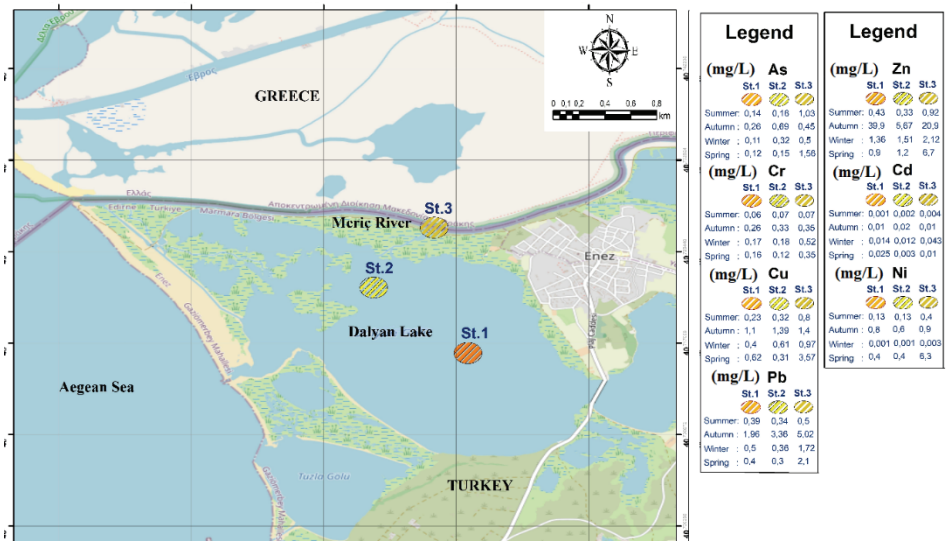

Fig. S-1. The study area, sampling stations, and concentration of the investigated elements (As, Cr, Cu, Pb, Zn, Cd, Ni).

TABLE S-I. The toxic element risk index values (PERI and BRI) in sediments of the Dalyan Lagoon Lake (St: Station)

Seasons	St	E^i_r							RI	ERM-Q_i							mERM-Q_i
Spring		As	Cr	Cu	Pb	Zn	Cd	Ni		As	Cr	Cu	Pb	Zn	Cd	Ni	
	1	0.08	0.005	0.103	0.08	0.011	1.5	0.04	1.82	0.001	0.001	0.002	0.004	0.003	0.0028	0.008	0.003
	2	0.1	0.004	0.052	0.06	0.015	0.2	0.04	0.45	0.002	0.001	0.001	0.003	0.004	0.0003	0.008	0.003
	3	1.04	0.012	0.595	0.42	0.084	0.6	0.63	3.38	0.018	0.002	0.009	0.019	0.025	0.0011	0.126	0.029
Summer																	
	1	0.093	0.002	0.038	0.078	0.005	0.06	0.01	0.29	0.002	0.0004	0.001	0.004	0.002	0.0001	0.003	0.001
	2	0.107	0.002	0.053	0.068	0.004	0.12	0.01	0.37	0.002	0.0005	0.001	0.003	0.001	0.0002	0.003	0.001
	3	0.587	0.002	0.133	0.1	0.012	0.24	0.04	1.11	0.012	0.0005	0.002	0.005	0.003	0.0004	0.008	0.004
Autumn																	
	1	0.17	0.008	0.183	0.392	0.499	0.6	0.08	1.94	0.003	0.002	0.003	0.018	0.148	0.001	0.016	0.027
	2	0.36	0.011	0.232	0.672	0.071	1.2	0.06	2.71	0.008	0.002	0.004	0.031	0.021	0.002	0.012	0.011
	3	0.241	0.011	0.233	1.004	0.261	0.6	0.09	2.44	0.005	0.002	0.004	0.046	0.077	0.001	0.018	0.022
Winter																	
	1	0.073	0.006	0.067	0.1	0.017	0.84	0.0001	1.1	0.001	0.001	0.001	0.005	0.005	0.002	0.00002	0.002
	2	0.213	0.006	0.102	0.072	0.019	0.72	0.0001	1.13	0.004	0.001	0.002	0.003	0.006	0.001	0.00001	0.002
	3	0.333	0.017	0.162	0.34	0.027	2.58	0.0003	3.46	0.006	0.004	0.002	0.016	0.008	0.005	0.00006	0.006